Applications of Telecommunication Transceiver Architectures in All-Fiber Coherent Detection Lidars

Abari, Cyrus F.; Mann, Jakob

Publication date:
2015

Document Version
Publisher's PDF, also known as Version of record

Applications of Telecommunication Transceiver Architectures in All-Fiber Coherent Detection Lidars

Cyrus F. Abari

Thesis for
PhD in Engineering

Technical University of Denmark
Lyngby, Denmark
2015

Department of Wind Energy
Technical University of Denmark
DTU Risø Campus, Frederiksborgvej 399
DK-4000 Roskilde, Denmark

Abstract

Coherent detection lidars have evolved over time and gradually become the de facto instruments for high resolution measurement of atmospheric boundary layer winds. The earlier versions of these lidars were bulky, expensive, and suffered from vulnerability to environmental effects such as temperature and vibrations. However, with the advent of fiber-optic communications a new class of stable, cost-effective, and low-maintenance optical components became available to the lidar community. Coherent detection lidars share many similarities with the high-speed fiber-optic communications. As a result, the new fiber-optic technology was quickly adopted in these lidars. Although coherent detection lidars, especially all-fiber coherent detection lidars, have benefited from the technology available in coherent fiber-optic communications, a considerable gap (in both research and technology) seems to exist between the two. In this thesis, I have presented some of the advances in fiber-optic transceivers, originally developed for high-speed data transmission, and shown how they can be integrated in micropulse and continuous-wave all-fiber coherent detection lidars. The presented technologies not only enable the possibility for performance improvements in existing lidars but also pave the way for the application of coherent detection lidars in areas where their presence was neither plausible nor easy to realize. This thesis, composed of an introduction and four scientific paper and one manuscript, specifically presents the adoption of some of the contemporary fiber-optic communications transceiver architectures in coherent detection lidars. In paper I a new short-range all-fiber coherent Doppler lidar employing an image-reject homodyne receiver is described and demonstrated. In Paper II two different approaches to signal processing, necessary for the estimation of mean velocity from the spectra, are discussed and the associated advantages and disadvantages such as the signal to noise ratio and signal processing overhead are discussed. The performance of the system proposed paper I is put to test in a real measurement campaign the results of which are discussed in Paper III. In Paper IV a patent-pending long-range polarization-diversity coherent Doppler lidar is presented. The system benefits from an improved transmit power (thanks to the availability of two erbium-doped fiber amplifiers separated in polarization) while having the ability to detect the depolarized backscatter signals. The ability to detect the degree of depolarization enables the characterization of aerosol types associated with each measurement range. Eventually, it is shown in Paper V that by adopting the image-reject homodyne receiver in an all-fiber coherent detection lidar, the spectrum of the Rayleigh or the spontaneous Rayleigh-Brillouin scattering (depending on the operating conditions) can be resolved. The system benefits from an eye-safe 1.5μm laser and can provide simultaneous measurements of temperature, pressure, and wind. The focus of the paper in Paper V is the temperature measurement capability of the system, provided as the proof of concept through numerical simulations.

Resumé (Abstract in Danish)

Kohærent detektion lidars (light detection and ranging) har efterhånden udviklet sig betydeligt og er nu *de facto* standarden for måling af vinde i det atmosfæriske grænselæg. De tidligere versioner af disse lidars var voluminøse, dyre og sårbare over for eksterne påvirkninger såsom temperaturvariationer og vibrationer. Men imidlertid har fremskridt indenfor fiberoptisk kommunikation resulteret i en række stabile, kosteffektive, vedligeholdelsesfrie optiske komponenter, som kan anvendes af lidar konstruktører. Kohærent detektion lidars deler nemlig mange ligheder med højhastigheds fiberoptisk kommunikation. Som følge heraf er den nye fiberoptiske teknologi hurtigt blevet anvendt i opbygningen af lidars. På trods af dette halter brugen af disse kommunikations komponenter stadig bagud i anvendelsen til lidars. I denne afhandling har jeg fremlagt nogle af de fremskridt inden for fiberoptiske transceivere, der oprindeligt er udviklet til high-speed data transmission, og vist, hvordan de kan integreres i pulsede og kontinuerlige fiberbaserede kohærent detektion lidars. Teknologierne har ikke alene muliggjort præstationsforbedringer i eksisterende lidarsystemer, men har også banet vejen for anvendelse i nye områder, hvor det ikke før har synes muligt. Denne afhandling, der består af en indledning, fire videnskabelige artikler og en artikel under udarbejdelse, præsenterer anvendelsen af nogle af de moderne fiberoptiske kommunikations-transceiver arkitekturer i kohærent detektions lidars. I artikel I er en ny kortrækkende fiber-baseret Doppler lidar, der anvender "image-reject" homodyn detektion, beskrevet og demonstreret. I artikel II diskuteres to forskellige måder at behandle signaler fra denne type lidar for at estimere vindhastigheder. Fordele og ulemper såsom signal støjforhold og effektivitet analyseres. Det foreslåede lidar system i artikel I bliver testet i en feltkampagne, hvis resultater er diskuteret i artikel III. I artikel IV præsenteres en patentanmeldt langtrækkende "polarization diversity" kohærent Doppler lidar. Systemets fordele er blandt andet en forbedret sendeeffekt (takket være tilgængeligheden af *to* erbiumdoterede fiberforstærkere med ortogonal polarisering) og samtidig evnen til at måle det depolariserede back-scatter. Graden af depolarisering muliggør karakteriseringen af aerosol typer som funktion af afstanden. Til sidst er det vist i artikel V, som er under udarbejdelse, at ved at anvende en "image-reject" homodyn modtager i en fiberbaseret kohærent lidar, kan spektret af den spontane Rayleigh-Brillouin spredning måles. Systemet bruger en 1,5 μm laser, som har den fordel, at den ikke skader det menneskelige øje, og kan i princippet give sammenhørende målinger af temperatur, tryk og vind. Fokus i artikel V er temperaturmålingen, som gennem numeriske simuleringer er vist muligt.

Contents

Preface

This thesis consists of a General Introduction and the following scientific papers which are referred to in the text by their roman numerals:

I. C. F. Abari, A. T. Pedersen, and J. Mann, "An all-fiber image-reject homodyne coherent Doppler wind lidar," Opt. Express, vol. 22, pp. 25880-25894, 2014.

II. A. T. Pedersen, C. F. Abari, J. Mann, and T. Mikkelsen, "Theoretical and experimental signal-to-noise ratio assessment in new direction sensing continuous-wave Doppler lidar," in proc. of J. Phys.: Conf. Ser. **524** 012004 doi:10.1088/1742-6596/524/1/012004.

III. C. F. Abari, A. T. Pedersen, E. Dellwik, and J. Mann, "Performance evaluation of an all-fiber image-reject homodyne coherent Doppler wind lidar," in Atmos. Meas. Tech. Discuss., vol. 8, pp. 3729-3752, 2015.

IV. C. F. Abari, X. Chu, M. Hardesty, and J. Mann, "A re-configurable all-fiber polarization diversity coherent Doppler wind lidar," to be submitted to Opt. Express.

V. C. F. Abari, X. Chu, J. Mann, and S. Spuler, "A micropulse eye-safe all-fiber molecular backscatter coherent temperature lidar," in proc. of the 27th int. laser radar conf. (ILRC 2015), New York, USA, July 2015.

Other relevant publications/Patents by the author

The author of this dissertation is also the main contributor or co-author of the following scientific publications and patents which are related to but not considered part of the dissertation:

I. C. F. Abari, J. Mann, T. Mikkelsen, M. Sjöholm, C. Peucheret, and A. T. Pedersen, "A polarization diversity image-reject homodyne receiver for directional radial velocity measurements in light detection and ranging (lidar) instruments," European Patent Office, Pending Patent, Application no.: 13186157-1812, Dec. 12, 2013.

II. N. Angelou, C. F. Abari, J. Mann, T. Mikkelsen, and M. Sjöholm, "Challenges in noise removal from Doppler spectra acquired by a continuous-wave lidar," presented at the 26th International Laser Radar Conference, Porto Heli, Greece, 25-29 June 2012.

Acknowledgments

Expressing my gratitude to the many people who helped or supported me throughout my PhD requires a book of its own. To state the obvious, I am very grateful to my academic adviser, Jakob Mann. My gratitude to Jakob is not only because of his role as an excellent academic adviser. Jakob has been a great source of motivation and inspiration; he trusted and believed in me and encouraged me to pursue my ideas. His philosophy and professional approach to science has been a guiding light for me.

I lack the words with which to express my many thanks to Xinzhao Chu. Her energy, passion, and dedication to science and engineering always fascinates me. Xinzhao was there for me when most other people were not. She encouraged me to follow through on my thesis during difficult times. If it were not for her support and enthusiasm, I might never have seen the light at the end of the tunnel.

Mikael Sjöholm not only was a sharp, critical, and supportive co-adviser throughout my PhD but also someone whose friendship I cherished during our long commutes to Sweden. He is one of the constant reminders of how lucky I am to have lived, enjoyed, and experienced life in Sweden.

My sincere thanks to Christophe Peucheret for his help and guidance early in my PhD, especially for getting me started with VPIphotonics. My special thanks to Mike Hardesty for inviting me and facilitating my visit at ESRL, NOAA. My gratitude to Scott Spuler for helping me have access to a great research and scientific environment at EOL, NCAR. I am grateful to Anne-Marie Hansen at TEM, DTU, and Tammy Kepple and Maureen Donovan at EOL, NCAR for their invaluable help with administrative work. Many thanks to Poul Hummelshøj for being a manager always careful to be fair and Jacob Berg for the conversations we had. Many thanks also to my numerous friends and colleagues whose friendship and companionship I have enjoyed and whose long list of names I cannot mention here but I will never forget.

Last, but not least, I cannot imagine how I could have finished my PhD without the constant support and inspiration of my beloved wife, Philippa. She affirmed for me that patience and love are the most important virtues, unparalleled by any others. Thank you for being there and letting me share my happy and sad moments with you.

«به پَایَان آمَد اِین دَفتَر حِکَایت همچِنَان بَاقی»
(سَعدی شیرَازی)

"This book has come to an end, but a tale is still to be told"
(Saadi of Shiraz*, The Divan; ghazal 586)

Cyrus F. Abari

*Saadi of Shiraz (1210-1291) was a Persian poet and avid traveler. He spent forty years traveling and experiencing life in the Middle-East, North Africa, and India at the end of which he wrote two books, The Rose Garden (Golestan) and the Orchard (Bustan), about his experiences. Another book by Saadi is his mystical love poetry compiled in Saadi: The Divan. Originally in Persian, The Divan has been translated into English; Paul Smith, Saadi: The Divan, NEW HUMANITY BOOKS, Australia, 2014.

General Introduction

Cyrus F. Abari

1 Introduction

Remote sensing of physical parameters is a very attractive topic in science and engineering. Compared to in situ sensing alternatives, remote sensing has a number of advantages. For instance, the measurement device does not need to be placed at the measurement point of interest. Imagine measuring the temperature inside a very hot industrial oven; There are not many in situ measurement devices capable of enduring the high temperatures in such environments. Sometimes, it is very difficult and even impossible to use an in situ measurement technique to quantify a certain parameter; Measurement of planetary surface temperatures is a good example. Probably, a very important characteristic of remote sensing is the ability to measure a parameter with no or little interference with the measurement medium. For instance, the measurement of atmospheric wind has been well established through the utilization of cup anemometers in the wind energy industry as well as atmospheric science. Despite many advances in cup anemometer design, this instrument interferes with the measurement medium (i.e., the wind field and turbulence structure at the point of measurement).

One of the widely used techniques in remote sensing is the application of light. In passive optical remote sensing, the (emitted light) radiation from a remote object is detected and processed to extract the parameters of interest while gather information about the object's properties or the medium between the source and detector [1] [1]. A very simple example of a passive remote sensing instrument is a camera. In a camera the light emission from an object is collected by the camera lens and further processed by its circuitry to identify certain characteristics associated with the object such as its structure and color. Although passive remote sensing is a very appealing technique, it may have certain limitations. For instance, the instrument has no control over the light source and its properties; A camera is not able to record any pictures in a pitch black environment when in a strictly passive operating mode.

Active optical remote sensing, another class of optical remote sensing techniques, relies on the transmission of a user-controlled light source to illuminate the target. The transmitted light from the source interacts with the object/medium of interest and the result, usually in the form of scattered light, is collected and processed. Light detection and ranging (lidar) belongs to the family of active optical remote sensing techniques. Although lidar is usually known for using a laser source for the purposes of light emission, the early adoptions of lidars involved utilizing an incoherent light source. For instance, [2] employed a simple search light technique for the measurement of air density profile in the upper atmosphere.

Wide adoption of lidars for remote sensing applications grew with the advent of lasers and became popular with their performance improvements [3–5]. Lasers provided the opportunity to generate a light source at a given wavelength which could stay coherent over longer distances. Lasers also provided the opportunity for fine tuning and manipulation of light suited for the application in hand. For instance, by tuning the laser wavelength to the resonance frequency of certain atoms and collecting the resultant radiations, some of their properties can be quantified in a measurement medium of interest; Sodium reso-

[1] For instance, in what is known as the passive differential optical absorption spectroscopy, the sunlight can be used to for the measurement and characterization of gases in the atmosphere.

nance fluorescence lidars have been used to measure and characterize the Na layers in the mesopause [6]. Due to their nature of operation, these lidars are also capable of measuring the motion-induced Doppler shifts [7] which helps to characterize other parameters such as the mesospheric waves [8].

2 Light scattering

In active light (laser) remote sensing, the interaction of the transmitted light and matter (or medium) is characterized to measure the desired parameters. Light interacts with the medium in a variety of ways. For instance, light is scattered by the atmospheric constituents such as aerosols and molecules. Light can also be absorbed by the medium. By measuring the amount or nature of the scattered or radiated light lidars can indirectly measure the sought after quantities. For instance, coherent Doppler lidars (CDL) are designed to measure the motion-induced Doppler shifts which enables the derivation of the target's (radial) velocity. Raman lidars can measure the Stokes and anti-Stokes frequency shifts in the scattered light; One applications is material identification and analysis [9]. Depending on the nature of the interaction between light and medium, the scattering from a target can be classified into two major groups: elastic and inelastic scattering.

2.1 Elastic scattering

Elastic scattering refers to the scattering of light where there is no transfer of internal energy between light and the target. In such cases, the light wavelength does not experience any wavelength change. Two primary examples of elastic atmospheric scattering are Mie and Rayleigh scattering. If the incident wavelength is comparable with the size of the target, such as light scattering by aerosol particles, the phenomenon is known as Mie scattering. The Mie scattering cross-section scales inversely with the laser wavelength. However, since there is a large size and shape distribution of the particles in some measurement mediums (such as the lower atmosphere), the explicit wavelength dependence of Mie scattering cross-section in such media is not known. Instead, empirical modeling and estimation have been carried out for the characterization of Mie scattering cross-section. In the reported results by Sirvastava et al. [10], for instance, the wavelength dependence of the volume cross-section depends on the aerosol loading conditions; For moderate and weak aerosol loading conditions the Mie scattering volume cross-section has a $\beta \propto \lambda^{-2}$ and $\beta \propto \lambda^{-3}$ dependence [2], respectively.

Another elastic scattering phenomenon in the atmosphere or gaseous medium is the Rayleigh scattering. Rayleigh scattering, also known as single molecular scattering, is the result of scattering by the constituent molecules. In pure Rayleigh scattering, the thermal motion of individual molecules are responsible for the observed Doppler shifts in the scattered light. Due to the random nature of the motions, the Doppler spectrum is known to have a Gaussian (or quasi Gaussian) profile [7]. Besides, unlike Mie scattering, the Rayleigh scattering cross-section has a well-known dependence on the incident wavelength. In other words, it can be shown that for a pure Rayleigh backscattering, i.e., a scattering

[2] β and λ represents the volume scattering coefficient and wavelength.

angle of π, the volume scattering cross-section is [7]

$$\beta(\pi, \lambda) = 2.938 \times 10^{-32} \left(\frac{P}{T}\right) \frac{1}{\lambda^{4.0117}}, \tag{2.1}$$

where λ is the wavelength, P is the pressure, and T is the temperature in SI units. Equation (2.1) has been used in combination with the U.S. Standard Atmospheric model [18] for the numerical simulations presented in Papers IV and V in this thesis.

The normalized Doppler spectrum associated with the Rayleigh scattering follows a Gaussian distribution and can be expressed as [11]

$$S(f - f_c) = \sqrt{\frac{1}{\pi a K}} \exp\left(-\left[\frac{2\pi(f - f_c) - \boldsymbol{K} \cdot \boldsymbol{u}}{aK}\right]^2\right), \tag{2.2}$$

where f_c is the carrier (laser) frequency, and $\boldsymbol{u}$ and $a = \sqrt{2k_B T/M}$ (with M being the molecular mass) are the mean and most probable gas velocities, respectively. Furthermore,

$$K = \frac{4\pi \sin(\theta_s/2)}{\lambda} \tag{2.3}$$

is the magnitude of the interaction wave vector where θ_s is the scattering angle and $\boldsymbol{K} = \boldsymbol{K_s} - \boldsymbol{K_o}$ ($\boldsymbol{K_o}$ and $\boldsymbol{K_s}$ being the wave vectors of the incident and scattered light).

Since the power of Rayleigh scattering (depending on the volume scattering cross-section of the molecules) is predictable in the atmosphere, see (2.1), it is considered to be a much more reliable and predictable scattering target, when compared with aerosols. For instance, if remote sensing of a certain parameter (such as wind speed) needs to be carried out at high altitudes (in the lower atmosphere), Rayleigh scattering can provide a reliable signal for the analysis of the wind-induced Doppler shifts. The presence of aerosol-like particles at those altitudes is variable and depends on the region, altitude, weather condition, etc.

2.2 Inelastic scattering

Inelastic light scattering is identified by an energy transfer between the incident light and target, or medium. In laser-induced fluorescence spectroscopy, the laser at a given wavelength is impinged on a medium (usually solids and liquids having a broad absorption and emission spectra due to the inter-molecular interactions). The transmitted laser is partially absorbed by the target resulting in excitation of electrons into higher energy levels. A transition back to lower energy ground states in the form of radiation is detected and characterized to identify or measure certain parameters in the target. In resonance florescence lidars, the laser wavelength is tuned to the absorption lines of certain atoms and ions. By measuring the volume cross-section the density and nature of such constituents can be measured. Other examples of inelastic scattering are rotational Raman [12], vibrational-rotational Raman [13], and spontaneous Brillouin scattering [3].

[3] Strictly speaking spontaneous Brillouin scattering is considered an inelastic scattering process. However, since the spectral frequency shifts due to energy transfer between light and sound waves is usually small, especially in gaseous media, it is sometimes treated as an elastic process. This is especially true in the event of spontaneous Rayleigh-Brillouin scattering discussed further on in this section.

2.3 Spontaneous Rayleigh-Brillouin scattering

Spontaneous Brillouin scattering (an inelastic scattering) is the result of interaction and energy transfer between photons and phonons, i.e., light and sound waves. In other words, the thermally excited acoustic waves in a medium result in light scattering which undergoes a certain amount of frequency shifting, proportional to the frequency of the scattering fluctuations [14]. As a result of spontaneous Brillouin scattering (SBS), the molecular scattering might exhibit Brillouin side-peaks in its spectrum. The combined effect of Rayleigh and SBS is known as the spontaneous Rayleigh-Brillouin scattering (SRBS) and has become a very attractive research topic for the characterization of gaseous media, including the lower atmosphere [15].

The spontaneous Brillouin side-bands become more dominant at higher gas densities [16]. Depending on the relationship between the illuminating laser wavelength and the gas density in the measurement volume, the scattering in the medium can be classified into three regimes. If the laser wavelength is much smaller than the mean free path in the gaseous medium, the scattering is pure Rayleigh; This is known as the Knudsen region [15] and the spectrum can be described by (2.2). The reason behind a pure Rayleigh scattering in Knudsen region can be associated with the fact that at low gas densities the scattering is "solely due to individual thermal molecules" [16]. If the illuminating laser wavelength is much longer than the mean free path, then the scattering is known to happen in the hydrodynamic regime. In this region, the collisional effects between the molecules are dominant. The transition regime from Knudsen to hydrodynamic is known as the kinetic regime. To quantify these scattering regimes a dimensionless parameter y is defined as the ratio between the scattering wavelength and the mean free path in the medium, i.e., [16]

$$y = \frac{nk_BT}{Ka\zeta\nu}, \tag{2.4}$$

where n is the number density and ζ is the shear viscosity. Rye [15] has shown that (2.4) can be modified such that for a scattering angle of $\theta_s = \pi$ in the atmosphere

$$y = \frac{\lambda\,(T + 111P)}{4.34T^2}, \tag{2.5}$$

where λ is the wavelength of the incident light in nm and P is the pressure in Pa.

To derive the SRBS spectrum the collisional cross-sections should be taken into account (and modeled) [11]. Two of the best mathematical models for SRBS are Tenti's S6 and S7 models [17]; These models demonstrate a very good fit between the model and the experimental data [16]. In atmospheric measurement, SRBS can be adopted to help carry out remote sensing of atmospheric temperature, pressure, and even wind. Rye [15] has shown that the Brillouin side-bands in SRBS can be used for the estimation of temperature. In fact, an accurate estimation of the SRBS can help derive the wind speed, pressure, and temperature simultaneously. Although the presence of side-bands in the SRBS (a structured spectra) can facilitate a more accurate estimation of the desired parameters, especially temperature, theoretically a pure Rayleigh spectra, encountered in Knudsen region, should suffice. Following Tenti's S6 model [17], the SRBS spectra for a few wavelengths and altitudes (with respect to the sea level) are plotted in Fig. 1. These

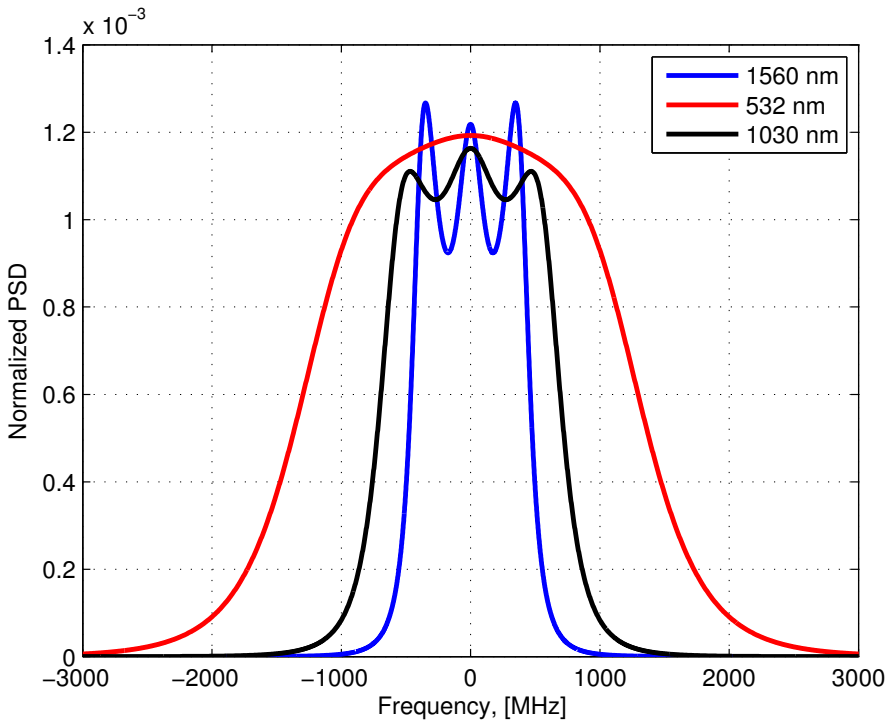

Figure 1: The normalized power spectral density (PSD) associated with the SRBS scattering for three different wavelengths. These plots have been calculated for an altitude of 1 km with respect to the see level. Tenti's S6 [17] and the U.S. Standard Atmospheric model [18] have been used for the calculation of the spectra.

plots have been calculated using the Tenti's S6 model [17] and the parameters from the U.S. Standard Atmospheric Model [18].

3 Lidars for active remote sensing

As mentioned in Sec. 1, lidars provide an attractive means for the remote sensing of physical parameters, especially in atmospheric science. Lidars can be realized in various configurations. Bi-static lidars, for instance, are built such that the transmitter and receiver optics are not co-located. In co-axial mono-static lidars, such as in coherent Doppler lidars (CDL), the transmitter and receiver optics see the same optical path. Depending on the principle of light detection, lidars are grouped as either direct detection or coherent detection lidars. Lidars can also be classified according to the physical process they are designed to identify and measure, e.g., Raman lidars and Doppler wind lidars.

Irrespective of their configuration and principle of operation, all lidars have five main building blocks [19], i.e., a light source, transmitter optics, receive optics, photodetector, and electronics for signal treatment and data processing. Many of the lidars are designed to measure the backscattered light from the target. To be able to estimate the expected amount of the collected signal backscatter from a certain range, a mathematical model needs to be adopted. For a mono-static lidar measuring the backscatter signal the generalized lidar equation can be expressed as

$$E_r = \eta\beta\left(\lambda_l, \lambda_r, z\right) G(z) T_{a1}(\lambda_l, z) T_{a2}(\lambda_r, z) E_s \left(\frac{A\Delta z}{z^2}\right), \tag{3.1}$$

where η is the lidar optical efficiency, E_s and E_r are the transmit and receive signal energies, β is the volume backscatter coefficient, $G(z)$ is a geometric factor, λ_l is the transmit laser wavelength, λ_r is the received signal wavelength, A is the receiver telescope apperture area, z is the distance to the target, Δz is the measurement range gate, and T_{a1} and T_{a2} are the one-way transmittance of the atmosphere for the transmit and receive wavelengths (λ_l and λ_r), respectively. Please note that (3.1) represents the expected optical backscatter power for a specific range and system configuration.

In elastic and quasi-elastic scattering (e.g., SRBS), there is no tangible change of wavelength in the scatter signal (compared to the transmit signal) and as a result $T_{a1} = T_{a2}$ in (3.1).

3.1 Coherent detection

In many lidar systems the received signal power is directly detected by the photodetector. In such systems, aside from (design-based[4]) optical filtering, the received signal is largely intact when impinged on the photodetector. As a result, the photodetector measures the amount of the received optical power from which the parameter of interest is estimated. In these systems the detection process at the photodetector level is often known as photon-counting since the collected optical power is very low; The variance

[4]In some systems atomic filters may be used to remove the Mie scattering from the received signal. In some others, an optical filter such as Fabry-Perot interferometer may be used as a frequency discriminator.

of the estimated parameter depends on counting each individual photons. For instance, in resonance fluorescence lidars, the amount of (number of photons in) backscatter light from a certain range at a predetermined wavelength is measured. In a Fabry-Perot (FP) etalon-based Doppler lidar [16], the FP acts as a frequency discriminator and, operating in concert with the direct detection PD, provides a picture of the received (optical) signal spectrum.

In coherent detection, the phase/phasor of the received signal (collected optical signal) is compared against a reference signal. Phase comparison is a simplistic way of defining coherent detection. In the jargon of lidars, radio systems, and optical communications, coherent detection specifically refers to mixing (also known as beating)[5] the received and reference signals such that the information carrying spectral region in the signal is translated into a lower frequency band for detection and analysis. The down-conversion (translation) of the signal into a lower frequency band is imperative if a high-resolution spectra from the signal is desired. This is mainly due to the fact that the available electronic components such as PDs, amplifiers, analog-to-digital converters (ADC) have a very limited bandwidth (BW) and cannot follow the fast signal fluctuations in the vicinity of the carrier frequency [6].

A requirement for coherent detection in lidars is spatial and temporal coherence between the receive and reference signals, thus coherent detection. Due to the desirable properties of the zeroth transverse electromagnetic mode in lasers (TEM00), it is used as the transmit signal in the majority of lidars. Due to the requirement on the spatial coherence in coherent detection, the received signal should also be of TEM00. As a result, it has been shown that in mono-static coherent detection the transmitter and receiver optics should be coaxial [20].

The mixing (beating) of the receive and reference signal occurs on the PD surface. The PD responds to the optical intensity fluctuations of the mixed signal (interference). As a result, imagine a complex-valued transmit signal

$$s(t) = \sqrt{P_o} \exp\left(-2j\pi f_c t\right), \tag{3.2}$$

where P_o is the power of the transmit signal and f_c is the carrier (laser) frequency. If the receive signal is

$$r(t) = \sum_{k=1}^{L} x_k(t) \exp\left(-2j\pi f_c t\right), \tag{3.3}$$

$x_k(t)$ is the kth scattered signal component in baseband (i.e., where the carrier frequency has been removed), and L is the number of scattering constituents (e.g., molecules or aerosols) and

$$l_o(t) = \sqrt{p_{lo}} \exp\left(-2j\pi f_c t\right), \tag{3.4}$$

[5]It is common in lidar literature to refer to coherent detection as heterodyning. In my humble opinion, this is a bad adoption of a technical terms as, strictly speaking, heterodyning refers to a specific class of coherent detection techniques for the translation of information-carrying signals to a lower frequency band.

[6]Carrier frequency usually refers to the frequency of the transmit signal. For radio signals it can be in the MHz and GHz region while for optical signals, such as lasers, it is in the THz region.

is the reference signal with power p_{lo}, then

$$i_D(t) = R_D \left|r(t) + l_o(t)\right|^2 + \omega_t = R_D \left[\left|r(t)\right|^2 + \left|l_o(t)\right|^2 + r(t)\overline{l_o(t)} + \overline{r(t)}l_o(t)\right] + \omega_t, \quad (3.5)$$

where R_D [A/W] is the detector responsivity, ω_t is the total noise[7], and $\overline{(\cdot)}$ denotes the complex conjugate operation. After some mathematical manipulation and simplifications (3.5) can be written as

$$i_D(t) = R_D\sqrt{p_{lo}} \left[\sum_{k=1}^{L} x_k(t) + \sum_{k=1}^{L} \overline{x_k(t)}\right] + i_{DC} + \omega_t, \quad (3.6)$$

where i_{DC} is a direct current with an amplitude proportional to the sum of $r(t)$ and $l_o(t)$ signal powers. Please note that by going from (3.5) to (3.6) we have ignored the signal components with a spectrum in the vicinity of the carrier frequency as they are effectively filtered out by the PD (due to its limited BW). As we can see, coherent detection translates the passband receive signal $r(t)$ to a baseband signal $i_D(t)$ which can be digitized and processed by the available electronics.

3.2 Coherent Doppler lidars

Coherent Doppler lidars (CDL) are a specific class of coherent detection lidars where the task is to detect and estimate the Doppler information from the receive signal. A primary example of Doppler lidars is the coherent Doppler wind lidars (CDWL) where the wind-induced Doppler shifts (on the scattered light) is estimated. CDLs are not limited to wind lidars; Theoretically, they can detect Doppler shifts associated with the thermal motion of individual molecules in Rayleigh scattering.

CDWLs have been used for remote sensing of wind in the atmospheric boundary layer for the past few decades [21]. The first systems benefited from gas and later solid-state lasers [22], as the primary light sources. Due to the stringent eye-safety requirements, the lidars employed in atmospheric remote sensing applications are designed around infrared (IR) lasers beyond 1.35 μm wavelengths [23] where the maximum permissible eye exposures is orders of magnitude higher than the visible and near IR wavelengths. The CO_2 and solid-state operated lidars are examples of IR CDWLs designed at 10.59 and 2.1μm laser wavelengths.

The gas and solid-state CDWLs, mainly built on open-space optics, are usually bulky, high-maintenance, and costly. The main issue in such systems is the generation and stabilization of the laser which requires optical and mechanical components with a relatively large form-factor. Besides, the transmitter and receiver optics in such systems are based on open-spaced optics and occupy a relatively large space too. Moreover, to maintain the designed optical path and system configuration the system should be isolated from environmental effects such as vibration and thermal fluctuations. An advantage of such systems is the availability of large optical energies in the transmit pulse (due to the nature of the laser source and its design). Optical energies of up to 1 J have been reported in CDWLs [22].

[7]The additive noise at the output of the PD (in coherent detection) is comprised of a few components. The dominant noise term is the detector's shot noise which is ideally white.

3.3 All-fiber coherent Doppler lidars

It is not far fetched to claim that with the advent of fiber-optic technology, optical communications experienced a Renaissance. The optical fibers act as a waveguide for the transmission of optical signals with a minimum amount of signal attenuation and distortion. Due to their nature, the silica glass optical fibers attain their minimum optical attenuation around 1.5μm wavelength. This revolution in fiber-optics has given rise to a larger number of high quality and cost-effective lasers and fiber-optic components at 1.5μm. For instance, fiber (and semiconductor) lasers with a very narrow linewidth (i.e., very low phase noise) and high output power stability are available. These lasers are not only much more cost-effective but also much more compact, when compared with the solid-state and gas lasers. Furthermore, these lasers are usually available as off-the-shelf components.

Besides high quality laser sources, fiber-optic amplifiers are also available with relatively small noise figures and sufficient amplifications. Erbium-doped fiber amplifiers (EDFA) are examples of fiber-optic amplifiers at 1.5μm wavelengths. In pulsed applications, these amplifiers provide pulse energies in the μJ region (generating mJ signal levels in single-mode EDFAs is very challenging); The μJ pulse energies are the reason why such systems are called micropulse lidars. A relatively small fiber core and presence of amplified spontaneous emission (ASE) are examples of factors limiting the available pulse amplification in such systems [24]. However, due to a high pulse repetition rate (PRR) in such systems, these amplifiers sustain an average output power of a few Watts which is comparable with the output power of the bulkier and larger laser options.

The lidar community quickly adopted the available 1.5μm technology and utilized that in a number of different lidars. For instance, all-fiber CDWL have been extensively employed in wind energy industry for the remote sensing of atmospheric wind. Examples of these systems are ZephIR 300 from ZephIR Lidar [25] and WindCube from Leosphere [26]. Due to their robust operation and small form-factor, these systems can be deployed as ground-based, airborne, or turbine-mounted lidars [27]. The short-range CDWL [28] developed at the National Center for Atmospheric Research (NCAR) is an example of an airborne all-fiber CDWL.

3.4 Transceiver architectures in coherent lidars

In all-fiber CDLs, the generation, manipulation, and transmission of laser light is largely carried out by fibers or fiber-based components. For instance, in ZephIR CDWLs [25], either a fiber-based laser or fiber-coupled semiconductor laser is responsible for the generation of a high-quality diffraction-limited laser at 1.5μm. Application of a low-power but high-quality laser source to drive an optical amplifier (for boosting the optical power) is known as master oscillator power amplifier (MOPA) configuration. The majority of all-fiber CDLs benefits from such a configuration. The output signal, i.e., the amplified laser is fed into the telescope through an optical circulator which provides a high isolation between the transmit and receive signals. The collected backscatter signals from the target are collected by the telescope and transmitted through optical fibers to the receiver for detection and further processing.

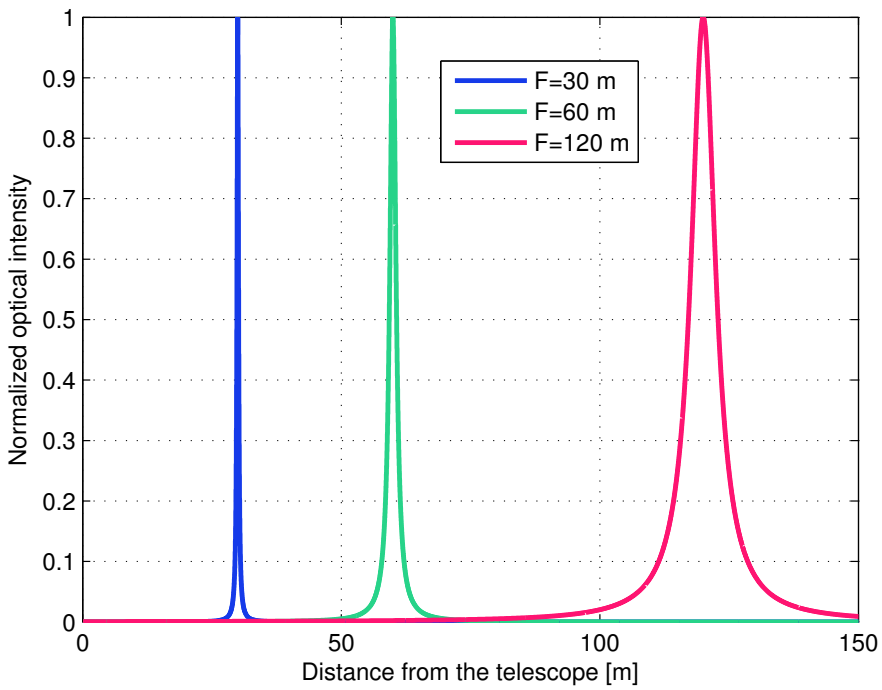

Figure 2: The amplitude-normalized optical intensity for various focus distances. The calculations have been done following (3.7) for $D = 10$ cm and $\lambda = 1560$ nm.

The above mentioned system is an example of (what is known as) continuous-wave (CW), short-range, or narrowband CDWLs. In such systems, the transmitted signal is not pulsed but a CW laser, i.e., a continuous transmission of the optical signal towards the target. Due to a CW transmission of the light, range gating (a procedure used in pulsed CDLs for ranging) cannot be carried out in such systems. Instead, the laser needs to be focused on the range of interest for the measurement resulting in a sampling volume which is range-dependent [29]. The capability of the system to provide a tight focus on the target plane depends on the transceiver optics, wavelength, as well as the range. As a result, the range-dependent optical signal intensity in such systems can be incorporated in the generalized lidar equation, i.e., (3.1), such that A becomes a range-dependent effective telescope output lens area [29–31]

$$A_{\text{eff}}(z) = \frac{\pi D^2}{4}\left[1 + \left(\frac{\pi D^2}{4\lambda z}\right)^2 \left(1 - \frac{z}{F}\right)^2\right]^{-1}, \tag{3.7}$$

where D is the diameter of the lens, λ is the wavelength, and F and z are the focus distance and range from the telescope output lens, respectively. Fig. 2 shows examples of amplitude-normalized range dependent optical intensities at the output of a CW CDWL for various focus distances from the telescope output lens; It is evident from this figure that CW systems operate best for short measurement distances as the sampling volume increases quadratically as a function of focus distance.

In another class of all-fiber CDLs, the transmitted signal is pulsed. Pulsed lidars are probably the most widely used lidars as they provide the opportunity for measurement at longer distances while providing a consistent sampling volume across the measurement range. In these (MOPA) systems, the output of a CW laser source, known as master oscillator (MO), is chopped and fed into an EDFA for amplification. The pulse train is subsequently transmitted through the atmosphere or the desired measurement medium. WindCube from Leosphere [26] is an example of pulsed, also known as long-range, all-fiber CDWL.

As shown by (3.5) an essential operation in coherent detection systems (including the short and long-range CDLs) is beating the backscatter signal with a reference signal known as local oscillator (LO). Although deriving the LO from the same laser source in a CDL is not strictly needed [8], LO is usually derived from the MO in the majority of CDLs for convenience. Besides, in both systems the mixing and treatment of the receive signals can be carried out in a variety of ways. For instance, the Doppler bearing signal can be directly translated into baseband, i.e., the carrier frequency (or any system-induced frequency offset) is completely eliminated in the resultant signal. In other words, any observed frequency shift is purely due to the physical process such as Doppler or Brillouin frequency shifts.

The treatment of the receive signal and mixing it with the LO is usually carried out by what is known as the optical front-end. As the name implies, the front-end is the first stage at the receiver (receiving the collected backscatter signal from the telescope).

[8] For instance, Schwiesow and Cupp [32] have shown that LO can be taken from a different laser as long as there is temporal and spatial coherence between the receive and LO signals.

Depending on how the system treats the receive and LO signals at the optical front-end, a few front-end (more broadly speaking transceiver) architectures can be realized.

Homodyne receivers, also known as direct-conversion receivers, completely remove the carrier frequency from the receive signal and translate it into baseband. Carrier frequency is often used in reference to the frequency of the optical transmit signal. In one instance of homodyne receivers (adopted in all-fiber CDWLs), the LO signal is taken from the end facet of the delivery fiber at the input to the telescope. The amount of the LO power is controlled by changing the angle of the end facet of the fiber [30]. This specific homodyne acthitecture is called a homodyne receiver with real-mixing [33]. In homodyne receivers with complex mixing (also known as image-reject homodybe receivers or quadrature-detection homodyne receivers) the backscatter signal is divided into two equal components. One component is mixed with the original LO while the other component is mixed with the phase-shifted (90^0) version of the LO.

Another conventionally employed optical front-end architecture is called the heterodyne receiver. This is probably the main reason why CDLs are also known as heterodyne lidars as the early adoption of such systems was based on this front-end architecture. In these systems, either the transmit or LO signal experiences a certain frequency shift (offset) which is within the detection BW of the PD. Thus, the detected signal has a fixed frequency offset with respect to the 0th frequency component. In such systems, the output of the PD is directly sampled by the ADC. The sampling frequency of ADCs should be large enough to satisfy the Nyquist sampling criteria imposed by the BW of the received signal as well as the induced frequency offset. These systems are usually known as heterodyne receivers with intermediate frequency (IF) sampling in literature [33] as the signal is directly sampled at the output of the PD [9]. Probably, one of the primary reasons for the popularity of this architecture is the fact that most long-range CDLs benefit from an acousto-optic-modulator (AOM) [34] for pulse generation and shaping; AOMs provide a high on/off extinction ratio needed for optimal performance of pulsed EDFAs. Due to their principle of operation AOMs also cause a frequency shift in the output signal which is responsible for the IF offset at the receiver.

Another class of optical-front ends in CDLs is superheterodyne receivers. These receivers are probably the oldest and most robust receivers used in radio systems [33]. A superheterodyne receiver is in principle a two-stage receiver where the information carrying signal is first translated into IF band and, after proper filtering and treatment, is eventually down-converted to the baseband. Effectively, this system is a hybrid between a heterodyne receiver with IF sampling and a homodyne receiver (usually) with complex mixing. A benefit of this front-end architecture is the reduction in the BW and sampling frequency of the ADCs. In CDLs, the first down-conversion stage occurs at the PD level and the second down-conversion stage, i.e., complex homodyning is carried out by an RF electronic component (mixer) commonly used in radio systems. In this thesis, I have shown that by adopting some of the recent advances in fiber-optic technology, commonly used in fiber-optic communications, all-fiber CDLs can be improved beyond what has been available to research community and industry. For instance, in Paper I a new short-range all-fiber CDL employing an image-reject homodyne receiver is described and

[9] The sampling is carried out after proper amplification and filtering of the signal from the PD.

demonstrated. In Paper II two different approaches to signal processing, necessary for the estimation of mean velocity from the spectra, are discussed and the associated advantages and disadvantages such as the signal to noise ratio (SNR) and signal processing overhead are discussed. The performance of the system proposed in Paper I is put to test in a real measurement campaign the results of which are discussed in Paper III. In Paper IV a patent-pending long-range polarization-diversity CDL is presented. The system benefits from an improved transmit power (thanks to the availability of two EDFAs separated in polarization) while having the ability to detect the depolarized backscatter signals. The ability to detect the degree of depolarization enables the characterization of aerosol types associated with each measurement range. Eventually, it is shown in Paper V that by adopting the image-reject homodyne receiver in an all-fiber coherent detection lidar, the spectrum of the Rayleigh or the SRBS (depending on the operating conditions) can be resolved. The system benefits from an eye-safe 1.5μm laser and has the potential to provide simultaneous measurements of temperature, pressure, and wind. The focus of the paper in Paper V is the temperature measurement capability of the system, provided as the proof of concept through numerical simulations.

4 Summary of included papers

The papers included in this thesis present the scientific research as well as the experimental activities, where relevant, carried out during the course of my PhD. This section is intended to provide a brief but informative insight into the content of each paper. The reader will have a first glimpse of the intended scientific and practical purpose of each paper where the unnecessary details are omitted and the main concepts and conclusions are presented.

4.1 Paper I - An all-fiber image-reject homodyne coherent Doppler wind lidar

Direct-conversion (homodyne) receivers are a familiar concept in radio systems and coherent optical communications. These receivers help translate the information carrying signal, spectrally spread around the carrier frequency, to the baseband (0-frequency). Up until recently, the commercial and research continuous-wave coherent Doppler lidars benefited either from a simple homodyne receiver (homodyne receiver with real mixing) or a heterodyne receiver with intermediate frequency (IF) sampling; The former suffers from the inability to detect the sign of the Doppler signal while the latter exhibits problems associated with additional noise and bandwidth inefficiency. In this paper, we show that by adopting an all-fiber image-reject homodyne receiver (homodyne receiver with complex mixing) it is possible to build a new generation of CDLs where the system can benefit from the advantages of a directional direct-conversion receiver. The result is a system that has better noise behavior, detection accuracy, and more efficient bandwidth when compared to its heterodyne counterpart. It is also shown that by employing a cross-spectral analysis, made available due to the presence of two detected signal components with independent noise sources, a rather signal-processing-intensive operation (noise whitening) required for accurate retrieval of mean wind speeds from the spectra in such systems, can be eliminated. The paper starts with a theoretical study and analysis of the system and is wrapped up with the system description of a prototype. Some preliminary measurements from lab experiments, as the proof of concept, are also presented in the paper.

4.2 Paper II -Theoretical and experimental signal-to-noise ratio assessment in new direction sensing continuous-wave Doppler lidar

One of the advantages of the image-reject homodyne receiver, discussed in Paper-I, is the ability to eliminate the noise-whitening process for an accurate wind retrieval. The proposed method is to carry out a cross-spectra analysis between the in-phase (I) and quadrature-phase (Q) components of the detected signal which allows the removal of the independent noise sources (such as shot noise) from the signals. This operation allows a theoretical signal-to-noise ratio (SNR) [10] close to infinity. However, we have debated in Paper-I that contrary to the well-known general notion of the SNR, i.e., the power of the detected signal to the power of shot noise, wind retrieval from the Doppler spectrum is sensitive to the signal-to-estimation-noise-ratio (SENR). SENR, a frequency dependent parameter, can be thought of the mean signal power to its variance for each frequency component. In this paper, we have analytically calculated the SENR for different scenarios: the SENR in the event of an auto-spectrum and cross-spectrum. The results are supported by measurements in the lab and indicate that the SENR in the event of cross-spectral analysis drops by a factor of $\sqrt{2}$, when compared to the auto-spectrum approach. Despite the $\sqrt{2}$ reduction in SENR, it is still recommended to employ the cross-spectral approach in the majority of the cases [11] the cross-spectral approach is chosen over the auto-spectrum. Noise whitening, a process required in auto-spectrum approach, is signal processing intensive and may introduce additional estimation noise. Besides, the merits of the cross-spectral approach are not limited to the elimination of shot-noise sources; Any uncorrelated noise source (such as $\frac{1}{f}$ noise) is removed once this procedure is revoked which adds to the accuracy of Doppler estimation from the noisy spectrum, especially around the zero frequency.

[10] It is very common in coherent detection to define the SNR as the power of the detected signal divided by the power of the detector shot noise.

[11] In Paper III it is shown that in a very specific measurement scenario where the Doppler spectrum crosses the zero frequency, i.e., both positive and negative Doppler signals are presented in the measurement volume, the cross-spectrum fails to provide a reliable measurement of t he mean wind speed.

4.3 Paper III -Performance evaluation of an all-fiber image-reject homodyne coherent Doppler wind lidar

Papers I and II discussed the idea behind an all-fiber image-reject homodyne coherent Doppler wind lidar. The system architecture was proposed and performance analysis were carried out both analytically as well as experimentally (through a few measurements in the lab). The main question, however, was still at large; How does the new system stack up against the CW CDL benefiting from a heterodyne receiver with IF sampling (1st-generation Windscanners), a well-established and widely used research lidar at the department of Wind Energy, Technical University of Denmark. It was a well-known fact that this system suffered from noisy behavior around the 0 radial wind velocity, i.e., the IF frequency. The spurious effects around this frequency, make an accurate estimation of wind velocities close to zero very challenging (and sometimes even impossible) as the Doppler signal retrieval in this region cannot be performed accurately. The measurement of close-to-zero velocities is especially important when measuring the vertical component of surface winds.

In this paper, the results of a specific measurement campaign are reported. In this campaign the lidar was deployed to measure the vertical component of the wind in the field. The results are compared against a sonic anemometer as the reference instrument. Besides, the results of another measurement campaign carried out in the past, where a heterodyne receiver with IF sampling was employed, are presented in this paper. The comparison between the probability distribution function (PDF) of the velocities indicate a significant improvement in the vertical wind component measurement capability of the prototype lidar.

Moreover, the performance of two spectral processing procedures, i.e., the auto-spectral and cross-spectral algorithms, are analyzed in the context of the vertical wind component measurement. It is shown that despite the merits of the cross-spectral processing, it cannot provide a full picture of the Doppler spectrum in very specific cases; In case both positive and negative Doppler components are present in the measurement volume the detected spectrum by this method can be biased. This is a rather special and rare occurrence and is expected in measurement scenarios where the mean wind speed is close to zero (such as the surface wind vertical component measurement). Moreover, the probability of its occurrence is expected to increase in the event of larger sampling volumes or more turbulent flow.

4.4 Paper IV - A re-configurable all-fiber polarization diversity coherent Doppler wind lidar

Long-range (pulsed) coherent Doppler lidars have a long history of application in atmospheric science and wind energy for the characterization of wind fields. The earlier versions of such systems benefited from gas and solid-state lasers as well as open-space optics. Recently, a number of all-fiber long-range systems have become available which provide compact, low-maintenance, and cost-effective solutions with a performance that rivals or even supersedes the more expensive non-fiber based counterparts. However, similar to the all-fiber short-range (continuous-wave) systems, a gap between fiber-optic technology used in fiber-optic communications and long-range coherent Doppler lidars seems to persist.

In this paper, a dual-polarization image-reject homodyne optical front-end, originally built for high-speed fiber-optic communications, is adopted. Furthermore, it is shown that by making certain modifications to the transmitter part of the conventionally available systems, a more capable lidar can be built. The lidar's performance and capabilities improve manyfold. For instance, due to the presence of a dual-polarization optical front-end, the system is capable of recording the target (atmospheric) induced depolarization. The ability to detect the signal depolarization makes it possible to retrieve more information about the nature of the target (i.e., the aerosol particles). By measuring the amount of the depolarization it is possible to get some insight about the particle type and size distribution associated with different measurement ranges.

Another advantage of the proposed system is the possibility to integrate two independent optical amplifiers in the system; The amplifiers are configured for the two orthogonal polarization states and operate in concert. Depending on the configuration of the system, which can be changed on the fly, the amplifiers can be combined to double the optical output power or the pulse repetition rate (PRR). Contingent on the lidar deployment and measurement scenario, the system can be configured in real-time to maximize the performance.

4.5 Paper V - A micropulse eye-safe all-fiber molecular backscatter coherent temperature lidar

Remote sensing of atmospheric temperature has been a challenging topic in atmospheric science and more recently wind energy. A variety of methods have been adopted for this purpose. Examples of non-lidar based systems are radiosondes and microwave radiometers. A variety of lidars have also been designed and deployed for remote sensing of temperature. The adopted lidar technologies, however, are usually expensive, bulky, and require high-maintenance. Due to the nature of atmospheric temperature measurement, the lidars need to rely on elastic or inelastic molecular backscattering. For instance, rotational Raman lidars measure the temperature-induced Raman shifts and high spectral resolution lidars (HSRL) take advantage of the temperature-dependent spectral broadening from atmospheric molecules. Both these systems are designed for submicron optical wavelengths due to design and physical process requirements.

Application of coherent lidars for recording the molecular spectral broadening has already been suggested in literature. Nevertheless, the idea never picked up. One of the main problems associated with coherent detection is the restrictions imposed on the applicable wavelengths in such systems; it is very challenging and costly to design high quality optical components, meeting the requirements of coherent detection, for sub-micron wavelengths. Wavelength above 1.4μm, conventionally used in coherent lidars, have a very weak Rayleigh scattering cross-section. However, these wavelengths can operate in a regime where the scattering is not pure Rayleigh but consists of spontaneous Rayleigh-Brillouin scattering (SRBS). The presence of Brillouin peaks in SRBS are good indicator of temperature and can be utilized to overcome the low backscatter signal power needed for an accurate estimation of the temperature.

Besides, in light of the recent advances in optical font-ends (such as the image-reject homodyne receiver) as well as wide-band photodetectors and electronics, it is shown that it is possible to build an eye-safe micropulse coherent lidar capable of remote sensing of atmospheric temperature at mesoscale. The presented results provide a proof of concept through Monte-Carlo numerical simulations.

5 Outlook

All-fiber coherent lidars have been gradually closing the gap with the coherent fiber-optic communications. A mature research base and technology infrastructure in fiber-optic communications can benefit the lidars; It can help develop robust, efficient, cost-effective, and compact lidars for remote sensing applications. In this thesis it is shown how some of the available fiber-optic technology associated with optical front-ends can be adopted in coherent lidars for an improved measurement performance. In these systems the standard off-the-shelf components built for 1.5μm fiber-optic communications were (or suggested to be) used to build the instrument. However, some of these components can be optimized for all-fiber coherent lidars.

Although 1.5μm wavelength has become the de facto standard in all-fiber CDLs, other all-fiber alternatives operating at other wavelengths can be realized. For instance, successful realization of thulium-doped all-fiber amplifiers for integration into master oscillator fiber amplifiers (MOPA) systems, similar to the reported systems in this thesis, has been reported in literature [35]. The reported numbers (distortion-free average output power of 210 W) in [35] surpasses any erbium-doped fiber amplifier at 1.5μm. The 2.1μm thulium-doped amplifier not only provide optical powers beyond what is achievable with erbium-doped fiber amplifiers at 1.5μm but also enable realization of coherent temperature lidars relying on SRBS for higher altitudes requiring opto-electronic components with lower BW requirements; The SRBS BW scales inversely with respect to the laser wavelength.

In this thesis, it is shown that an all-fiber polarization diversity receiver can be adopted in a pulsed CDL to, among other things, acquire additional information about the depolarized signal backscatter from different ranges. The same front-end can be adopted in a CW system not only for depolarization characterization of the backscatter light but also for cloud detection and removal. A challenging task in CW CDLs is the presence of clouds or other objects in the beam path having a higher reflectivity or scattering cross-section. The available systems usually employ complicated signal processing algorithms for the detection and removal of the clouds. Since clouds usually introduce a certain amount of light depolarization in the backscatter signal, a polarization diversity optical front-end can discriminate the backscatter signal from the clouds, eliminating the need for signal-processing-intensive algorithms which might introduce uncertainty rendering some acquired data invalid.

Another potential architecture in all-fiber coherent lidars is a frequency-diversity system. The frequency-diversity system provides the opportunity to perform a simultaneous measurement carried out at multiple heights simultaneously. Although a frequency-diversity system as such has been reported in literature [36, 37], the reported system suffers from excess amplifier noise due to its design. However, modified designs based on a limited frequency hopping scheme, where the transmit pulses are frequency shifted through an electro-optic modulator (e.g., Mach-Zehnder modulator), can be adopted. Thanks to an additional range isolation from frequency separation in the transmitted pulse train, these systems will provide the opportunity to carry out the measurements at multiple heights simultaneously.

Advanced digital signal processing is another area in radio systems and fiber-optic

communications which has been exhaustively researched and developed. Digital signal processing techniques enable us to improve the estimation of parameters for a given system configuration and detected signal quality. Besides, they can provide the chance to eliminate or reduce the effect of spurious effects in lidars. For instance, one of the spurious effects in CW CDLs is the interferometric noise, not addressed in this thesis. Interferometeric noise and its behavior is beyond the scope of this thesis and has been well-researched in fiber-optics (e.g., see [38, 39]). I believe by employing a signal processing technique known as digital compensation in analog front-ends (also known as dirty RF [33, 40]), it is possible to estimate and reduce the effect of the interferometric noise particularly observed in CW variants of CDLs.

References

[1] S. Svanberg, *Atomic and Molecular Spectroscopy.* Springer, 2001.

[2] E. O. Hulburt, "Observations of a searchlight beam to an altitude of 28 kilometers," *Appl. Opt.*, vol. 27, pp. 377–382, 1937.

[3] G. G. Goyer and R. Watson, "The Laser and Its Application to Meteorology," *B. Am. Meteorol. Soc.*, vol. 44, pp. 564–570, 1963.

[4] F. J. McClung and R. W. Hellwarth, "Giant Optical Pulsations from Ruby," *Appl. Opt.*, vol. 33, pp. 828–829, 1962.

[5] G. Fiocco and L. D. Smullin, "Detection of scattering layers in the upper atmosphere (60-140 km) by optical radar," *Nature*, vol. 199, pp. 1275–1276, 1963.

[6] C. S. Gardner, "Sodium resonance fluorescence lidar applications in atmospheric science and astronomy," *Proc. IEEE*, vol. 77, pp. 408–418, 1989.

[7] T. Fujii and T. Fukuchi, *Laser Remote Sensing.* CRC Press, Chapter 5, 2005.

[8] M.-L. Chanin and A. Hauchecorne, "Lidar observation of gravity and tidal waves in the stratosphere and mesosphere," *J. Geophys. Res.*, vol. 86, pp. 9715–9721, 1981.

[9] M. Gaft and L. Nagli, "UV gated Raman spectroscopy for standoff detection of explosives," *Opt. Mater.*, vol. 30, pp. 1739–1746, 2008.

[10] V. Srivastava, J. Rothermel, A. D. Clarke, J. D. Spinhirne, R. T. Menzies, D. R. Cutten, M. A. Jarzembski, D. A. Bowdle, and E. W. McCaul, "Wavelength dependence of backscatter by use of aerosol microphysics and lidar data sets: application to 2.1-μm wavelength for space-based and airborne lidars," *Appl. Opt.*, vol. 40, pp. 4759–4769, 2001.

[11] C. Mercer, *Optical Metrology for Fluids, Combustion and Solids.* Springer Science+Business Media New York, 108–109, 2003.

[12] Y. F. Arshinov, S. M. Bobrovnikov, V. E. Zuev, and V. M. Mitev, "Atmospheric temperature measurements using a pure rotational raman lidar," *Appl. Opt.*, vol. 22, pp. 2984–2990, 1983.

[13] S. R. Langhoff, C. W. B. Jr., and D. P. Chong, "Theoretical study of the effects of vibrational and rotational interactions on the Raman spectrum of N_2," *J. Chem. Phys.*, vol. 78, p. 5287, 1983.

[14] S. Speziale, H. Marquardt, and T. S. Duffy, "Brillouin scattering and its application in geosciences," *Mineralogy & Geochemistry*, vol. 78, pp. 543–603, 2014.

[15] B. J. Rye, "Molecular backscatter heterodyne lidar: a computational evaluation," *Appl. Opt.*, vol. 37, no. 27, pp. 6321–6328, 1998.

[16] M. O. Vieitez, E. J. van Duijn, W. Ubachs, B. Witschas, A. Meijer, A. S. de Wijn, N. J. Dam, and W. van de Water, "Coherent and spontaneous Rayleigh-Brillouin scattering in atomic and molecular gases and gas mixtures," *Phys. Rev. A.*, vol. 82, p. 043836, 2010.

[17] C. D. Boley, R. C. Desai, and G. Tenti, "Kinetic models and Brillouin scattering in a Molecular Gas," *Canadian Journal of Physics*, vol. 50, no. 18, pp. 2158–2173, 1972.

[18] *U.S. Standard Atmosphere.* U.S. Government Printing Office, 1976.

[19] T. Fujii and T. Fukuchi, *Laser Remote Sensing.* CRC Press, 486–488, 2005.

[20] S. F. Clifford and L. Lading, "Monostatic diffraction-limited lidars: the impact of optical refractive turbulence," *Appl. Opt.*, vol. 22, pp. 1696–1701, 1983.

[21] R. T. Menzies and R. M. Hardesty, "Coherent Doppler Lidar for Measurements of Wind Fields," *Proc. IEEE*, vol. 77, pp. 449–462, 1989.

[22] R. M. Huffaker and R. M. Hardesty, "Remote sensing of atmospheric wind velocities using solid-state and CO_2 coherent laser systems," *Proc. IEEE*, vol. 84, pp. 181–204, 1996.

[23] T. S. Kubo and T. J. Kane, "Diode-Pumped Lasers at Five Eye-Safe Wavelengths," *IEEE J. Quantum Electron.*, vol. 28, pp. 1033–1040, 1992.

[24] D. Taverner, D. J. Richardson, L. Dong, J. E. Caplen, K. Williams, and R. V. Penty, "158-μJ pulses from a single-transverse-mode, large-mode-area erbium-doped fiber amplifier," *Optics Letters*, vol. 22, pp. 378–380, 1997.

[25] ZephIR 300 technical specifications. [Online]. Available: http://www.zephirlidar.com/resources/technical-specs. [Accessed Feb. 6, 2015].

[26] WINDCUBE V2, a 200m vertical wind Doppler lidar. [Online]. Available: http://www.leosphere.com/products/vertical-profiling/windcube-v2. [Accessed Feb. 6, 2015].

[27] Wind Iris, a turbine-mounted lidar. [Online]. Available: http://http://www.aventlidartechnology.com/. [Accessed April 3, 2015].

[28] S. M. Spuler, D. Richter, M. P. Spowart, and K. Rieken, "Optical fiber-based laser remote sensor for airborne measurement of wind velocity and turbulence," *Appl. Opt.*, vol. 50, pp. 842–851, 2011.

[29] C. M. Sonnenschein and F. A. Horrigan, "Signal-to-noise relationships for coaxial systems that heterodyne backscatter from the atmosphere," *Appl. Opt.*, vol. 10, pp. 1600–1604, 1971.

[30] C. J. Karlsson, F. Olsson, D. Letalick, and M. Harris, "All-fiber multifunction continuous-wave coherent laser radar at 1.55 m for range, speed, vibration, and wind measurements," *Appl. Opt.*, vol. 39, pp. 3716–3726, 2000.

[31] R. Targ, M. J. Kavaya, R. M. Huffaker, and R. L. Bowles, "Coherent lidar airborne windshear sensor: performance evaluation," *Appl. Opt.*, vol. 30, pp. 2013–2026, 1991.

[32] R. Schwiesow and R. Cupp, "Offset local oscillator for cw laser Doppler anemometry," *Appl. opt.*, vol. 20, pp. 579–582, 1981.

[33] F. Horlin and A. Bourdoux, *Digital compensation for Analog Front-Ends.* John Wiley & Sons, 2008.

[34] S. L. Chuang and S. L. Chuang, *Physics of Optoelectronic Devices.* John Wiley & Sons, Chapter 12, 1995.

[35] J. Liu, H. Shi, K. Liu, Y. Hou, and P. Wang, "210 W single-frequency, single-polarization, thulium-doped all-fiber MOPA," *Optics Letters*, vol. 22, pp. 13 572–13 578, 2014.

[36] A. T. Pedersen, "Frequency swept fibre laser for wind speed measurements," PhD dissertation, Dept. of Photon. Eng., Tech. Univ. of Denmark, Lyngby, Denmark, 2011.

[37] P. Lindelöw, "Fiber based coherent lidars for remote wind sensing," PhD dissertation, Dept. of Photon. Eng., Tech. Univ. of Denmark, Lyngby, Denmark, 2007.

[38] B. Moslehi, "Analysis of optical phase noise in fiber-optic systems employing a laser source with arbitrary coherence time," *J. Lightw. Technol.*, vol. 4, pp. 1334–1351, 1986.

[39] M. Harris, G. N. Pearson, J. M. Vaughan, D. Letalick, and C. Karlsson, "The role of laser coherence length in continuous-wave coherent laser radar," *J. Mod. Opt.*, vol. 45, pp. 1567–1581, 2009.

[40] G. Fettweis, M. Lohning, D. Petrovic, M. Windisch, P. Zillmann, and W. Rave, "Dirty RF: a new paradigm," in Proc. of IEEE PIMRC: IEEE 16th Int. Symp. on (IEEE, 2005), pp. 2347–2355.

An all-fiber image-reject homodyne coherent Doppler wind lidar

Paper I

Cyrus F. Abari, Anders T. Pedersen, and Jakob Mann

Based on: C. F. Abari, A. T. Pedersen, and J. Mann, "An all-fiber imagereject homodyne coherent Doppler wind lidar," Opt. Express, vol. 22, pp. 25880 – 25894, 2014.

Abstract

In this paper, we present an alternative approach to the down-conversion (translation) of the received optical signals collected by the antenna of an all-fiber coherent Doppler lidar (CDL). The proposed method, widely known as image-reject, quadrature detection, or in-phase/quadrature-phase detection, utilizes the advances in fiber optic communications such that the received signal can be optically down-converted into baseband where not only the radial velocity but also the direction of the movement can be inferred. In addition, we show that by performing a cross-spectral analysis, enabled by the presence of two independent signal observations with uncorrelated noise, various noise sources can be suppressed and a more simplified velocity estimation algorithm can be employed in the spectral domain. Other benefits of this architecture include, but are not limited to, a more reliable measurement of radial velocities close to zero and an improved bandwidth. The claims are verified through laboratory implementation of a continuous wave CDL, where measurements both on a hard and diffuse target have been performed and analyzed.

1 Introduction

Light detection and ranging (lidar) instruments have been in use for remote sensing of atmospheric conditions, including the atmospheric boundary layer (ABL), for about five decades. For instance, Fiocco and Smullin [1] demonstrated one of the early application of lidars (also known as optical radar) in atmospheric characterizations and meteorological observations. Wind lidars were already employed in early 1970s [2]. Following advances in fiber optic communications, where lasers with wavelengths close to 1550 nm are used, this technology has been extensively used in all-fiber CDLs. Commercial examples of such systems are widely available: for instance, ZephIR from ZephIR Lidar [3], Windcube from Leosphere [4], and WindEye from WINDAR Photonics [5] are examples of all-fiber CDLs. The all-fiber 1550 nm CDLs have a master oscillator power amplifier architecture (MOPA) where a compact laser source, known as the master oscillator (MO), is utilized for the generation of a highly coherent light. Examples of MOs are distributed feedback (DFB) fiber or semiconductor lasers. DFB lasers have a small form factor and provide high sensitivity, robustness, and low levels of phase noise. The fiber optic technology, used in optical communications industry, is employed for the generation, amplification, transmission, and manipulation of the laser beam in all-fiber CDLs. Applications of CDLs in the wind industry cover, but are not limited to, the measurement of wind velocities in terrain for the characterization and optimization of wind turbine installation (wind resource assessment) [6, 7], the measurement of the incoming wind flow for optimal wind turbine yaw and pitch control [8, 9], and power curve verification [10].

Typically, there are two major variants of mono-static CDLs used for wind measurements, i.e., continuous wave (CW) and pulsed. In CW CDLs ranging is achieved by translating the end facet of the delivery fiber along the optical axis of the telescope [11]. Thus, ranging is achieved by focusing the laser beam on the range of interest. On the other hand, pulsed lidars emit a laser pulse for wind flow characterizations [12]. In such systems, ranging is achieved by range gating the received signals, i.e., the collected scattering from aerosol particles [13]. In both types of systems, the backscatter from aerosol

particles are collected through a telescope which passes them on to the following stages for further processing.

Due to numerous advantages provided by digital signal processing algorithms, the detected signals are typically digitized for further treatment. However, the available analog-to-digital converters (A/D) have limited bandwidth (BW) that is far below the laser frequency, conventionally known as the carrier frequency. Besides, the opto-electronic components, such as photodetectors have limited BW and cannot follow signal fluctuations in the THz region. As a result, it is imperative to down-convert the optical signals into lower radio frequency (RF) spectrum known as intermediate frequency (IF) or baseband, also known as zero-IF. Coherent receivers achieve this by mixing (beating) the reflections with a local oscillator (LO) signal, usually derived from the MO. Depending on the LO frequency and the front-end treatment of the signals, various architectures may be realized. In fact, the optical coherent detection is "simply an extension into the optical region, of a well-known radio-frequency technique used in superheterodyne receiver". [14]

Depending on the frequency where the optical signal is translated [15] the architectures in CDLs may be categorized into two main classes: direct-conversion (homodyne) and heterodyne architectures. In homodyne receivers, the LO and signal carrier frequencies are equal. In heterodyne receivers, the carrier frequency is different from the LO's. A homodyne or heterodyne receiver may be realized through either real mixing or in-phase/quadrature-phase (I/Q) mixing, also known as complex mixing. The complex mixing process is also known as the image-reject or quadrature mixing principle. The inability to perform an image rejection (and thus real mixing) in telecommunications results in possible corruption of the transmitted information because the two sides of the band overlap and interfere [16]. In CDLs it results in a symmetric spectrum where the sign of the radial wind velocity cannot be discriminated which is a rather serious issue for certain applications. To solve the sign ambiguity, a few receiver architectures can be employed, the most popular of which are heterodyne receivers with IF sampling and homodyne receivers with complex mixing. Heterodyne mixing with IF sampling is a well-known and widely used approach for signal detection in CDLs.

In this paper, we show that by employing a direct image-reject architecture in a CW CDL, made feasible through commercially available components for optical communications, a more robust and accurate CDL can be prototyped. The result is a system that has twice the BW as existing CDLs that employ heterodyning with IF sampling for a similar system configuration. In addition, the prototype system provides a better estimate of radial velocities close to zero where the signal is contaminated by noise in heterodyne receivers. Furthermore, it is shown that by performing a cross-spectral analysis between the in-phase and quadrature-phase components, the noise sources (mainly the shot noise) can be suppressed and a less signal processing intensive algorithm employed to extract the radial velocity information. Although the focus of the paper is on CW CDLs many of the principles can be applied to a pulsed CDL with no or minor modifications.

The paper is divided into several sections. In Section 2, we adopt a simple but efficient signal model associated with coherent detection in an all-fiber homodyne CW CDL with real mixing to present the concepts and lay a mathematical framework. In Section 3, we present the image-reject homodyne receiver and analyze its theoretical performance with respect to receivers with real mixing such as the one described in Section 2. A

laboratory prototype of an all-fiber image-reject homodyne CW CDL, as described in this paper, is presented in Section 4 where a few measurement results on hard and diffused target are presented as a proof of concept. Throughout the paper, an effort has been made to emphasize the most important parameters affecting the CDL performance for the discussed architectures. Meanwhile, wherever deemed appropriate, we have ignored the topics secondary to the results presented in this paper. We have also adopted a number of simplifications without sacrificing the generality and applicability of the results. The optical and electronic components in this paper are assumed to be lossless and ideal unless otherwise specified in the text.

2 Coherent detection and signal modeling

Before analyzing the image-reject receiver architectures, it is worthwhile to adopt appropriate transmit and receive signal models associated with a CW CDL in a MOPA configuration. Fig. 1 illustrates one of the simplest receiver architectures adopted for such systems. In this system, the laser source signal, MO, is modeled after the fundamental mode of an optical resonator, i.e., TEM_{00} [15], where the transverse irradiance has a Gaussian distribution and the longitudinal intensity is Lorentzian. Irrespective of the temporal irradiance shape associated with the transmitted laser signal, we can adopt the following mathematical model in time domain for the electric field fluctuations of the optical signal at the output of the erbium doped fiber amplifier (EDFA):

$$L(t) = \sqrt{2p}\cos\left[2\pi f_c t + \theta(t)\right] + L_R(t), \tag{2.1}$$

where p is the optical signal power, f_c is the laser frequency (also known as the carrier frequency), $\theta(t)$ is the laser phase noise that defines the laser line width [17], and $L_R(t)$ is the relative intensity noise (RIN) of the laser. After passing through the optical circulator, $L(t)$ is split into a transmit signal $s(t)$ and LO signal $L_O(t)$. LO in this particular system configuration is derived by collecting the back reflections from the end facet of the delivery fiber, i.e., the fiber at the input of the telescope. The LO power can be adjusted by polishing the end facet of the delivery fiber [11] at the desired angle. Thus, the transmitted signal, $s(t)$, through the telescope is a major fraction of $L(t)$ where $s(t) = \sqrt{1-\epsilon}L(t)$. Furthermore, $0 < \epsilon < 1$ is the splitting ratio that controls the LO power. For reflections from a diffuse target such as backscatter from aerosol particles in the air the received signal for the collected light by the telescope can be modeled as

$$r(t) = \left[2(1-\epsilon)p\right]^{1/2} \sum_{l=0}^{L-1} \alpha_l \cos\left[2\pi\left(f_c + \Delta f_l\right)t + \theta(t) + \phi_l\right], \tag{2.2}$$

where α_l is the net optical attenuation , Δf_l is the Doppler shift due to motion, ϕ_l is the phase factor associated with the lth aerosol particle, and L is the number of aerosol particles in the measurement volume. Furthermore, α_l, Δf_l, and ϕ_l can be modeled as independent random variables where Δf_l has a Gaussian distribution and ϕ_l is a uniformly distributed random variable with $\phi_l \in [0, 2\pi)$. In Eq. (2.2) the effect of $L_R(t)$ in the collected signal has been ignored because its power is insignificant compared to the power of the transmitted signal.

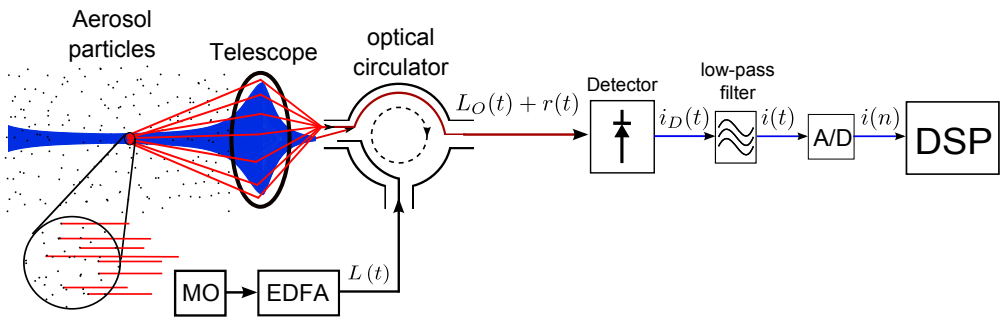

Figure 1: Homodyne receiver with real mixing. The LO is derived from the Fresnel reflections at the end facet of delivery fiber at the output of the circulator.

Moreover, the average received power in Eq. (2.2) is approximated by [18]

$$p_r = \pi p_t \beta(\pi) \lambda, \tag{2.3}$$

where $p_t = (1-\epsilon)p$ is the transmit signal power, $\beta(\pi)$ is the atmospheric backscatter coefficient, and λ is the wavelength.

The phase noise, $\theta(t)$, is commonly characterized by a Wiener process [19]. It can be shown that phase noise exhibits a Lorentzian shaped spectrum whose 3-dB BW defines the laser line-width, characterizing the coherence length of the laser. Phase noise in modern DFB lasers can be improved such that its detrimental effect in coherent lidars can be ignored for the majority of practical applications. Thus, for simplicity and without loss of generality, we ignore the effect of phase noise for the remainder of this paper.

On the other hand, RIN can be of practical importance, especially for DFB fiber lasers. Although, most of RIN will be buried under a detector's shot noise, the RIN peak, associated with the laser's relaxation frequency [20], may skew the measurements. This is more pronounced for gas lasers such as He-Ne [21] and fiber lasers [22] where the peak appears in the low-frequency region of the spectrum. Therefore, the presence of RIN affects the measurement results and the minimum detectable signals [23] and is a limiting factor, especially in optical remote sensing and meteorology [24]. It has been shown [25] that the RIN peak for some semiconductor lasers is outside the measurement range of interest and does not pose a problem when compared to fiber based lasers.

To illustrate the concepts in this paper, we have derived the mathematical models associated with backscatter from a single particle. The models provide a simple mathematical way to present the concepts that hold for both hard targets and diffuse targets. Verification of the results has been provided through atmospheric measurements presented in Section 4.

Following Eq. (2.2), the received signal associated with backscatter from a single particle can be modeled as

$$r(t) = \alpha \left[2(1-\epsilon)p\right]^{1/2} \cos\left[2\pi\left(f_c + \Delta f\right)t + \phi\right], \tag{2.4}$$

where subscript l has been dropped for a single particle.

If LO is

$$L_O(t) = \sqrt{2\epsilon p} \cos\left(2\pi f_c t\right), \tag{2.5}$$

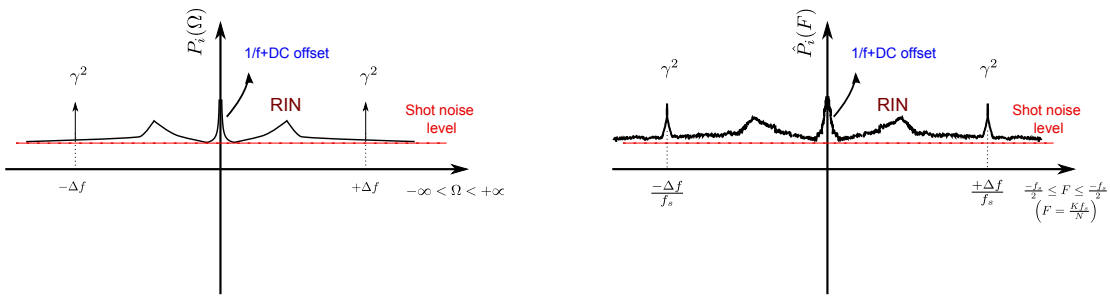

(a) CTFT (b) DFT

Figure 2: Examples of the PSD associated with the baseband signal. (a) The spectra when CTFT has been performed to estimate the spectra. (b) The effect of estimation noise when a limited observation time is available for spectral processing after digitization.

then mixture of the received and LO signals, i.e., $r(t) + L_o(t)$, is impinged on a photo detector whose response to the light intensity, in the form of an electric current, can be modeled as

$$i(t) \propto \left[r(t) + L_o(t)\right]^2. \tag{2.6}$$

After some mathematical manipulation and simplifications, the resultant current at the output of the low-pass filter is

$$i(t) = 2\gamma \cos\left[2\pi\left(\Delta f\right)t + \phi\right] + \eta(t), \tag{2.7}$$

where $\gamma = p\alpha R_D\left[\epsilon(1-\epsilon)\right]^{1/2}$ and $\eta(t)$ is the total noise. Furthermore, R_D is the detector responsivity and

$$\eta(t) = \eta_{\text{dc}} + \eta_R(t) + \eta_{sn}(t) + \eta_f(t), \tag{2.8}$$

where η_{dc} is the DC noise, $\eta_R(t)$ is the detected RIN, $\eta_{\text{sn}}(t)$ is the shot noise, and $\eta_f(t)$ is the $1/f$ noise. In Eq. (2.8) we have ignored the effect of thermal noise and the detector's dark noise as they are insignificant when compared to other noise sources. Furthermore, the shot noise power is

$$p_{\eta_{sn}} = 2ER_D p_{LO} B, \tag{2.9}$$

where $E = 1.3 \times 10^{-19}$ J is the light quantum energy, p_{LO} is the local oscillator power, and B is the BW.

The baseband signal in Eq. (2.7) contains the Doppler shift information which can be extracted through spectral analysis of the signal. Thus, for the received signal in Eq. (2.7)

$$P_i(\Omega) = \mathscr{F}\left\{\mathbb{E}\left[i(t)\overline{i(t+\tau)}\right]\right\} = \gamma^2\delta(\Omega - \Delta\Omega) + \gamma^2\delta(\Omega + \Delta\Omega) + P_\eta(\Omega), \tag{2.10}$$

where $P_i(\Omega)$ and $P_\eta(\Omega)$ are the power spectral density (PSD) of the signal and noise respectively, $\mathscr{F}$ is the continuous-time Fourier transform (CTFT), Ω is the frequency in Laplace domain, $\mathbb{E}[\cdot]$ denotes the ensemble average operation, and $\overline{(\cdot)}$ represents the complex conjugate operation. Fig. 2(a) illustrates an example of the PSD associated with Eq. (2.10). As can be seen, the PSD is symmetric around zero frequency.

In practice, due to the advances in digital signal processors and computers, the signals need to be digitized for further processing. However, only a limited observation time is available for processing (e.g., spectral processing) of the digitized signal. There are various ways [26, 27] to estimate the PSD of a signal such as the one in Eq. (2.7). A widely used method is to estimate the spectra through periodograms [28], which when applied to the digitized version of the signal in Eq. (2.7), results in

$$\hat{P}_i(K) = \frac{f_s}{M} \sum_{m=0}^{M-1} |I(K)|^2 , \tag{2.11}$$

where K is the discrete frequency component, M is the number of averages, and f_s is the sampling frequency. In addition, $I(K)$ is the discrete Fourier transform (DFT) defined as

$$I(K) = \frac{1}{N} \sum_{n=0}^{N-1} i(n) \exp\left(-2\pi j \frac{n}{N} K\right) , \tag{2.12}$$

where N is the number of DFT points. Compared to Eq. (2.10),

$$\hat{P}_i(K) = P_i\left(\Omega_K\right) + \eta_{est}(K), \tag{2.13}$$

where $\eta_{est}(K)$ is the estimation noise and $\Omega_K = \frac{K f_s}{N}$. For the shot-noise limited operational mode, where the effect of all other noise sources are neglected, $\eta_{est}(K)$ can be modeled as a Gaussian random variable [29] where

$$\begin{aligned} \mu_{\eta_{est}}(K) &= \mathbb{E}\left\{\eta_{est}(K)\right\} = \eta_{sn}\left(\Omega_K\right), \\ \sigma_{\eta_{est}}(K) &= \frac{P_i\left(\Omega_K\right)}{\sqrt{M}}. \end{aligned} \tag{2.14}$$

Fig. 2(b) shows an example of an estimated PSD for the signal in Eq. (2.7).

The ability to detect the Doppler shift in practice depends on the performance of the estimation algorithm that can discriminate the signal information from the noise, especially, the estimation noise. As a result, it seems necessary to define a new quantity:

$$\mathrm{SENR}_i = \frac{P_i(K_D) - P_\eta(K_D)}{\sigma_{\eta_{est}}(K)|_{(K \neq K_D)}}, \tag{2.15}$$

where SENR_i is the signal-to-estimation-noise-ratio and $K_D = \pm\lfloor \frac{\Delta f}{f_s} \rfloor N$, the frequency associated with the Doppler peak. Please note that SENR is different from (the commonly used)

$$\mathrm{SNR}_i = \frac{\int_{-\infty}^{+\infty} P_i\left(\Omega\right)\, d\Omega - p_\eta}{p_\eta}, \tag{2.16}$$

where $p_\eta = \int_{-\infty}^{+\infty} P_\eta\left(\Omega\right)\, d\Omega$. For a shot-noise limited operation, where the effect of other noise sources and unwanted signals is ignored, and assuming a flat spectra the SNR for the presented homodyne receiver with real mixing is

$$\mathrm{SNR}_i = \frac{\alpha^2 R_D (1-\epsilon) p}{EB}. \tag{2.17}$$

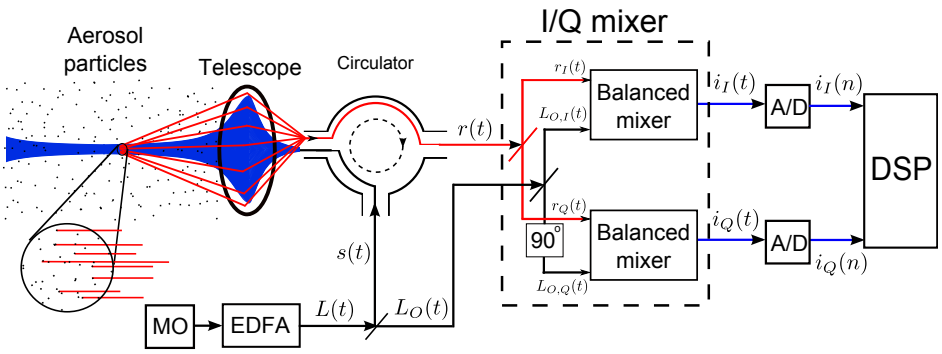

Figure 3: The schematic of the image-reject homodyne receiver.

One of the major sources of unwanted signals is the non-ideal behavior of optical components such as the optical circulator. For instance, due to the presence of phase noise and cross-talk in optical circulators the estimated signal may suffer from interferometric noise [30, 31]. Reflections from optical components such as telescope lenses can also be compounding. A thorough analysis of SENR has been performed in [29] from which it can be inferred that the SENR for the simple homodyne system, described in this section, is

$$\mathrm{SENR}_i = \frac{\sqrt{M}\alpha^2 R_D(1-\epsilon)p}{E} = B\sqrt{M}\mathrm{SNR}_i. \tag{2.18}$$

As shown in Eq. (2.16), SNR refers to the ratio of the signal power and the instrument noise power (e.g., shot-noise). In spectral analysis, however, SENR seems to be the major player in determining how well the signal can be estimated when buried in estimation noise.

Despite its many advantages, the above-modeled system suffers from an inability to discriminate the direction of travel, i.e., the sign of the radial velocity. This is evident from the example PSDs illustrated in Figs. 2(a)-2(b), in which the presence of the image component of the Doppler signal masks the sign of the radial velocity. To extract the direction of travel, other receiver architectures need to be implemented. Examples of such systems are heterodyne receivers with IF sampling [32], super heterodyne receivers [33], and image-reject homodyne receivers. In the following sections we have presented a detailed analysis of an all-fiber image-reject homodyne receiver. The presented system not only resolves the sign ambiguity, but it also benefits from a novel approach in signal processing that eliminates the major noise sources and simplifies extraction of the Doppler information from the signal. Additionally, through prototyping the system we will demonstrate its performance for a number of different measurement scenarios, including measurement on hard and diffuse targets.

3 Image-reject architecture

To resolve the ambiguity associated with the direction of travel, an image-reject homodyne receiver can be utilized. In image-reject homodyne receivers, the return signal is mixed

with two realizations of the LO signal where one realization is exactly 90 degrees out of phase with respect to the other one. This concept is widely used in radio systems [16] and in optical communications [34]. The idea has also been tested as a solution in CDLs using open space optics. For instance, it has been shown [35] that by using a circularly polarized light one can attain the in-phase and quadrature-phase LO realizations required for this principle. The reported results were based on measurements on a hard target in a laboratory environment. However, to the best of our knowledge, this is the first time an all-fiber system implementation of a CDL employing an image-reject homodyne architecture has been reported in literature where measurements for both hard and diffuse targets have been successfully performed.

Fig. 3 provides an illustration of the system implementation for an all-fiber image-reject architecture. In contrast to the homodyne receiver illustrated in Fig. 1, the LO signal in this system is not derived from Fresnel reflection at the end facet of the delivery fiber at the output of the optical circulator. Instead, two realizations of the LO with equal power are obtained through an I/Q mixer. The I/Q mixer has two fundamental roles. First, it provides two realization of the LO required for in-phase and quadrature-phase components. Second, it utilizes two balanced mixers to mix the return signal with the LO, detect the result, and filter the signals for delivery to the next stage for digitization and further processing. The splitters inside the I/Q mixer provide a 50/50 splitting ratio while the 90 degree phase shift is achieved through a finely tuned delay line. Thus,

$$\begin{cases} L_{O,I}(t) = \sqrt{\epsilon p}\cos\left(2\pi f_c t\right), \\ L_{O,Q}(t) = \sqrt{\epsilon p}\sin\left(2\pi f_c t\right). \end{cases} \tag{3.1}$$

Furthermore, it can be shown that, $p_{LO,I_1} = p_{LO,I_2} = p_{LO,Q_1} = p_{LO,Q_2} = \frac{\epsilon p}{4}$, where subindices refer to the individual photo-diodes at the in-phase and quadrature-phase legs.

The balanced mixer, as shown in Fig. 4, is mainly composed of a fiber coupler and two matched photo diodes. The input signals (the return signal and the LO) fed into the coupler, having a 50-50 coupling ratio, are mixed such that the output legs provide a common and differential signal components. At the output of the matched diode pair the common component is rejected and the differential mode is passed through. For such a configuration, the common mode rejection ratio (CMRR) depends on the matching of the two photo-diodes as well as the coupling ratio. In this paper, we have assumed ideal matching between the two diodes as well as an ideal and stable 50% coupling ratio.

After some mathematical manipulations and simplifications, it can be shown that the current at the output of the balanced mixer for the in-phase and quadrature-phase components are

$$\begin{cases} i_I(t) = \sqrt{2}\gamma\cos\left[2\pi\left(\Delta f\right)t + \phi\right] + \eta_I(t), \\ i_Q(t) = \sqrt{2}\gamma\sin\left[2\pi\left(\Delta f\right)t + \phi\right] + \eta_Q(t), \end{cases} \tag{3.2}$$

where subscripts $(\cdot)_I$ and $(\cdot)_Q$ denote the in-phase and quadrature-phase components, respectively. Additionally,

$$\begin{cases} \eta_I(t) = \eta_{sn,I}(t) + \eta_{f,I}(t), \\ \eta_Q(t) = \eta_{sn,Q}(t) + \eta_{f,Q}(t). \end{cases} \tag{3.3}$$

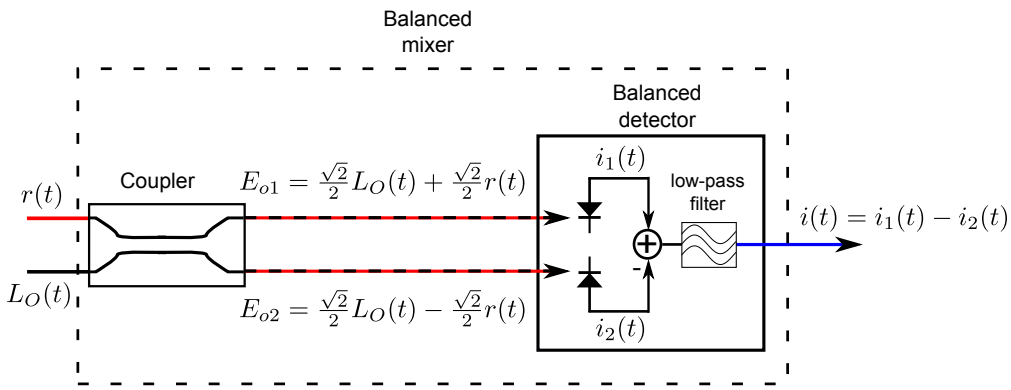

Figure 4: The schematic of the balanced mixer. The mixer consists of a balanced coupler and two balanced photo diodes connected in reverse.

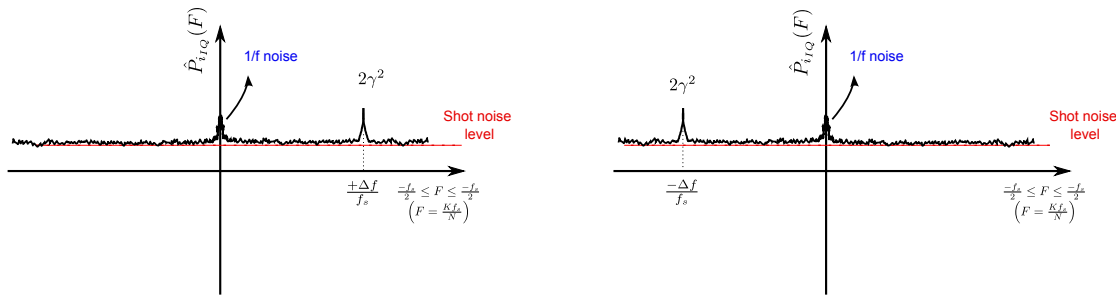

(a) Autospectrum, positive Doppler shift (b) Autospectrum, negative Doppler shift

Figure 5: Examples of the estimated PSD associated with the baseband signal. (a) The spectra when the radial direction of travel associated with the target is positive. (b) Because the radial direction of travel is away from the telescope, a negative Doppler shift is measured.

In Eq. (3.3), we have ignored the effect of RIN and DC noise since they appear at the common mode of the ideally modeled balanced mixers and are filtered out. In practice, due to reflections from optical surfaces in the system, there is a DC term that appears in the differential mode. We have assumed ideal optical surfaces so that reflections can be ignored.

The signal pair in Eq. (3.2) can be combined to make a complex valued signal such that,

$$i_{IQ}(t) = \sqrt{2}\gamma\cos\left(2\pi\Delta f t + \phi\right) + \eta_I(t) + j\left[\sqrt{2}\gamma\sin\left(2\pi\Delta f t + \phi\right) + \eta_Q(t)\right], \tag{3.4}$$

where $j = \sqrt{-1}$. Moreover, it can be shown that

$$\begin{cases} P_{i_{IQ}}(\Omega) = 2\gamma^2\delta(\Omega - \Delta\Omega) + P_{\eta_I}(\Omega) + P_{\eta_Q}(\Omega), \\ \hat{P}_{i_{IQ}}(K) = P_{i_{IQ}}(\Omega_K) + \eta_{est}(K), \end{cases} \tag{3.5}$$

and [29]

$$\mathrm{SENR}_{i_{IQ}} = \sqrt{M}\mathrm{SNR}_{i_{IQ}} = \frac{\sqrt{M}\alpha^2 R_D(1-\epsilon)p}{E}. \tag{3.6}$$

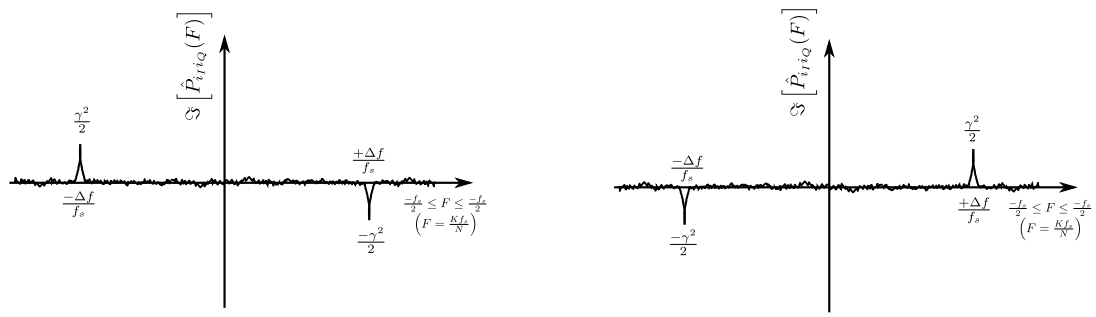

(a) Cross-spectrum, positive Doppler shift (b) Cross-spectrum, negative Doppler shift

Figure 6: Examples of the estimated cross-spectra of the in-phase and quadrature-phase signal components in baseband. (a) Positive Doppler shift. (b) Negative Doppler shift.

Fig. 5(a)-5(b) show examples of the PSD associated with Eq. (3.5). As can be seen, the PSDs are not symmetric. Also, when compared to the PSDs in Fig. 2(a)-2(b), they are free from RIN and DC noise, thanks to the balanced mixer.

Although the shot noise exhibits a flat spectrum, it is usually shaped due to the presence of filters and electronic components. As a result, to extract the Doppler information it is necessary to whiten the noise [36]. Among other things, noise whitening is a signal processing intensive algorithm and adds to the uncertainty of radial velocity estimation. The image-reject architecture makes the noise whitening redundant due to the availability of two signal observations with independent noise sources. As a result, by performing a cross-spectral analysis between the in-phase and quadrature-phase components we have shown that the signal information, including the direction of travel, is contained in the imaginary part of the result. Thus,

$$\mathrm{Im}\left[P_{i_\mathrm{I} i_\mathrm{Q}}(\Omega)\right] = \frac{1}{2}\gamma^2\left[\delta(\Omega+\Delta\Omega) - \delta(\Omega-\Delta\Omega)\right], \tag{3.7}$$

where

$$P_{i_\mathrm{I} i_\mathrm{Q}}(\Omega) = \mathscr{F}\left(\mathbb{E}\left[I_I(\Omega)\overline{I_Q(\Omega)}\right]\right), \tag{3.8}$$

and $\mathrm{Im}\left[\cdot\right]$ represents the imaginary component. Furthermore,

$$\hat{P}_{i_\mathrm{I} i_\mathrm{Q}}(K) = \frac{f_s}{M}\sum_{m=0}^{M-1} I_I(K)\overline{I_Q(K)} = P_{i_\mathrm{I} i_\mathrm{Q}}(\Omega_K) + \eta_{\mathrm{est,IQ}}(K), \tag{3.9}$$

where, similar to Eq. (2.14), $\eta_{\mathrm{est,IQ}}$ is a zero-mean Gaussian random variable with $\sigma^2_{\eta_{\mathrm{est,IQ}}}$. Moreover, following [29] it can be shown that

$$\mathrm{SENR}_{i_I i_Q} = \frac{\sqrt{2M}\alpha^2 R_D(1-\epsilon)p}{2E}. \tag{3.10}$$

One of the main advantages of the cross-spectral analysis is elimination of uncorrelated noise sources including the shot-noise. Elimination of background noise simplifies the estimation algorithms (including background noise whitening) to extract the Doppler information. It also reduces the number of frequency bins by a factor of 2, which essentially

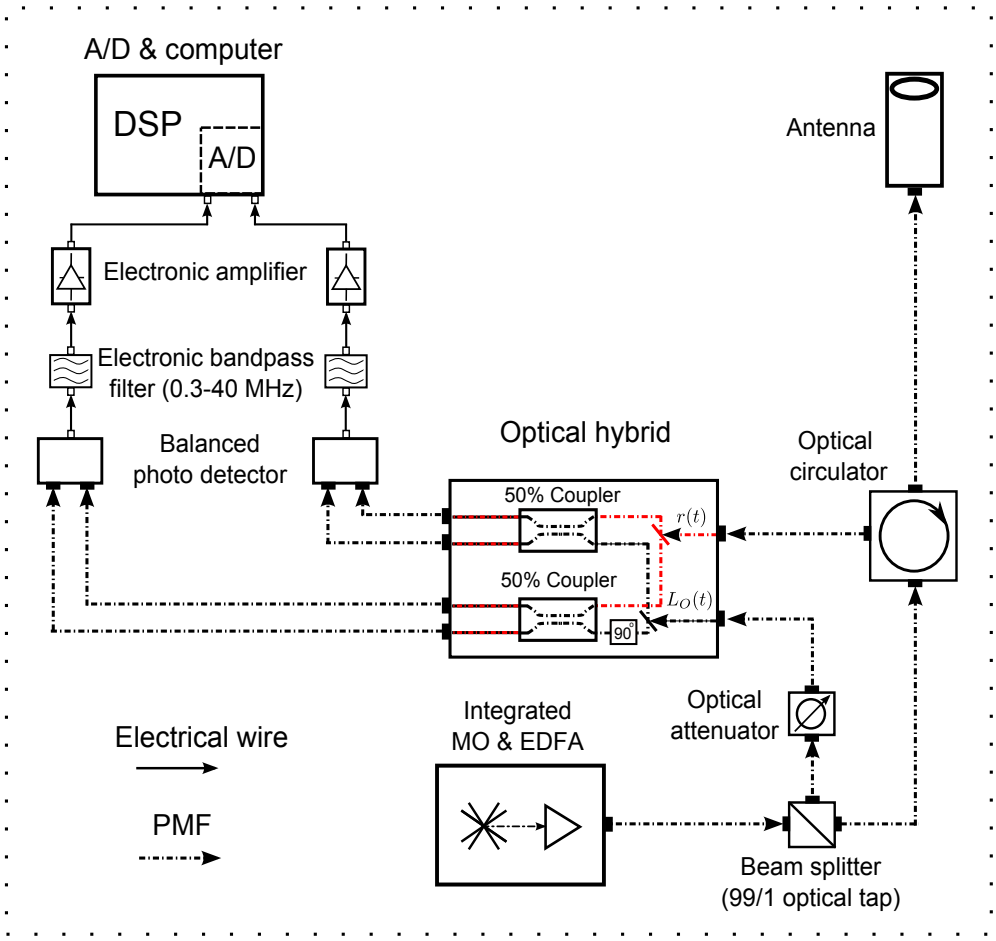

Figure 7: The schematic of the system set-up. All optical fibers are Panda polarization maintaining fibers. Also, all the optical components in this system are polarization maintaining and fiber coupled. Except the optical antenna (telescope), all the components are commercially available.

translates into a more efficient storage of spectral data. Moreover, due to the elimination of 1/f noise and DC noise around zero-frequency component, a better estimate of the radial velocities close to zero can be performed. The experimental results, carried out for the measurement of the vertical component of the wind, support the above mentioned claim and will be published in a future paper. This is in contrast to other available system implementations, such as the heterodyne receiver with IF sampling employing an AOM, where the system suffers from added noise by the additional active component (that is, the AOM) and non-ideal filters such as notch filters. Despite its many advantages, the cross-spectral approach suffers from an inherent SENR loss, viz., $\frac{\sqrt{2}}{2}$, [29] that becomes evident when comparing Eq. (3.6) and Eq. (3.10).

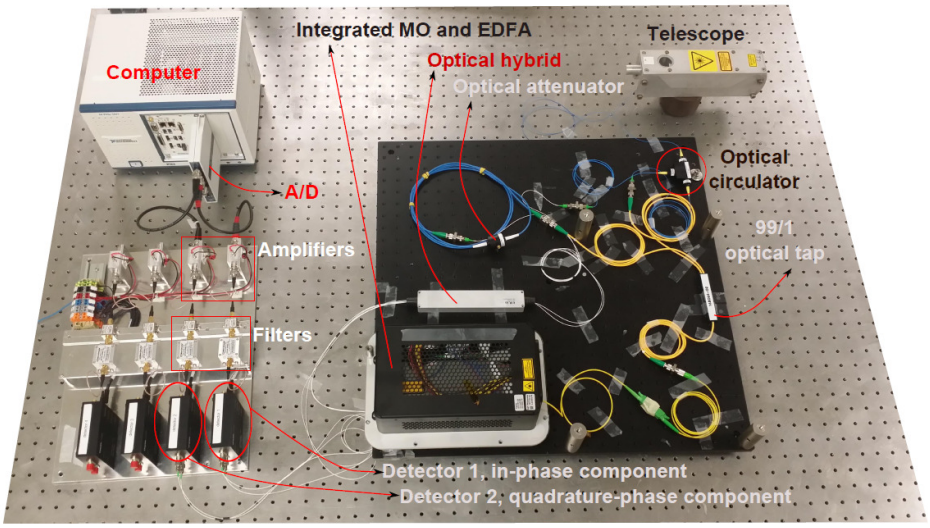

Figure 8: The system set-up in the laboratory environment.

4 Experimental results

An all-fiber prototype of the proposed architecture in this paper has been built and tested on hard and diffuse targets (atmospheric aerosols). The measurement results for hard and diffused targets, as presented in this section, are solely meant for proof of concept. A detailed analysis of the measurements and how they compare to measurements done by a reference instrument (such as a sonic anemometer) is well beyond the scope of this paper and will be provided in a future paper.

The system follows the schematic illustrated in Fig. 7. An integrated MO and EDFA configuration generates a fiber coupled Gaussian beam at the wavelength of 1565 nm. The maximum output power is around 1.35 W. The output is split by an optical tap into two signals: LO and transmit signals. The splitting ratio is 99/1; that is, 99% of the laser power is directed towards the telescope (via the optical circulator) while 1% of the power is fed into an optical attenuator for fine-tuning of the LO power. For optimal coherent detection the LO power should be large enough so that the photo detectors are in shot-noise limited operation mode. However, it is imperative to make sure the detectors are not operating in saturation mode. The return signal from the target is collected by the telescope and fed into the optical circulator. Eventually, the signal is passed by the optical circulator to the optical hybrid. The optical hybrid collects the return signal as well as the LO and produces the necessary in-phase and quadrature components in balanced pairs at the output. The results are fed into the balanced photo detectors. After detection, the electrical signal from the the balanced photo detectors are filtered and amplified before being converted into digital signals. The result is processed by the computer where the Doppler information can be extracted. We used an integrated A/D card and National Instrument (NI) computer. Fig. 8 shows a photo of the system set-up in the lab environment.

For measurements on a hard target, a rotating disk was used as the primary target in the lab. Due to strong reflective behavior of the disk the transmit signal power of

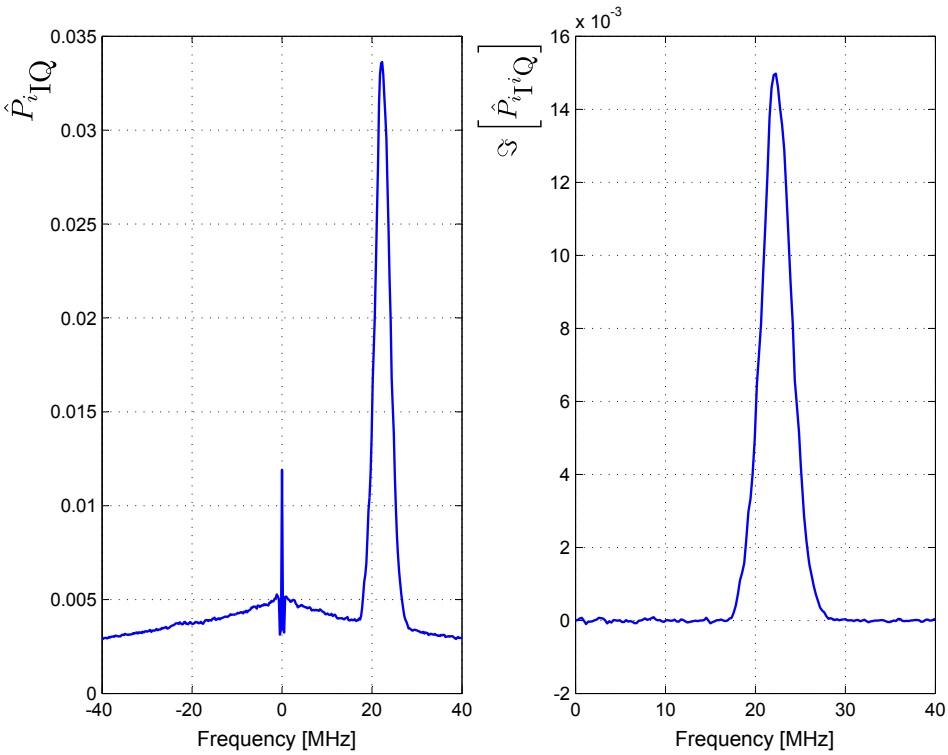

Figure 9: The measurement on a moving hard target, i.e., a spinning disk. The leftmost plot illustrates the autospectrum of the complex signal, while the rightmost one refers to the one-sided cross-spectra between the in-phase and quadrature-phase signal components. Please note that single-sided cross-spectrum (the right-most plot) represents the left side of the spectrum in Figs. 6(a)-6(b), as it contains all the relevant information for the measurement of radial velocity as well as direction.

the laser was adjusted to 70 mW. The target was 5 meters away from the telescope. The laser beam was focused at the distance of 2 meters from the telescope output lens. Table 1 lists the system parameters for the measurement campaigns. As Fig. 9 shows, a wide-band Doppler frequency shift is measured. The wide-band characteristic is due to the transmit signal spot size on the surface of the rotating disk; the rotational speed of the disk varies as a function of the distance from the center of the disk. The narrow dip around zero frequency is due to the high-pass filter. It is evident that despite the presence of the high-pass filter a strong DC component still exists. Furthermore, it can be seen that the autospectrum, the leftmost plot in Fig. 9, exhibits a colored (filtered) Gaussian noise as expected across its frequency span. The filtering effect might become significant due to environmental dependency of the electronic components. As a result, for the autospectrum shown in the left-most plot in Fig. 9, noise whitening needs to be carried out before an accurate radial speed can be estimated. The rightmost plot in Fig. 9 illustrates the one-sided cross-spectral analysis, as a result of which the uncorrelated noise sources, e.g., shot noise, 1/f noise, and DC noise due to reflections from the telescope, are suppressed. Besides, due to a relatively flat background spectrum, noise whitening is not required in this case. Thus, radial velocity estimation is not only easier but also more accurate than the autospectral analysis for the majority of scenarios.

Table 1: Experimental system parameters

Campaign	p_t [W]	BW [MHz]	f_s [MHz]	N	M	Aperture size [inches]
Hard target	70×10^{-3}	40	120	512	4000	2
Diffuse target	1.1	40	120	512	4000	2

For atmospheric measurements, the full output power of the integrated MO and EDFA was used. Due to losses in the system (e.g., fiber connectors) the maximum output power to the telescope was 1.1 W. Fig. 10 illustrates the atmospheric measurement. For this campaign the telescope was pointing upward. As a result, the vertical component of the wind was measured. We know from experience that measuring the vertical component accurately is a challenge due to the presence of the Doppler signal in the vicinity of the DC component (i.e., zero frequency). As seen in the leftmost plot in Fig. 10, the signal strength is much lower and the Doppler shift is closer to zero. Accurate estimation of radial velocity in this case also requires additional signal processing and filtering. However, by utilizing the cross-spectral analysis, the majority of noise sources are suppressed and a rather flat spectra is achieved. It is evident that the benefits of cross-spectral analysis are more emphasized for weaker Doppler signals and lower radial velocity speeds, where dilution with various noise sources around zero frequency is more severe. As we will show in a future paper, however, the merits of the cross-spectral technique become questionable once the Doppler spectrum crosses the zero frequency, where the signal contains both negative and positive Doppler shifts close to zero.

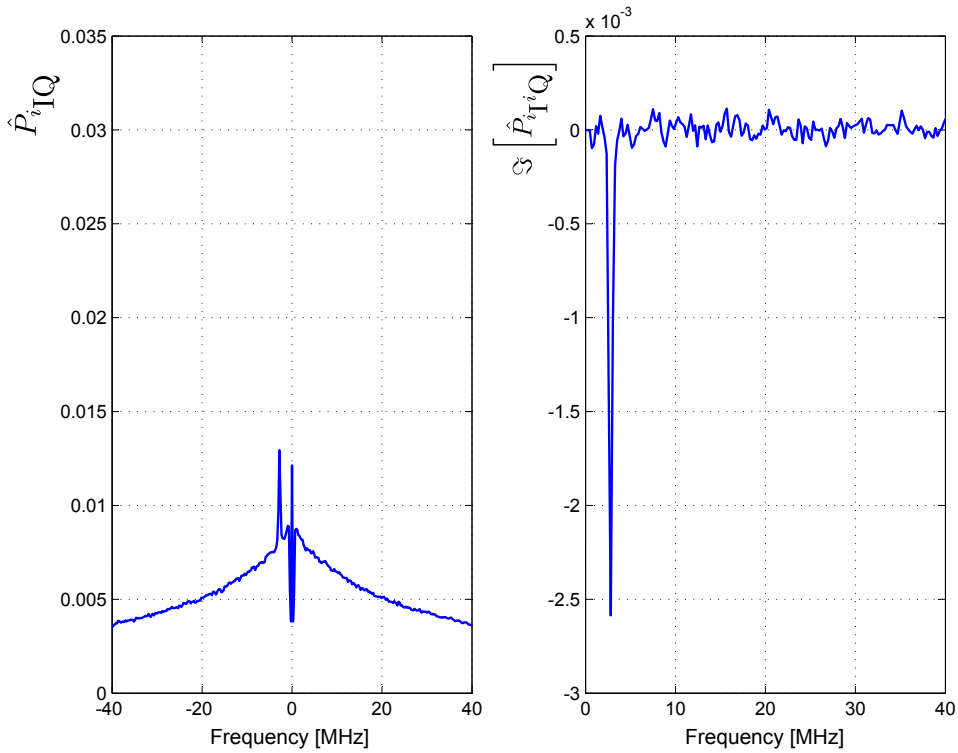

Figure 10: The atmospheric measurement using the full output power of the laser. The measurement spectra is associated with the vertical component of the wind. The leftmost plot illustrates the autospectrum of the complex signal, while the rightmost one refers to the one-sided cross-spectra between the in-phase and quadrature-phase signal components. Please note that single-sided cross-spectrum (the right-most plot) represents the left side of the spectrum in Figs. 6(a)-6(b), as it contains all the relevant information for the measurement of radial velocity as well as direction.

5 Conclusion

By analyzing a promising new approach, an all-fiber image-reject architecture, for signal detection in fiber CDLs, we have shown that a more robust system implementation can be realized. The robustness is partly the result of using passive components, as opposed to alternative system implementations such as heterodyne receivers that use active components, and partly attributable to a new approach in signal processing algorithm made available due to the presence of in-phase and quadrature-phase signal components. Despite its simplicity, the signal processing algorithm, the cross-spectral analysis, improves the accuracy of Doppler shift estimation by eliminating the estimation inaccuracies often introduced by noise whitening procedure, as well as suppressing the major extraneous noise present in the auto-spectral counter-part. Additionally, the presented system profits from a lower memory requirement for the storage of the estimated spectra. The new approach benefits from an all-fiber technology available in fiber optic communications and is easy to implement.

Acknowledgements

The authors would like to thank Torben Mikkelsen, Mikael Sjöholm, Peter John Rodrigo, and Christophe Peucheret from Technical University of Denmark, as well as Mike Harris from ZephIR Lidar (UK), for the fruitful discussions that helped us understand the concepts more clearly. This project is mainly funded by the WindScanner project from the Danish Strategic Research Council, Danish Agency for Science -Technology and Innovation; Research Infrastructure 2009; Grant No. 2136-08-0022. Ingeborg and Leo Dannin Grant for Scientific Research funded the NI computer used in this work.

References

[1] G. Fiocco and L. D. Smullin, "Detection of scattering layers in the upper atmosphere (60-140 km) by optical radar," *Nature*, vol. **199**(1), pp. 1275–1276, 1963.

[2] A. V. Jelalian, *Laser radar systems.* Boston Artech, 1992.

[3] ZephIR 300 technical specifications, (ZephIR Lidar, 2014). http://www.zephirlidar.com/resources/technical-specs.

[4] WINDCUBE V2, a 200m vertical wind Doppler lidar, (Leosphere, 2014). http://www.leosphere.com/products/vertical-profiling/windcube-v2.

[5] WINDAR functional specifications, (WINDAR PHOTONICS, 2014). http://www.windarphotonics.com/product.

[6] F. Bingöl, J. Mann, and D. Foussekis, "Conically scanning lidar error in complex terrain," *Meteorologische Zeitschrift*, vol. **18**(2), pp. 189–195, 2009.

[7] S. Lang and E. McKeogh, "Lidar and sodar measurements of wind speed and direction in upland terrain for wind energy purposes," *Remote Sensing*, vol. **3**(9), pp. 1871–1901, 2011.

[8] T. Mikkelsen, N. Angelou, K. Hansen, M. Sjöholm, M. Harris, C. Slinger, P. Hadley, R. Scullion, G. Ellis, and G. Vives, "A spinner-integrated wind lidar for enhanced wind turbine control," *Wind Energ.*, vol. **16**(4), pp. 625–643, 2013.

[9] D. Schlipf, D. J. Schlipf, and M. Kühn, "Nonlinear model predictive control of wind turbines using lidar," *Wind Engineering*, vol. **16**(7), pp. 1107–1129, 2012.

[10] I. Antoniou, S. M. Pedersen, and P. B. Enevoldsen, "Wind shear and uncertainties in power curve measurement and wind resources," *Wind Engineering*, vol. **33**(5), pp. 449–468, 2010.

[11] C. J. Karlsson, F. A. Olsson, D. Letalick, and M. Harris, "All-fiber multifunction continuous-wave coherent laser radar at 1.55 μm for range, speed, vibration, and wind measurements," *Appl. Opt.*, vol. **39**(21), pp. 3716–3726, 2000.

[12] G. N. Pearson, P. J. Roberts, J. R. Eacock, and M. Harris, "Analysis of the performance of a coherent pulsed fiber lidar for aerosol backscatter applications," *Appl. Opt.*, vol. **41**(30), pp. 6442–6450, 2002.

[13] P. Lindelöw, "Fiber based coherent lidars for remote wind sensing," PhD dissertation, Dept. of Photon. Eng., Tech. Univ. of Denmark, Lyngby, Denmark, 2007.

[14] S. F. Jacobs, "Optical heterodyne (coherent) detection," *Am. J. Phys.*, vol. **56**(3), pp. 235–245, 1988.

[15] O. E. DeLange, "Optical heterodyne detection," *IEEE Spectr.*, vol. **5**(10), pp. 77–85, 1968.

[16] B. Razavi, "Design considerations for direct-conversion receivers," *IEEE Trans. Circuits Syst. II: Analog Digit. Signal Process*, vol. **44**(6), pp. 428–435, 1997.

[17] L. Richter, H. Mandelberg, M. Kruger, and P. McGrath, "Linewidth determination from self-heterodyne measurements with subcoherence delay times," *IEEE J. Quantum Electron.*, vol. **22**(11), pp. 2070–2074, 1986.

[18] M. Harris, G. N. Pearson, K. D. Ridley, C. J. Karlsson, F. A. A. Olsson, and D. Letalick, "Single-particle laser doppler anemometry at 1.55 μm," *Appl. Opt.*, vol. **40**(6), pp. 969–973, 2001.

[19] J. R. Barry and E. A. Lee, "Performance of coherent optical receivers," *Proc. IEEE*, vol. **78**(8), pp. 1369–1394, 1990.

[20] A. Valle and L. Pesquera, "Relative intensity noise of multitransverse-mode vertical-cavity surface-emitting lasers," *IEEE Photon. Technol. Lett*, vol. **13**(4), pp. 272–274, 2001.

[21] R. Stierlin, R. Bättig, P. D. Henchoz, and H. P. Weber, "Excess-noise suppression in a fiber-optic balanced heterodyne detection system," *OPT QUANT ELECTRON*, vol. **18**(6), pp. 445–454, 1986.

[22] L. Ma, Y. Hu, S. Xiong, Z. Meng, and Z. Hu, "Intensity noise and relaxation oscillation of a fiberlaser sensor array integrated in a single fiber," *Optics Letters*, vol. **35**(1), pp. 1795–1797, 2010.

[23] G. A. Cranch, M. A. Englund, and C. K. Kirkendal, "Intensity noise characteristics of erbium-doped distributed-feedback lasers," *IEEE J. Quantum Electron.*, vol. **39**(12), pp. 1579–1587, 2003.

[24] A. D. McCoy, L. B. Fu, M. Ibsen, B. C. Thomsen, and D. J. Richardson, "Relaxation oscillation noise suppression in fiber DFB lasers using a semiconductor optical amplifier," in Conference on Lasers and Electro-Optics, 2004 OSA CLEO Poster Session II (Optical Society of America, 2004), page CWA56.

[25] P. J. Rodrigo and C. Pedersen, "Comparative study of the performance of semiconductor laser based coherent Doppler lidars", Proc. SPIE **8241**, 824112 (2012).

[26] B. J. Rye and R. M. Hardesty, "Discrete spectral peak estimation in incoherent backscatter heterodyne lidar. i: Spectral accumulation and the Cramer-Rao lower bound," *IEEE Trans. Geosci. Remote Sens.*, vol. **31**(1), pp. 16–27, 1993.

[27] J. M. B. Dias and J. M. N. Leitão, "Nonparametric estimation of mean Doppler and spectral width," *IEEE Trans. Geosci. Remote Sens.*, vol. **38**(1), pp. 271–282, 2000.

[28] M. H. Hayes, *Statistical Digital Signal Processing and Modeling.* John Wiley & Sons, 1996.

[29] A. T. Pedersen, C. F. Abari, J. Mann, and T. Mikkelsen, "Theoretical and experimental signal-to-noise ratio assessment in new direction sensing continuous-wave Doppler lidar," in Proc. J. Phys.: Conf. Ser. **524 012004**.

[30] M. Harris, G. N. Pearson, J. M. Vaughan, and D. Letalick, "The role of laser coherence length in continuous-wave coherent laser radar," *J. Mod. Opt.*, vol. **45**(8), pp. 1567–1581, 2009.

[31] B. Moslehi, "Analysis of optical phase noise in fiber-optic systems employing a laser source with arbitrary coherence time," *J. Lightw. Technol.*, vol. **4**(9), pp. 1334–1351, 1986.

[32] C. A. Hill, M. Harris, and K. D. Ridley, "Fiber-based 1.5 μm lidar vibrometer in pulsed and continuous modes," *Appl. Opt.*, vol. **46**(20), pp. 4376–4385, 2007.

[33] C. Allen, Y. Cobanoglu, S. K. Chong, and S. Gogineni, "Development of a 1310-nm, coherent laser radar with RF pulse compression," in Proceedings of IEEE Geoscience and Remote Sensing Symposium (IEEE, 2000), pp. 1784–1786.

[34] L. G. Kazovsky, L. Curtis, W. C. Young, and N. K. Cheung, "All-fiber 90° optical hybrid for coherent communications," *Appl. Opt.*, vol. **26**(3), pp. 437–439, 1987.

[35] D. O. Hogenboom and C. A. DiMarzio, "Quadrature detection of a Doppler signal," *Appl. Opt.*, vol. **37**(13), pp. 2569–2572, 1998.

[36] N. Angelou, C. F. Abari, J. Mann, T. Mikkelsen, and M. Sjöholm, "Challenges in noise removal from Doppler spectra acquired by a continuous-wave lidar," presented at the 26th International Laser Radar Conference, Porto Heli, Greece, 25-29 June 2012.

Theoretical and experimental signal-to-noise ratio assessment in new direction sensing continuous-wave Doppler lidar

Paper II

Anders T. Pedersen, Cyrus F. Abari, Jakob Mann, and Torben Mikkelsen

Based on: A. T. Pedersen, C. F. Abari, J. Mann, and T. Mikkelsen, "Theoretical and experimental signal-to-noise ratio assessment in new direction sensing continuous-wave Doppler lidar," in proc. of J. Phys.: Conf. Ser. **524** 012004 doi:10.1088/1742-6596/524/1/012004.

Abstract

A new direction sensing continuous-wave Doppler lidar based on an image-reject homodyne receiver has recently been demonstrated at DTU Wind Energy, Technical University of Denmark. In this contribution we analyse the signal-to-noise ratio resulting from two different data processing methods both leading to the direction sensing capability. It is found that using the auto spectrum of the complex signal to determine the wind speed leads to a signal-to-noise ratio equivalent to that of a standard self-heterodyne receiver. Using the imaginary part of the cross spectrum to estimate the Doppler shift has the benefit of a zero-mean background spectrum, but comes at the expense of a decrease in the signal-to noise ratio by a factor of $\sqrt{2}$.

1 Introduction

Coherent Doppler lidars have in recent years started to play an increasingly important role within the wind energy industry and are now widely used for especially resource assessment. Lidars offer a cost-efficient and flexible alternative to in-situ anemometers, and met masts and several commercial products have found their way to the market. Despite being a well-established technology coherent Doppler lidars still represent a very active research field both in terms of the instruments themselves and their applications. Critical parameters such as accuracy and maximum measurement range are constantly being improved, and new features like controllable scanning patterns are emerging. For the application of lidars in wind energy the lidars seem to be moving from the ground to being mounted directly on the turbine, and e.g. power curve measurements from turbine mounted lidars have been demonstrated [1]. Another interesting application relates to turbine control where the aim is to maximise energy production and turbine lifetime through feed-forward yaw and pitch control using a turbine mounted lidar [2].

1.1 Direction sensing continuous-wave lidar

Continuous-wave (CW) Doppler wind lidars possess several desirable properties such as a simple basic design and a high duty cycle measuring rate, but unfortunately also some less desirable features such as limited measuring range and missing capability of sensing the direction of the wind. One can work around the latter limitation by shifting the frequency of the reference local oscillator (LO) compared to the transmitted signal, e.g. with the aid of an acousto-optic modulator (AOM). However, this approach has shown to lead to practical problems with instabilities in the Doppler spectrum especially at frequencies close to the acoustic frequency of the AOM and to effectively limit the bandwidth.

At DTU Wind Energy a different technique to achieve direction sensing has recently been demonstrated with great success [3]. This detection scheme is based on an image-reject homodyne receiver, also known as coherent in-phase and quadrature (IQ) detection, which in essence works by dividing the received backscattered signal in two and mixing one half with a reference local oscillator signal and the other half with a 90° delayed copy of the LO [4, 5]. By calculating the cross spectrum between these two signals the sign of the Doppler shift and thus the direction of the wind can be deduced. The cross spectrum between the two channels furthermore has the advantage of automatically eliminating any

DC component and background noise contributions thus making noise flattening obsolete in the post processing. In this study we analyze the signal-to-noise ratio (SNR) of the IQ detection lidar theoretically and experimentally, and compare with that of a lidar detection system using the standard self-heterodyne technique.

1.2 Experimental setup

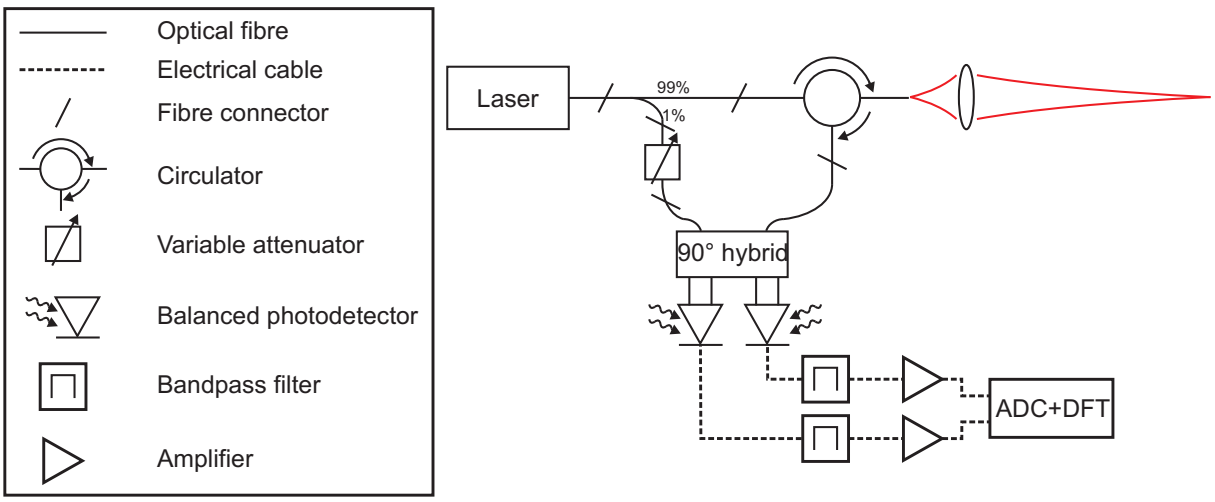

Figure 1: Schematic drawing of the direction sensing lidar used in this study.

Figure 1 shows a sketch of the setup for the direction sensing CW lidar used in this study. A 1565 nm CW fiber laser delivers an output power of approximately 1 W. This is sent to an optical circulator and from there to the telescope unit which focuses the light into the atmosphere. Light scattered back into the same mode as the output is collected by the telescope and directed back to the circulator and from here to the 90°-hybrid. Here the backscattered signal is mixed with the local oscillator signal (LO) which is tapped out from the laser output using a 1/99 optical splitter. The hybrid splits the received signal and the LO in two and introduces a 90° phase shift on one of the two LO signals before they are mixed on two balanced photodetectors. In order to achieve an appropriate optical power level on the detectors the LO can be attenuated before entering the hybrid. The two analog electrical detector output signals are bandpass filtered to condition them and avoid aliasing before they are amplified and finally digitised and processed by an FPGA board and a computer.

1.3 Data processing

Due to the phase shift induced by the 90° hybrid the photocurrents generated by the two photodetectors are 90° out of phase and may thus be written as

$$i(t) \propto \sin(\omega_D t + \phi) \tag{1.1}$$

$$q(t) \propto \pm\cos(\omega_D t + \phi), \tag{1.2}$$

where $i(t)$ and $q(t)$ are called the in-phase and quadrature-phase signal, respectively, and the sign of $q(t)$ depends on the sign of the wind velocity. ω_D is here the Doppler shift frequency and ϕ is an arbitrary phase constant.

The signals may be processed in three different ways. The first of these is the standard auto spectrum, S_I, of each signal which can be calculated according to

$$S_I(\omega) = \left\langle |I(\omega)|^2 \right\rangle = \left\langle |\mathcal{F}\{i(t)\}|^2 \right\rangle, \tag{1.3}$$

in the case of the in-phase signal. Here $\mathcal{F}\{\cdot\}$ denotes the Fourier transform, and$\langle\rangle$ the ensemble average.

The auto spectra of both i and q are symmetric, i.e. the positive and negative halves of the spectra are identical, and can therefore not be used directly to determine the direction of the wind. One way to achieve this is instead to calculate the auto spectrum of the complex signal, S_C, defined as

$$S_C(\omega) = \left\langle |I(\omega) + jQ(\omega)|^2 \right\rangle = \left\langle |\mathcal{F}\{i(t) + jq(t)\}|^2 \right\rangle, \tag{1.4}$$

where $j = \sqrt{-1}$ is the complex unit. This operation results in a spectrum in which the image component of the Doppler peak is eliminated. That is, the Doppler peak will only be present in either the positive or the negative half of the spectrum depending on the sign of the Doppler shift, see Figure 2a.

In the third data processing method the imaginary part of the cross spectrum, χ, between the two signals is used, i.e.

$$\mathrm{Im}\left(\chi(\omega)\right) = \left\langle \mathrm{Im}\left(I(\omega)Q^*(\omega)\right)\right\rangle = \left\langle \mathrm{Im}\left(\mathcal{F}\{i(t)\}\mathcal{F}^*\{q(t)\}\right)\right\rangle, \tag{1.5}$$

where $*$ denotes the complex conjugate and Im the imaginary part. This results in an anti-symmetric spectrum where the sign of the wind speed can be deduced from the sign of the Doppler peak, see Figure 2b.

Figure 2 shows measured examples of the latter two methods described above. As can be seen the auto spectrum of the complex signal has a Doppler peak located around -2 MHz which for this specific lidar system is equivalent to a wind speed of approximately -1.5 m/s. The shape of the background spectrum is determined by the combined frequency response of the detectors, bandpass filters, and amplifiers. For example can the effect of the lowpass edge of the filters clearly be seen to set in at ± 50 MHz. A strong DC component is also present and this is probably due to a slight offset in the ADC or an imbalance in the optical part of the system, or stray light due to reflections from optical components such as the telescope. The same information, i.e. wind speed and direction, can be deduced from the imaginary part of the cross spectrum where the negative peak indicates a negative wind speed. With this method the negative half of the spectrum thus becomes obsolete which can be advantageous when storing spectra. Another advantage of using the cross spectrum, as can be seen from the figure, is the zero-mean flat background noise spectrum. As a result it is not necessary to first measure the noise spectrum in order to normalise the spectrum [6].

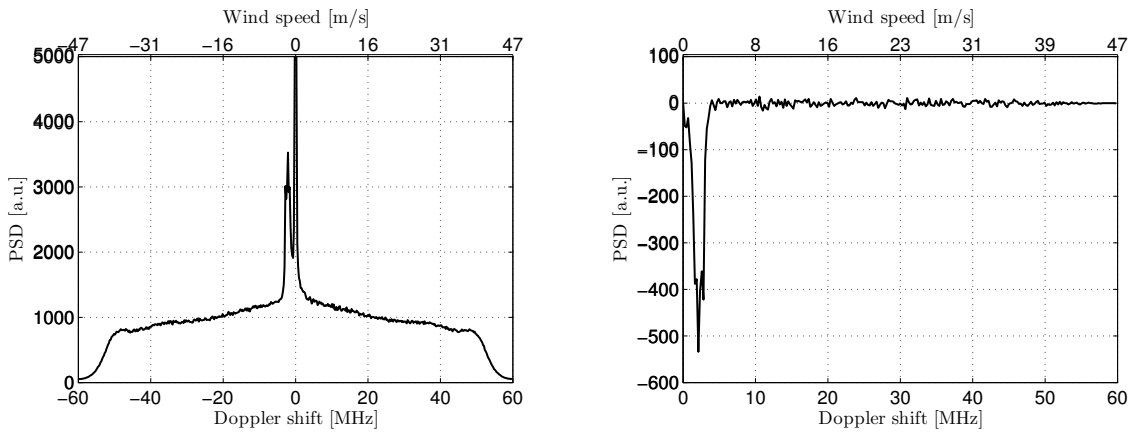

(a) (b)

Figure 2: (a) Auto spectrum of the complex signal, Eq. (1.4). (b) Imaginary part of cross spectrum, Eq. (1.5).

2 Signal-to-noise ratio

In this section we will calculate the relative signal-to-noise ratios of the three data processing methods described above. In the following we will assume spectra with equal noise statistics across the full bandwidth, i.e. the standard deviation of the noise is the same in all frequency bins. For convenience and since we will be working solely in the frequency domain the angular frequency, ω, will be omitted in the equations.

2.1 Auto spectrum of individual signals

The auto spectrum of either I or Q is

$$\langle |I|^2 \rangle = \langle |Q|^2 \rangle = \begin{cases} S + N & \text{at Doppler peak} \\ N & \text{outside Doppler peak,} \end{cases} \tag{2.1}$$

where S and N are the power spectral density of the signal and of the background noise, respectively. When performing actual measurements we do not have access to the ensemble average but rather the average of a number n of spectra, which is typically of the order of a few hundreds to a few thousands. We denote that average by $\langle\rangle_n$. So, for example, $\langle |I|^2 \rangle_n = \frac{1}{n}\left(|I_1|^2 + |I_2|^2 + \ldots + |I_n|^2\right)$, where I_k is the kth element from a series of consecutive Fourier amplitudes produced from a detector time series. It is reasonable to assume that I_k and I_l are independent (for $k \neq l$) for frequencies outside the Doppler peak, and also that the noise from the in-phase, I, and quadrature-phase, Q, signals are independent.

We now define the signal-to-noise ratio (SNR) as the signal power, i.e. how far the Doppler peak is above the noise floor, divided by the standard deviation of the noise level. So, for one of the detector signals, say I, the ratio is

$$\text{SNR} = \frac{(S+N) - N}{\sigma_n(N)} = \sqrt{n} S/N \equiv \text{SNR}_0, \tag{2.2}$$

where

$$\sigma_n^2(N) = \left\langle \left(\langle |I|^2 \rangle_n - \langle |I|^2 \rangle \right)^2 \right\rangle, \tag{2.3}$$

is the variance of the spectral estimate of the noise calculated at a frequency outside the Doppler peak. We denote the signal-to-noise ratio of this setup SNR_0 and use it as reference when comparing with the other methods. Assuming that the complex Fourier amplitudes are Gaussian one gets the standard result

$$\frac{\sigma_n^2(N)}{N^2} = \frac{1}{n}, \tag{2.4}$$

which was used in Eq. (2.2).

If we add the two auto spectra for I and Q the signal power will double but the standard deviation of the noise only increase by $\sqrt{2}$. Thus for $\langle |I|^2 \rangle + \langle |Q|^2 \rangle$ we get

$$\mathrm{SNR} = \sqrt{2}\mathrm{SNR}_0, \tag{2.5}$$

and thereby an improvement in SNR compared to the case only utilizing one of the two detectors by $\sqrt{2}$.

2.2 Auto spectrum of the complex signal

For the auto spectrum of the complex signal the spectral power is

$$\left\langle |I + jQ|^2 \right\rangle = \left\langle |I|^2 + |Q|^2 - jIQ^* + jI^*Q \right\rangle = \begin{cases} 4S + 2N & \text{at Doppler peak} \\ 2N & \text{outside Doppler peak,} \end{cases} \tag{2.6}$$

where it has been used that $\langle jI^*Q \rangle = -\langle jIQ^* \rangle = S$ at the Doppler peak and 0 outside the Doppler peak.

The uncertainty on the noise level is $\sigma_n(2N)/2N = 1/\sqrt{n}$ because the noise is a sum of n terms each having twice the variance as compared to the situation leading to Eq. (2.2). The implication is that the signal-to-noise ratio is

$$\mathrm{SNR} = \frac{4S}{\sigma_n(2N)} = 2S\frac{\sqrt{n}}{N} = 2\mathrm{SNR}_0, \tag{2.7}$$

which is seen to be twice as good as the signal from one of the individual detectors. This is intuitively not surprising since each detector only receives half of the total signal power in the setup used, but when using the output from both detectors and combing them as a complex signal the full signal power is utilized.

2.3 Cross spectrum

We now turn to the imaginary part of the cross spectrum between I and Q where the spectral power is given as

$$\mathrm{Im}\left(\langle IQ^* \rangle\right) = \begin{cases} \pm S & \text{at Doppler peak} \\ 0 & \text{outside Doppler peak.} \end{cases} \tag{2.8}$$

Due to the uncorrelated noise sources the average noise power at the output of the cross-spectral analyser is zero. However, we need to estimate the fluctuations around zero in order to use our signal-to-noise definition. We therefore need to estimate $\sigma_n^2(\mathrm{Im}(IQ^*))$ away from the Doppler peak. Here I and Q are uncorrelated Gaussian variables and the product IQ^* will have equal variance of the real and imaginary parts. So,

$$\sigma_n^2\left(\mathrm{Im}\left(IQ^*\right)\right) = \frac{1}{2}\sigma_n^2\left(IQ^*\right). \tag{2.9}$$

Since the mean of IQ^* is zero we can write the variance (at least for large n) as

$$\sigma_n^2\left(IQ^*\right) = \left\langle |\langle IQ^*\rangle_n|^2\right\rangle = \frac{1}{n^2}\left\langle |I_1Q_1^* + I_2Q_2^* + \ldots + I_nQ_n^*|^2\right\rangle. \tag{2.10}$$

Due to independence all the cross terms in the squared sum will vanish and we are left with n terms of the form $\langle I_kQ_k^*I_k^*Q_k\rangle$. Since the random variables are joint Gaussian and I and Q uncorrelated, this fourth order statistics can, due to Eq. (2.1), be expanded to products of second order statistics as $\langle I_kQ_k^*I_k^*Q_k\rangle = \langle |I_k|^2\rangle\langle |Q_k|^2\rangle = N^2$ (see the Isserlis relation in [7]). Combining these results we get

$$\frac{\sigma_n^2\left(\mathrm{Im}\left(IQ^*\right)\right)}{N^2} = \frac{1}{2n}, \tag{2.11}$$

and the signal-to-noise ratio becomes

$$\mathrm{SNR} = \frac{S/N}{1/\sqrt{2n}} = \sqrt{2}\mathrm{SNR}_0. \tag{2.12}$$

Hence it is seen that the penalty for achieving a flat background spectrum is a reduction in SNR of $\frac{1}{\sqrt{2}}$ relative to that of the auto spectrum of the complex signal.

The results derived in this section are summarized in Table 1 together with the experimental results.

3 Experiments

In order to test the validity of the results derived above two experiments were conducted. First the SNR was measured in the laboratory with the Doppler shift provided by a moving hard target, and secondly on a real atmospheric wind signal.

3.1 SNR from hard target

The SNR was measured in the laboratory using an experimental setup as shown in Figure 3 and with a telescope with a 1" aperture and 0.10 m focal length. The laser beam was focused weakly on a spinning paper disc adjusted to a relative speed of about 1 m/s and, in order not to saturate the detectors as well as to mimic a real atmospheric return signal, attenuated with a neutral density filter. The filter attenuated the signal by 25 dB upon each passage. The raw signals were sampled at 120 MS/s and processed using a 512 point discrete Fourier transform routine. $n = 4096$ of these spectra were averaged to a single

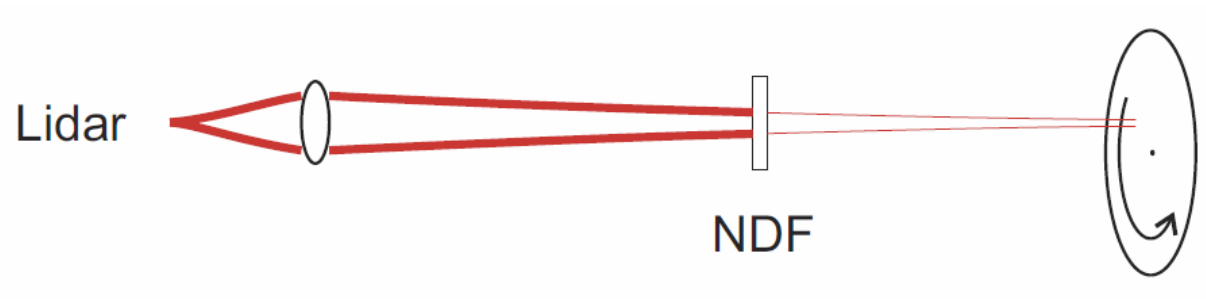

Figure 3: Schematic drawing of the setup used to measure the SNR from a moving hard target. The neutral density filter (NDF) attenuates the laser beam by 25 dB upon each passage.

output spectrum resulting in an output rate of approximately 57 Hz. Data was collected for 60 s. Subsequently the laser beam was blocked and another 60 s of data collected. From this the mean backgrounds of the different auto spectra were calculated and the spectra containing Doppler peaks were flattened by dividing with the respective mean background spectra. The SNRs were finally calculated by dividing the value in the bin containing the Doppler peak by the standard deviation of the bins not containing signal.

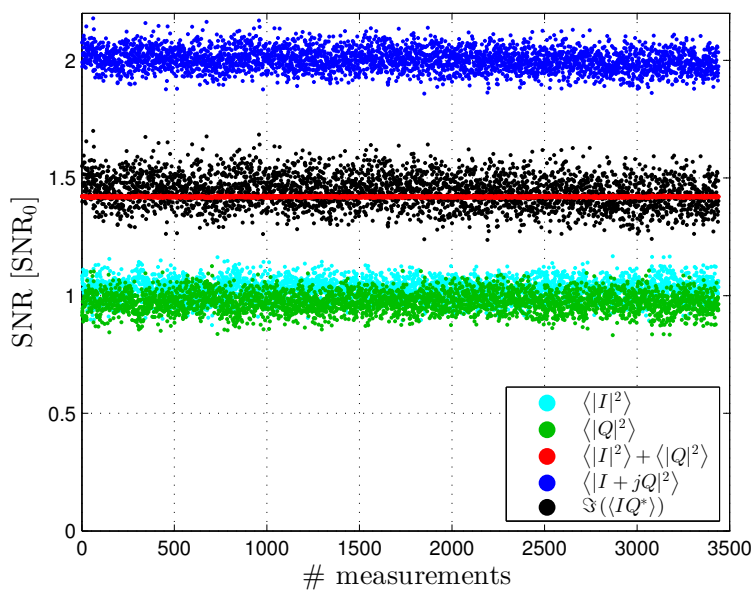

Figure 4: Scatter plot of the measured SNR from a moving hard target and based on the different data processing methods.

The results of the measurements are shown in Figure 4 in units of SNR_0 here calculated as the mean SNR of I and Q. First it is noted that there is a slight offset between the SNRs of channels I and Q. This is ascribed to an imbalance in either the optical or electrical part of the system and is the reason for calculating SNR_0 as an average. As

predicted by the derivations above the auto spectrum of the complex signal is seen to result in an SNR of two SNR_0 whereas the imaginary part of the cross spectrum only increases the SNR by approximately 1.44 which is very close to the numerical value of $\sqrt{2}$, see Table 1. One distinct feature stand out in the figure and that is that the variance of the $\langle|I|^2\rangle + \langle|Q|^2\rangle$ based SNR is much smaller than those of the other four. This is because SNR_0 is calculated as the mean of SNRs of the individual I and Q channels and any further imbalance between the two, e.g. due to changes in the polarisation of the backscattered light during a measurement period, will affect the complex signal and the cross spectrum, but for $\langle|I|^2\rangle + \langle|Q|^2\rangle$ they will cancel. The measurement is especially sensitive to changes in the polarisation of the backscattered light because the splitting ratio of the 90°-hybrid is polarisation sensitive, and any instability could therefore lead to the signal not being divided equally between channel I and Q.

3.2 SNR from atmospheric return

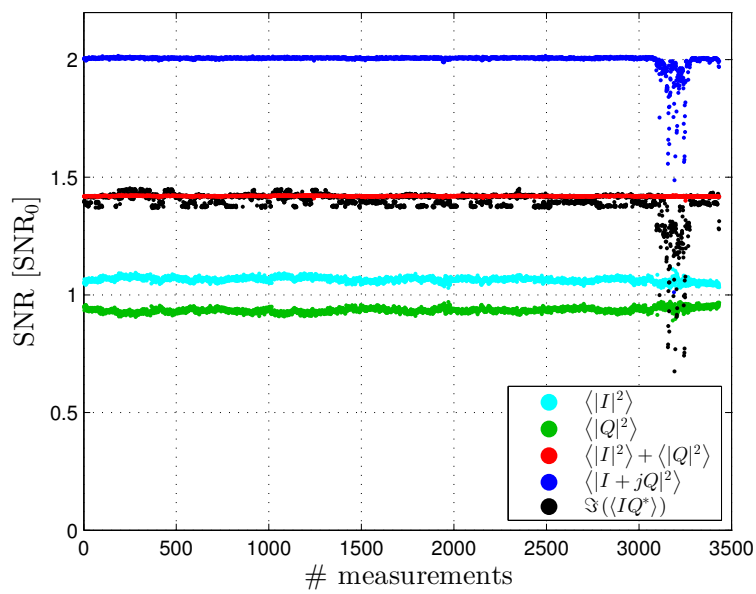

Figure 5: Scatter plot of the measured SNR from an atmospheric return and based on the different data processing methods.

For measuring the SNR of the return from the atmosphere the same procedure as for the hard target measurement was used, but this time using a telescope with a 3" aperture, and 0.28 m focal length and with the laser beam focused approximately 80 m from the lidar. The resulting SNR measurements are shown in Figure 5 and the averages of these measurements are shown in Table 1. Although the signal power is expected to have uncertainties due to broadening of the peak because of effects such as speckle broadening and turbulence, good agreement with the theoretical results is again seen; the mean SNR of the complex signal and of the imaginary part of the cross spectrum is 2.01 SNR_0 and 1.41 SNR_0, respectively. In these measurements a sudden drop in the SNR is seen in the

Table 1: SNR/SNR$_0$ for the different data processing methods comparing the theoretically expected values with the experimentally measured values.

	$\langle\|I\|^2\rangle$	$\langle\|Q\|^2\rangle$	$\langle\|I\|^2\rangle + \langle\|Q\|^2\rangle$	$\langle\|I + jQ\|^2\rangle$	$\mathrm{Im}\,(\langle IQ^*\rangle)$
Theoretical	1	1	$\sqrt{2}$	2	$\sqrt{2}$
Exp. hard target	1.03	0.97	1.42	2.00	1.44
Exp. atm.	1.07	0.93	1.42	2.01	1.41

end of the time series and these are due to natural variations in the wind speed. When the wind speed approaches 0 m/s the Doppler peak is attenuated by the high pass edge of the bandpass filters with a decreasing SNR as a result. Also a much smaller variance in the measured SNR than for the hard target measurement is seen. A possible explanation for this could be is the polarisation state of light is better preserved in the scattering process with aerosols in the air than with the hard target. However, further investigation is necessary in order to clarify this.

4 Discussion and conclusion

A direction sensing CW lidar has been constructed by incorporating a 90° hybrid into a basic CW lidar setup. The 90° is a completely passive component and requires thus no external control and is less prone to add noise to the measurement as compared to using active components such as an AOM. There are two ways of processing the signals generated by the lidar; calculate either the auto spectrum of the complex signal or the imaginary part of the cross spectrum. The latter method has the very appealing properties of a zero-mean flat background noise spectrum and that all information is contained in the positive half of the spectrum reducing the requirements on data storage. However, we show theoretically and experimentally that these attractive features come at the expense of a reduction in SNR by a factor of $\sqrt{2}$, that is by approximately -1.5 dB. This reduction in SNR will in most situations not limit the operation of the lidar, but under conditions with very clear air or very fast measurements it must be taken into consideration, e.g by increasing the laser output power or perhaps use the auto spectrum of the complex signal instead. Also for Doppler shifts close to zero the auto spectrum of the complex signal may be advantageous to use because if the Doppler spectrum is perfectly centered around zero the resulting positive and negative peaks of the imaginary part of the cross spectrum will cancel. On the other hand, due to the elimination of the need to normalise the spectrum, necessary for the derivation of accurate wind speeds, the cross-spectral technique does not introduce any estimation error which is inherent to any estimation algorithm. A thorough analysis of the impact on the SNR due to spectral whitening is beyond the scope of this paper and is to be investigated in future a work.

5 Acknowledgments

This work was supported by "WINDSCANNER - The European ESFRI WindScanner research infrastructure facility" FP7-Infrastructures-2012-1 grant no. 312372.

The resources provided by the Center for Computational Wind Turbine Aerodynamics and Atmospheric Turbulence funded by the Danish Council for Strategic Research grant no. 09-067216 are also acknowledged.
JM would like to thank for the grant provided by the Ingeborg and Leo Dannin foundation.

References

[1] R. Wagner, T. Pedersen, M. Courtney, I. Antoniou, S. Davoust, and R. L. Rivera, "Power curve measurement with a nacelle mounted lidar," *wind Energy*, vol. 17, pp. 1441–1453, 2014.

[2] E. Bossanyi, B. Savini, M. Iribas, M. Hau, B. Fischer, D. Schlipf, T. van Engelen, M. Rossetti, and C. E. Carcangiu, "Advanced controller research for multi-MW wind turbines in the UPWIND project," *wind Energy*, vol. 15, pp. 119–145, 2012.

[3] J. Mann, A. T. Pedersen, E. Dellwik, E. Simley, C. F. Abari, and T. Mikkelsen, "Experimental demonstration of an image-reject cw coherent Doppler lidar," proc. of ISARS - 17th Int. Symp. for the Advancement of Boundary-Layer Remote Sensing.

[4] C. Wang, L. Gao, Y. Li, and H. Cong, "Investigation of balanced detection and receiver for coherent lidar," proc. SPIE7382, doi:10.1117/12.829459 (2009).

[5] C. F. Abari, A. T. Pedersen, P. J. Rodrigo, M. Sjoholm, C. Peucheret, T. Mikkelsen, and M. J, "A homodyne image-reject optical front-end receiver architecture for improved signal detection in coherent Doppler lidars," presented at the 17th Int. Symp. for the Advancement of Boundary-Layer Remote Sensing, Auckland, New Zealand, 2014.

[6] N. Angelou, C. F. Abari, J. Mann, T. Mikkelsen, and M. Sjöholm, "Challenges in noise removal from Doppler spectra acquired by a continuous-wave lidar," presented at the 26th International Laser Radar Conference, Porto Heli, Greece, 25-29 June 2012.

[7] L. Koopmans, *The spectral analysis of time series.* Academic Press, 1974.

Performance evaluation of an all-fiber image-reject homodyne coherent Doppler wind lidar

Paper III

Cyrus F. Abari, Anders T. Pedersen, Ebba Dellwik, and Jakob Mann

Based on: C. F. Abari, A. T. Pedersen, E. Dellwik, and J. Mann, "Performance evaluation of an all-fiber image-reject homodyne coherent Doppler wind lidar," Atmos. Meas. Tech. Discuss., vol. 8, pp. 3729-3752, 2015.

Abstract

The main purpose of this study is to evaluate the near-zero wind velocity measurement performance of two separate 1.5 μm all-fiber coherent Doppler lidars (CDL). The performance characterization is performed through the presentation of the results from two separate atmospheric field campaigns. In one campaign, a recently developed continuous wave (CW) CDL benefiting from an image-reject front-end was deployed. The other campaign utilized a different CW CDL, benefiting from a heterodyne receiver with intermediate frequency (IF) sampling. In both field campaigns the results are compared against a sonic anemometer, as the reference instrument. The measurements clearly show that the image-reject architecture results in more accurate measurements of radial wind velocities close to zero. Close-to-zero velocities are usually associated with the vertical component of the wind and are important to characterize.

1 Introduction

Light detection and ranging (lidar) for remote sensing of wind has become a well-established and widely used instrument in atmospheric science and wind energy [1–7]. Among different variants of lidars, coherent Doppler lidars (CDL) are of primary interest for remote measurement of wind as well as characterization of turbulence structures for the lower atmosphere [8–10]. Due to their nature of operation, CDLs measure the radial velocity of the wind which does not necessarily coincide with the true velocity vector. Thus, one ideally needs to employ three lidars, with a sufficient angular separation, for probing the measurement volumes of interest to be able to derive the full wind velocity vector. One of the challenges in existing CDLs is the detection of the radial velocity direction. Among the few commercially available continuous wave (CW) systems none is capable of determining the radial velocity direction.

A few research CW CDLs, capable of determining the sign of the radial velocity, have been developed over the years. For instance, Schwiesow and Cupp [11] used two CO_2 lasers with frequency-offset locking to discriminate the radial velocity direction. The system benefits from a down-conversion principle known as heterodyne receiver with intermediate frequency (IF) sampling [12, 13]. However, the reported signal to noise ratio (SNR) around zero velocity in this system was poor. More recently, a CW CDL capable of determining the radial velocity sign/direction is the 1st-generation "Windscanner" [14] also benefiting from a heterodyne receiver with IF sampling. In this system an acousto-optic modulator (AOM) is used to provide a frequency shift (offset) between the local oscillator (LO) signal and the transmit signal. As an all-fiber directional CW CDL, the 1st-generation Windscanner has been a valuable research instrument for directional remote sensing of wind. A detailed analysis of systems benefiting from the heterodyne front-ends with IF sampling is beyond the scope of this paper. Suffice to mention that they may suffer from a number of drawbacks in terms of (more) extraneous noise, (lower) detection bandwidth (BW), as well as (more) intensive data acquisition and processing. Some of these issues are briefly discussed in the remainder of this paper.

Recently, an all-fiber directional CW CDL employing an image-reject homodyne optical front-end was successfully demonstrated by Abari et al. [15]. This reported sys-

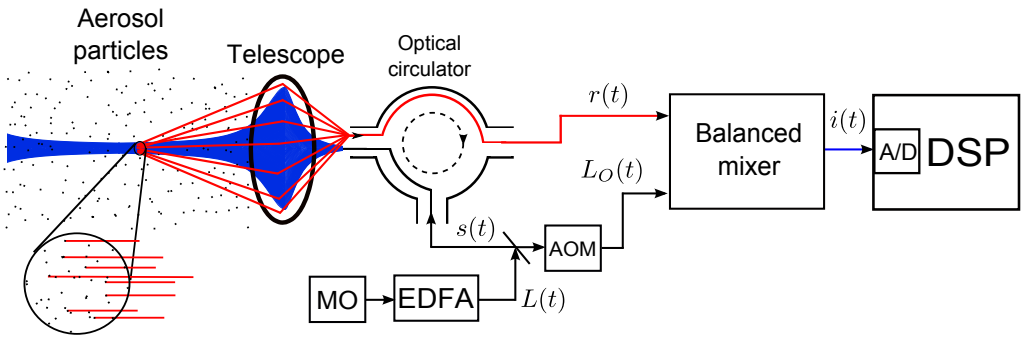

Figure 1: Heterodyne receiver with IF sampling (HCDL). To be able to capture the full return signal power a balanced mixer/detector needs to be employed; for details please see [15]. MO and EDFA represent the master oscillator and erbium-doped fiber amplifier, respectively. Optical circulator isolates the transmit , $s(t)$, and the receive signal, $r(t)$. $L_o(t)$ represents the local oscillator signal.

tem utilizes an all-fiber 90^0 hybrid [16], conventionally employed in high-speed optical-communications, to optically down-convert the desired signals to baseband. As opposed to the heterodyne receivers with IF sampling, the optical down-conversion is carried out with passive components, only. As a result, the noise behavior of the system, especially around the zero Doppler shift, is improved. Besides, the system reduces the BW of the photo-detectors as well as the A/D by a factor of two. Abari et al. [15] have shown that due to the presence of two signal components with independent noise sources, a cross-spectral analysis technique can be utilized to remove the unnecessary noise sources in the system, eliminating the additional intensive signal processing for the removal of the background noise.

To evaluate the performance of the all-fiber image-reject system (see Abari et al. [15]), its performance was compared against a sonic anemometer in a field campaign. The measurements were specifically carried out to measure the vertical component of the wind vector: The vertical component is usually very small and appears in the the frequency region where CW CDLs generally suffer from a multitude of noise sources, such as offset noise, interferometric noise, $1/f$ noise, etc. For comparison purposes, the results of this campaign are compared with the results of a different campaign carried out in 2013 where three 1st-generation Windscanners (benefiting from an AOM-based heterodyne receiver with IF sampling) were utilized to measure the 3D wind vector. For the latter, only the results associated with measured radial velocities close to zero are discussed in this paper so that a fair comparison between the above mentioned systems can be done.

This paper starts with a brief and simple introduction, in terms of baseband signal models, to the image-reject architecture and how it compares to the heterodyne architecture with IF sampling. We also discuss the advantages and disadvantages of a signal processing approach, introduced in [15] and further analyzed in [17], to remove the dominant noise sources and eliminate spectral whitening. Then, we will present some of the measurement results relevant to this paper for two separate measurement campaigns where the 1st-generation Windscanners and a prototype CW CDL, benefiting from image-reject

homodyne receiver [15], were deployed for remote sensing of wind. Finally, the paper is wrapped up with a few concluding remarks. Throughout this paper, we will use ICDL and HCDL to refer to the CW CDL benefiting from image-reject front-end and 1st-generation Windscanner CW CDLs (an AOM-based heterodyne receiver with IF sampling), respectively.

2 Image-reject optical receiver in CW CDLs and spectral processing

One of the most well-known and widely used optical front-end architectures in CW CDLs is the homodyne receiver with real mixing [18]. A detailed analysis of this system, as well as other architectures, is not the purpose of this paper. The interested reader can refer to [15] and [18] for more information. In such a system, a simplified transmit signal can be expressed as

$$s(t) \propto \cos\left(2\pi f_c t\right), \tag{2.1}$$

where f_c is the optical carrier frequency. As a result, the baseband signal associated with backscatter from a single moving particle can be written as

$$i(t) = \alpha \cos\left(2\pi \Delta f t\right) \tag{2.2}$$

where α, among other things, represents the net effect of transmit optical power, atmospheric transmission, scattering, telescope area, and the receiver efficiency. In Eq. (2.2) we have ignored any parameters (such as phase shift) secondary to the concepts discussed in this paper. Please note that Eq. (2.2) represents both negative and positive Doppler shifts. As a result, due to its symmetric spectrum with respect to the zero frequency it is impossible to infer the direction of the radial velocity. Fig. 1 illustrates an example of a HCDL where the role of the acousto-optic modulator (AOM) is to shift the local oscillator (LO) frequency to an IF offset to enable the discrimination of negative and positive radial velocities.[1] Assuming similar operating conditions, the detected signal, in the baseband form, for the transmit signal in Eq. (2.1) is

$$i(t) = \alpha \cos\left(2\pi f_{IF} t \pm 2\pi \Delta f t\right). \tag{2.3}$$

As we can see from Eq. (2.3), it is relatively simple to extract the sign of the radial velocity as well as its magnitude; the sign can be inferred by comparing the Doppler shift with respect to the IF. However, we know from experience that a few imperfections contribute to the corruption of the desired Doppler signal components close to IF. We believe the main sources of spurious signals are leakage from the optical circulator, back reflections from the telescope [2], and a challenging offset noise removal at the IF frequency. Besides,

[1] Alternatively, the transmit (or receive) signal can be frequency shifted. In 1st-generation Windscanners, the transmit signal is frequency shifted.

[2] In CW CDLs, the presence of non-ideal characteristics of the optical circulator and anti-reflection coating may give rise to an unwanted signal in the vicinity of the zero-velocity Doppler component. The unwanted signal is known as the interferometric noise. [19] can be consulted for a thorough analysis of interferometric noise in coherent fiber-optic systems.

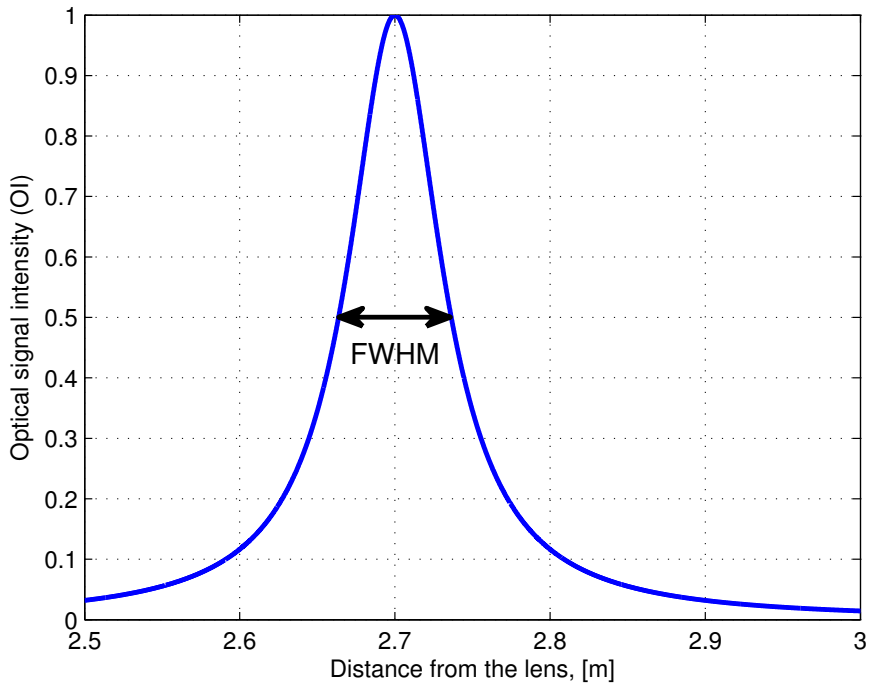

Figure 2: Optical signal intensity as a function of distance from the output lens of a telescope. For an effective aperture diameter of 2 cm, the FWHM at a focus distance of 2.7 m is about 72 mm. Due to beam truncation at the output lens in our system, the measured FWHM is 140 mm.

possible AOM imperfections, such as a dirty AOM radio frequency (RF) drive and the zeroth-order component leakage may contribute to additional noise in the system. As a result, an accurate measurement of small Doppler shifts (associated with wind speeds close to zero) becomes more cumbersome and sometimes even impossible.

A thorough analysis of an all-fiber image-reject homodyne receiver has been provided in [15]. This system utilized a receiver employing two signal detection arms, in-phase (I) and quadrature-phase (Q) components. The combination of the I and Q signal components results in a complex-valued signal

$$i(t) = i_I(t) + j i_Q(t) = \frac{\alpha\sqrt{2}}{2}\cos\left(2\pi\Delta f t\right) \pm j\frac{\alpha\sqrt{2}}{2}\sin\left(2\pi\Delta f t\right), \tag{2.4}$$

where $j = \sqrt{-1}$. Furthermore, $i_I(t)$ and $i_Q(t)$ are the baseband I and Q components, respectively. It can readily be seen that by comparing the I and Q components in Eq. (2.4), the radial velocity sign can be inferred. Furthermore, we have shown in [15] that there are two approaches to retrieve the velocity component from the spectral analysis of Eq. (2.4), i.e., auto-spectral analysis of the complex signal or the cross-spectral analysis of the in-phase and quadrature components. For the remainder of this paper, we use the term cross-spectral approach when referring to the cross-spectrum between the in-phase and quadrature components of the baseband signal in Eq. (2.4). The cross-spectral

approach seems to be the obvious option in the majority of measurements due to its ability to remove, at least on average, the uncorrelated noise sources such as the dominant detector's shot noise. The main advantage of this approach, for the majority of scenarios, is the elimination of additional signal processing algorithms, such as spectral whitening, that may introduce additional estimation noise. However, as will be shown shortly, the cross-spectral approach cannot be reliably employed for a small number of measurement cases using the ICDL where the Doppler spectra leaks across the zero frequency.

Following Eqs. (25) and (26) in [15] it is evident that the cross-spectral approach works best when the spectral components are to the one side of the zero frequency. In other words, the Doppler shifts associated with the backscatter are either all positive or negative, i.e., they do not leak across the zero frequency. This is, of course, the case for the majority of scenarios. However, as we will show in this paper, the estimation of Doppler shifts distributed around zero frequency for cross-spectral approach becomes skewed and biased. For instance, if the vertical velocity component measurement associated with a large sampling volume is carried out, it is highly probable to observe a wide distribution of velocities which cross the zero frequency. This is indirectly due to the incapability of lidars to provide point measurements; CDLs always provide a volume measurement. In the event of CW CDLs, the sampling volume is primarily a function of the output lens diameter and measurement range.

For an untruncated Gaussian beam, the transmit laser beam's optical intensity has a Lorentzian distribution defined by

$$\mathrm{OI} = \frac{\Gamma}{\pi\left[(F-d)^2+\Gamma^2\right]}, \tag{2.5}$$

where λ is the wavelength, d, and F are the distance and focus distance of the light with respect to the output lens of the telescope, respectively. Furthermore,

$$\Gamma = \frac{4\lambda F^2}{\pi D_{\mathrm{eff}}^2}, \tag{2.6}$$

where D_{eff} is the output lens effective diameter, i.e., where the transmit beam radial intensity drops to $1/e^2$ (see [20]). For an effective antenna diameter of 2 cm and a focus distance of 2.7 m the full-width-half-maximum (FWHM) of the beam (as shown in Fig. 2) is 72 mm (see [20, 21]). In our experiment the lens diameter (not the effective diameter) was a mere $D = 2.2$ cm. Due to beam truncation (see [22]) at the output lens of the telescope in our system the FWHM at the focus distance deviated from the untrucated beam in Eq. (2.5). Our measurements indicated a FWHM of 140 mm at a focus distance of 2.7 m at the time of measurement. This width corresponds approximately to the 115 mm gap of the sonic [23] used for the verification of the measurement results, elaborated in Sec. 3. Following Eq. (2.6) it can be inferred that the FWHM varies quadratically as a function of the focus distance.

To demonstrate the performance of the cross-spectral approach, in the event of Doppler spectral power at both sides of zero frequency, let us assume a simple case of optical backscatter from two individual aerosol particles. The two particles have Doppler shifts equal in magnitude but opposite in sign, with baseband coefficients α and β associated

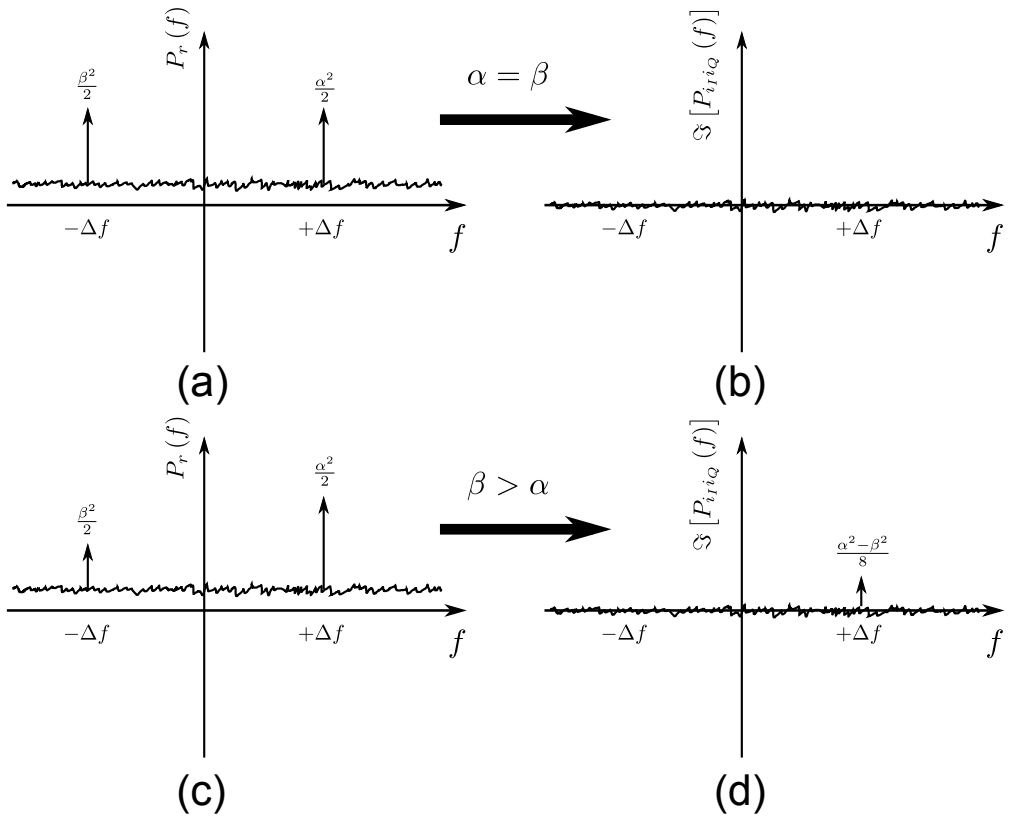

Figure 3: Cross-spectral approach in the event of spectral components appearing on both sides of zero frequency. Examples of auto-spectra are shown in the left column while the corresponding cross-spectra are shown in the right.

with positive and negative Doppler shifts, respectively. Thus, assuming the transmit signal in Eq. (2.1) and following the image-reject architecture elaborated in [15], the following baseband complex signal can be formulated

$$i(t) = i_I(t) + j i_Q(t) = \frac{\sqrt{2}\,(\alpha+\beta)}{2}\cos\left(2\pi\Delta f t\right) + j\frac{\sqrt{2}\,(\alpha-\beta)}{2}\sin\left(2\pi\Delta f t\right). \tag{2.7}$$

Moreover, assuming the desired Doppler signal information is contained in the imaginary part of the cross spectrum between I and Q [15,]

$$\mathrm{Im}\left[P_{i_I i_Q}\right] = \frac{(\alpha+\beta)(\alpha-\beta)}{8}\left[\delta\left(f+\Delta f\right) - \delta\left(f-\Delta f\right)\right], \tag{2.8}$$

$\mathrm{Im}\left[P_{i_I i_Q}\right]$ represents the imaginary component of the cross-spectrum between I and Q.

To asses the performance of the cross-spectral approach, let us consider three different scenarios:

1. If $\beta \to 0$, then
$$\mathrm{Im}\left[P_{i_I i_Q}\right] = \frac{\alpha^2}{8}\left[\delta\left(f+\Delta f\right) - \delta\left(f-\Delta f\right)\right]. \tag{2.9}$$
which is a better spectral estimator, compared to the auto-spectral method, as elaborated in [15] and [17]. This is a very common measurement scenario since simultaneous occurrence of Doppler spectral components with opposite sign is rare and is expected in specific conditions, e.g., vertical wind component measurement in turbulent flow or large sampling volume.

2. If $\beta = \alpha$, then
$$\mathrm{Im}\left[P_{i_I i_Q}\right] = 0. \tag{2.10}$$
In this case, contrary to the auto-spectral procedure, the estimator fails to detect the presence of a Doppler signal. However, the center of gravity and median estimators, explained in what follows, are able to produce the correct average Doppler shift associated with the sampling volume.

3. If $\beta \neq \alpha, \beta \neq 0$, then Eq. (2.8) detects a single signal component which might be negative or positive depending whether $\beta > \alpha$ or $\beta < \alpha$. This may result in an inaccurate detection/estimation of the Doppler shift and introduce a bias in the measurement volume averaged velocity estimate away from zero.

As a result, although cross-spectral approach provides a reliable and convenient way for Doppler shift estimation in the majority of cases, it fails to provide unbiased velocity estimates when Doppler components spread across the zero frequency.

On the other hand, more often than not, we are interested in the mean value of the Doppler shift as it represents the dominant wind velocity in the sampling volume. Thus, is it possible to utilize the cross-spectral approach when one is interested in the average value of the wind velocity in the sampling volume? To answer this question, let's take the two practical estimators conventionally used for the sampling-volume average wind velocity estimation, i.e., the center of gravity and median estimators.

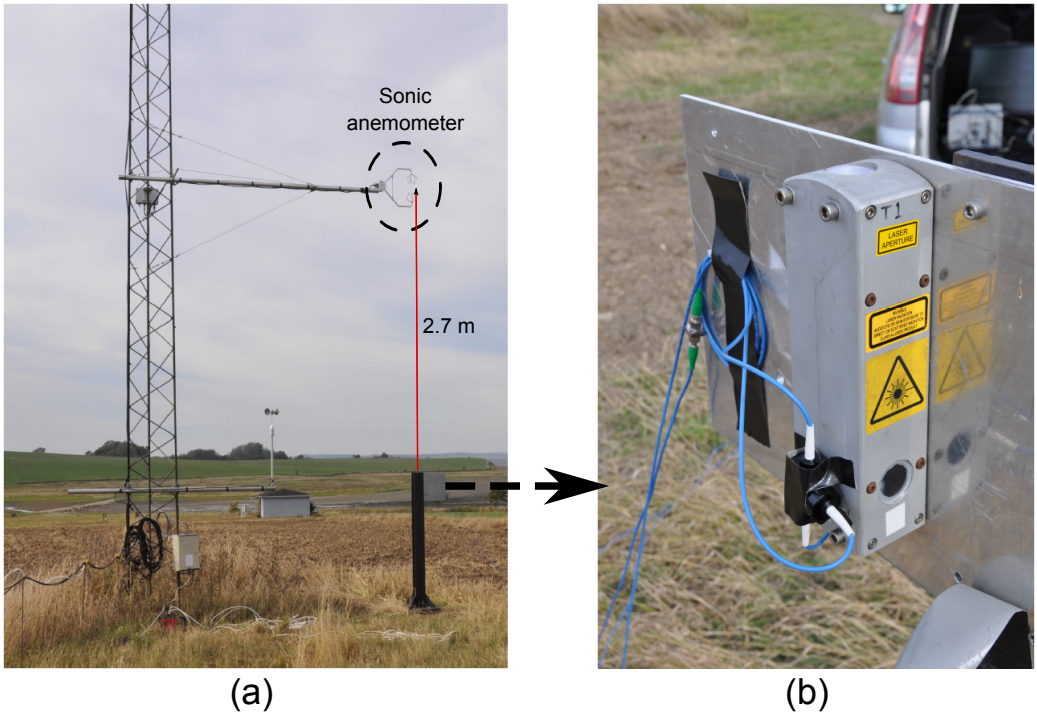

Figure 4: Field campaign at Risø campus of the Technical University of Denmark. Fig. (a) shows the position of the ICDL's output antenna with respect to the sonic. Fig. (b) is an expanded view of the mounting plate for the antenna, viewed from the backside of the plate seen in Fig. (a).

Table 1: Measurement campaign system parameters. p_t, BW, and f_s represent the optical output power, detection bandwidth, and sampling frequency, respectively. Furthermore, N and M represent the number of DFT points and spectral averaging, respectively. Periodograms [25] were used for the estimation of spectra as elaborated in [15].

F [m]	D [cm]	FWHM [mm]	λ [nm]	p_t [W]	BW [MHz]	f_s [MHz]	N	M
2.7	2.2	140	1565	0.95	50	120	512	3900

The mean (center of gravity) Doppler shift estimator, operating on a PSD (treated as a PDF of Doppler shifts), is

$$\mu_f = \int f P_r(f)\, df / \int P_r(f)\, df, \tag{2.11}$$

where μ_f is the mean Doppler shift. It can be easily shown that

$$\int f P_r(f)\, df = 2 \int f \mathrm{Im}\left[P_{i_I i_Q}(f)\right]^- df, \tag{2.12}$$

where $\mathrm{Im}\left[P_{i_I i_Q}(f)\right]^-$ is the one-sided spectrum, (see [15]. At first glance the center of gravity estimator should be able to operate on the cross-spectral approach. However, to estimate the center of gravity, the spectrum needs to be normalized, hence the normalization factor in the denominator of Eq. (2.11). Replacing $P_r(f)$ in Eq. (2.11) with $\mathrm{Im}\left[P_{i_I i_Q}(f)\right]^-$ associated with the spectrum in Fig. 3d results in Δf which deviates from the true center of gravity estimate, i.e., $(\alpha^2 - \beta^2)\Delta f/(\alpha^2 + \beta^2)$. The median estimator of the Doppler shifts is defined by

$$\int_{-\infty}^{\tilde{f}} P(f)\, df = \frac{1}{2} \int_{-\infty}^{+\infty} P(f)\, df, \tag{2.13}$$

where $\tilde{f}$ is the median frequency. It is trivial to show that the median estimator for the average velocity retrieval fails to provide an accurate estimate when operating on $\mathrm{Im}\left[P_{i_I i_Q}(f)\right]^-$. As a result, the auto-spectrum of the signal, $P_r(f)$, needs to be utilized. The median estimator turns out to exhibit a lower variance [24], when compared to the center of gravity estimator. Once the median (or mean) value of Doppler shifts are estimated, it is trivial to find the corresponding median wind speed by

$$\tilde{v} = \frac{1}{2}\lambda \tilde{f}. \tag{2.14}$$

Using the auto-spectrum in Eqs. (2.11) and (2.13), requires the dominant background noise to be removed (a rather signal processing intensive procedure that can introduce an additional estimation error).

Following the above discussion, the cross-spectral approach cannot be reliably used when estimating either the mean or median value of the vertical wind component since there is a possibility for spectral cancellation across the zero frequency. The chances for spectral cancellation are even higher when measurements are done in turbulent flows and

large sampling volumes. As shown in Eq. (2.5), the sampling volume increases quadratically as a function of distance from the transceiver antenna. Thus, more precautions should be taken when measurements are done for long ranges.

On the other hand, the cross-spectral approach is a very effective way for mean/median Doppler shift estimation in the event of Doppler spectra being confined to either side of the zero frequency. Hence, a combination of cross-spectral and auto-spectral approach can be employed for an efficient estimation of mean wind velocity in ICDLs. For instance, a real-time automated algorithm can primarily benefit from a cross-spectral approach to estimate the Doppler shifts. If the estimated shift is inside a predefined confidence interval, e.g., ± 1 m/s, the auto-spectral approach can be revoked to estimate the mean value of the Doppler shift.

In this paper, we have simply relied on the auto-spectral approach for the median Doppler shift estimation. This is justified by the fact that in this particular campaign we have purposefully performed the measurements for the vertical wind velocity component, only. As we will see in Sec. 3, the results illustrate a significant improvement over the measurements performed by a HCDL.

3 Measurement results

Two separate and independent measurement campaigns were carried out to verify the results from the deployed CW CDLs against a sonic anemometer. In the first measurement campaign, carried out at the Risø campus of the Technical University of Denmark (October-November, 2013), three HCDLs and one 3D CSAT sonic anemometer (Cambell scientific) were utilized. The HCDLs were carefully positioned around the mast shown in Fig. 4a and focused on the measurement center of the sonic anemometer, which for this experiment was located around 6 m from the ground. The three wind lidars were tilted and measured at an angle of approximately 35 ° degrees. The FWHM of the measurement volume was 90 mm which is comparable to the path length of the sonic anemometer (115 mm). The main purpose of this experiment at the time was to investigate the possibility of calibrating the sonic anemometer using the wind lidar. As mentioned before, only a subset of data representing wind measurements close to zero velocity, taken from only one HCDL, are used for comparison purposes in this paper.

In a later measurement campaign, carried out in January, 2014, we made use of a prototype ICDL elaborated in [15]. The parameters for the system are listed in Table 1. To measure the vertical component of the wind, where observation of near-zero velocities are maximized, the beam at the output of the telescope was aligned vertically and the beam was focused at the measurement center of the sonic anemometer. Fig. 4 shows the field deployment of the instrument for this specific campaign. Due to the direction of wind during both measurement campaigns, the effect of mast shadowing was minimal.

Figs. 5a and 5b illustrate the probability distribution function (PDF) of the measured velocities for the measurement campaign carried out by the HCDL. Fig. 5b is an example associated with PDF of velocities away from the IF frequency (zero Doppler shift) while Fig. 5a illustrates the PDF of velocities around the IF offset, i.e., zero radial velocity. As it can be seen from Figs. 5a and 5b the performance of the lidar, compared against the

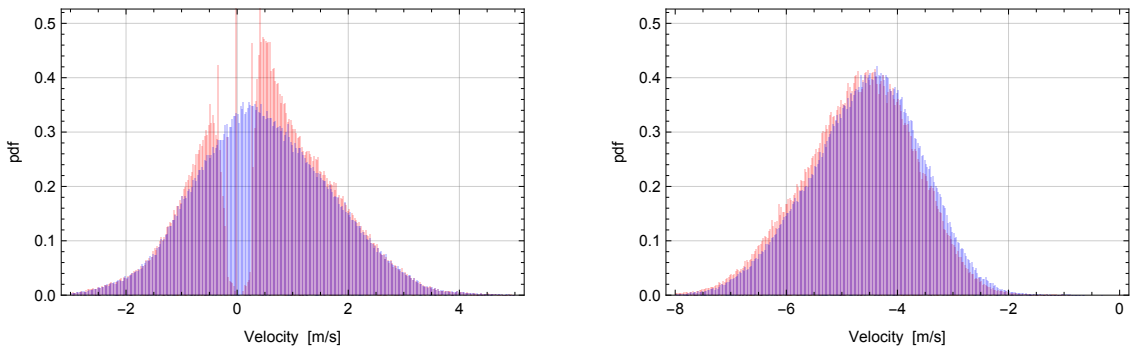

(a) Vicinity of zero velocity (b) Away from zero velocity

Figure 5: The PDF of estimated median velocities; in both figures, blue and red represent the measurements performed by the sonic and heterodyne CW CDL (HCDL), respectively. Please observe the gap in the PDF of velocities associated with the HCDL in (a). The over-shoots (when compared to the blue PDF) correspond to the accumulation of the estimated velocities associated with the frequencies away from zero as well as the inaccurately estimated velocities associated with the frequencies inside the gap.

sonic, is consistent across the displayed velocity range[3]. However, the measured close-to-zero velocities are either impossible to estimate or significantly biased, when compared to the sonic. This is mainly due to the presence of spurious effects around the IF offset.

Fig. 6 illustrates the PDF of the velocities measured by the ICDL, acquired during the latest field campaign. It is obvious that, when compared to the HCDL, the estimated mean velocities around zero are more consistent with the measurements performed by the sonic. This is mainly the direct consequence of using passive components for radial sign detection, elaborated in [15], as opposed to the AOM (an active component), introducing additional spurious effects. Moreover, the need for notch filters, band-pass filters with a very narrow frequency band, for attenuating the strong IF offset is eliminated. From experience, the analogue notch filters are costly, difficult to design, and often suffer from non-symmetric response. They also suffer from environmental effects such as temperature dependency. The image-reject receiver, though, benefits from a high-pass filter for removing the DC offset which is more robust and has better frequency response characteristics.

Figs. 7a and 7b show the estimated median velocities sorted in ascending order. The velocity range has been selected to be in the vicinity of the zero frequency shift. The estimated mean wind velocities, associated with the measurement volume, show a one-to-one correspondence between the sonic and lidar. Wind speed values in Figs. 7a and 7b are associated with data in Figs. 5a and 6, respectively. In these figures, the red curve is a linear fit to the measured data. An ideal one-to-one correspondence between the lidar and sonic should result in a straight line with a slope of one, passing through the center. For the campaign associated with the HCDL, Fig. 7a, a significant deviation from the reference instrument is observed (as expected). The deviations for the ICDL, Fig. 7b,

[3]In Fig. 5b a shift of approximately 0.1 m/s can be seen between the sonic and the lidar velocity PDFs. The cause of this shift is presently unknown to us, but could be either due to flow distortion in the sonic or a slightly wrong rotation of the three-dimensional sonic velocity data. This difference is not the subject of the present contribution, but it will be pursued and addressed in a future paper.

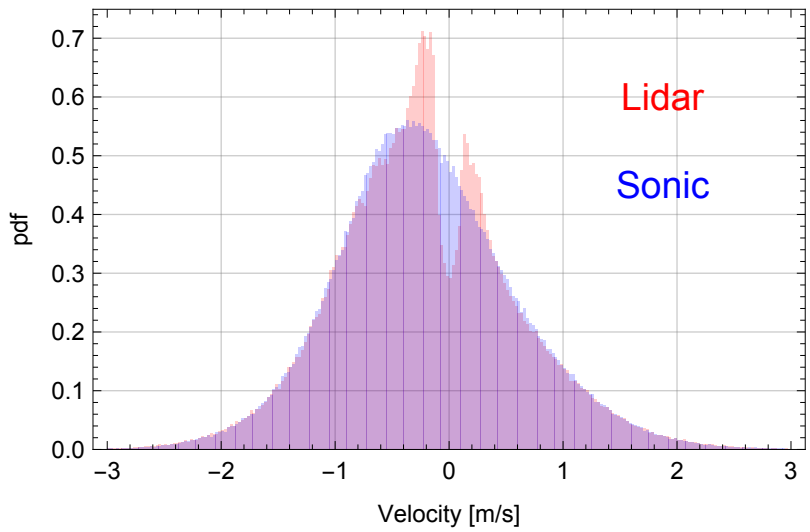

Figure 6: The PDF of the estimated median velocities close to zero, measured by the sonic and ICDL. Blue and red represent the sonic and lidar measurements, respectively. As we can infer from the gap in this figure, the ICDL also suffers from an estimation inaccurcay around zero. This can be attributed to spurious effects (such as DC offset, 1/f noise, filtering, etc.) around the zero frequency. The noise behaviour; however, is significantly improved when compared to the HCDL results presented in Fig. 2.5.

are far less pronounced and consistently follow the sonic, except in a very narrow range around zero velocity.

4 Conclusion

The presented results in this paper verify the relevant performance improvement claims in [15], where a prototype all-fiber CW CDL benefiting from an image-reject opto-electronic front-end was described. The comparison of the results from the presented system and a sonic anemometer clearly indicate a significant improvement in Doppler shift estimation over the AOM-based heterodyne receiver with IF sampling, especially for Doppler shifts close to zero. By discussing some special events, where the Doppler spectrum has energy both at negative and positive frequencies, we have shown that the auto-spectral approach, as opposed to the cross-spectral approach originally suggested in [15], provides a more reliable estimation of the Doppler shifts. As a result, a hybrid approach to spectral estimation is desired where the algorithm primarily employs the cross-spectral approach but switches to an auto-spectral approach (with noise whitening) when small Doppler shifts of the order of ± 1 m/s are detected.

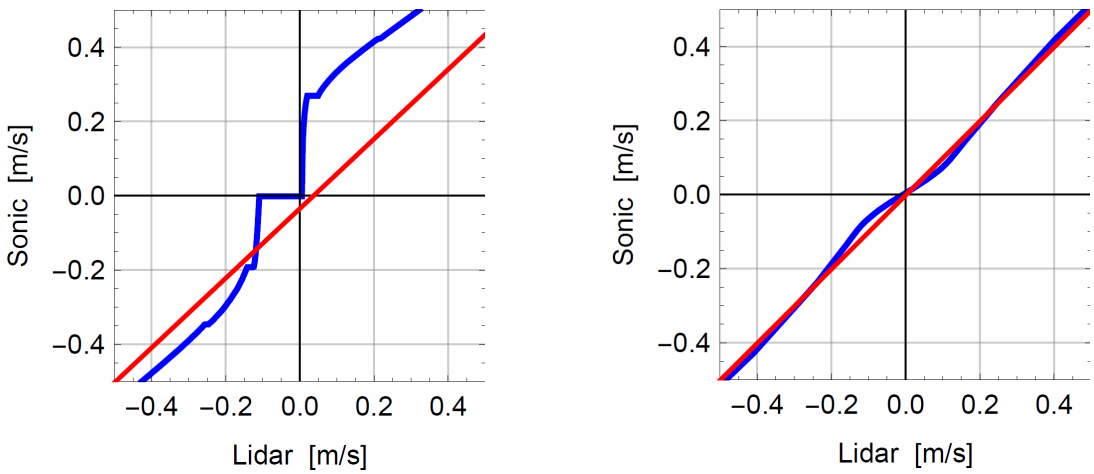

(a) Heterodyne CW CDL (HCDL) (b) Image-reject CW CDL (ICDL)

Figure 7: The estimated median velocities sorted in ascending order and stacked against the sonic (blue). The red line is a linear fit to the blue curve which extends to several m/s in both directions. For an ideal lidar (and sonic) the blue curve would be a one-to-one line.

Acknowledgements

The authors would like to thank Xinzhao Chu from University of Colorado in Boulder and Mikael Sjöholm, Nikolas Angelou, and Karen Enevoldsen from the Technical University of Denmark for their invaluable help. This project is mainly funded by the WindScanner project from the Danish Strategic Research Council (DSF), Danish Agency for Science-Technology and Innovation; Research Infrastructure 2009; Grant No. 2136-08-0022. Additional funds from DSF grant no. 09-067216 (the DTU "Flow Center") are also appreciated. Ingeborg and Leo Dannin Grant for Scientific Research funded the NI computer used in this work.

References

[1] S. Mayor and E. W. Eloranta, "Two-dimensional vector wind fields from volume imaging lidar data," *J. Appl. Meteor.*, vol. 40, pp. 1331–1346, 2001.

[2] Z. Wang, Z. Liu, L. Liu, S. Wu, B. Liu, Z. Li, and X. Chu, "Iodine-filter-based mobile Doppler lidar to make continuous and full-azimuth-scanned wind measurements: Data acquisition and analysis system, data retrieval methods, and error analysis," *Appl. Opt.*, vol. 49, pp. 6960–6978, 2010.

[3] C. J. Grund, R. M. Banta, J. L. George, J. N. Howell, M. J. Post, R. A. Richter, and A. M. Weickmann, "High-resolution doppler lidar for boundary layer and cloud research," *J. Atmos. Oceanic Technol.*, vol. 18, pp. 376–393, 2001.

[4] D. Schlipf, P. W. Cheng, and J. Mann, "Model of the correlation between lidar

systems and wind turbines for lidar-assisted control," *J. Atmos. Oceanic Technol.*, vol. 30, pp. 2233–2240, 2013.

[5] D. A. Smith, M. Harris, A. S. Coffey, T. Mikkelsen, H. E. Jørgensen, J. Mann, and R. Danielian, "Wind lidar evaluation at the danish wind test site in høvsøre," *Wind Energy*, vol. 9, pp. 87–93, 2006.

[6] F. Bingöl, J. Mann, and G. C. Larsen, "Lidar measurements of wake dynamics part I: One dimensional scanning," *Wind Energy*, vol. 13, pp. 51–61, 2010.

[7] Y. L. Pichugina, R. M. Banta, W. A. Brewer, S. P. Sandberg, and R. M. Hardesty, "Doppler lidar–based wind-profile measurement system for offshore wind-energy and other marine boundary layer applications," *J. Appl. Meteor. Climatol.*, vol. 51, pp. 327–349, 2012.

[8] R. T. Menzies and R. M. Hardesty, "Coherent doppler lidar for measurements of wind fields," *Proceedings of the IEEE*, vol. 77, pp. 449–462, 1989.

[9] F. Hall, R. Huffaker, R. Hardesty, M. Jackson, T. Lawrence, M. Post, R. Richter, and B. Weber, "Wind measurement accuracy of the NOAA pulsed infrared Doppler lidar," *Appl. Opt.*, vol. 23, pp. 2503–2506, 1984.

[10] A. Sathe and J. Mann, "A review of turbulence measurements using ground-based wind lidars." *Atmospheric Measurement Techniques*, vol. 6, no. 11, pp. 3147–3167, 2013.

[11] R. Schwiesow and R. Cupp, "Offset local oscillator for CW laser Doppler anemometry," *Appl. opt.*, vol. 20, pp. 579–582, 1981.

[12] K. Shimizu, T. Horiguchi, Y. Koyamada, and T. Kurashima, "Coherent self-heterodyne brillouin otdr for measurement of brillouin frequency shift distribution in optical fibers," *J. Lightwave Techno.*, vol. 12, pp. 730–736, 1994.

[13] B. Razavi, "Design considerations for direct-conversion receivers," *IEEE Trans. Circuits Syst. II: Analog Digit. Signal Process*, vol. 44, pp. 428–435, 1997.

[14] T. Mikkelsen, J. Mann, M. Courtney, and M. Sjöholm, "Lidar-based research and innovation at DTU wind energy–a review," in *J. Phys.: Conf. Ser.*, vol. 524. IOP Publishing, 2014, p. 012007.

[15] C. F. Abari, A. T. Pedersen, and J. Mann, "An all-fiber image-reject homodyne coherent Doppler wind lidar," *Opt. Express*, vol. 22, pp. 25 880–25 894, 2014.

[16] Kylia, single polarization 90^0 optical hybrid COH24. Available at: http://www.kylia.com/, 2015.

[17] A. T. Pedersen, C. F. Abari, J. Mann, and T. Mikkelsen, "Theoretical and experimental signal-to-noise ratio assessment in new direction sensing continuous-wave Doppler lidar," in *J. Phys.: Conf. Ser.*, vol. 524, no. 1. IOP Publishing, 2014, p. 012004.

[18] C. J. Karlsson, F. Å. A. Olsson, D. Letalick, and M. Harris, "All-fiber multifunction continuous-wave coherent laser radar at 1.55 μm for range, speed, vibration, and wind measurements," *Appl. Opt.*, vol. 39, pp. 3716–3726, 2000.

[19] B. Moslehi, "Analysis of optical phase noise in fiber-optic systems employing a laser source with arbitrary coherence time," *J. Lightw. Technol.*, vol. 4, pp. 1334–1351, 1986.

[20] C. M. Sonnenschein and F. A. Horrigan, "Signal-to-noise relationships for coaxial systems that heterodyne backscatter from the atmosphere," *Appl. Opt.*, vol. 10, no. 7, p. 1600–1604, 1971.

[21] N. Angelou, J. Mann, M. Sjöholm, and M. Courtney, "Direct measurement of the spectral transfer function of a laser based anemometer," *Rev. Sci. Instrum.*, vol. 83, p. 033111, 2012.

[22] H. Urey, "Spot size, depth-of-focus, and diffraction ring intensity formulas for truncated gaussian beams," *Appl. Opt.*, vol. 43, pp. 620–625, 2004.

[23] T. W. Horst and S. P. Oncley, "Corrections to inertial-range power spectra measured by CSAT3 and solent sonic anemometers, 1. Path-averaging errors," *Boundary-Layer Meteorology*, vol. 119, no. 2, pp. 375–395, 2006.

[24] N. Angelou, C. F. Abari, J. Mann, T. Mikkelsen, and M. Sjöholm, "Challenges in noise removal from Doppler spectra acquired by a continuous-wave lidar," in *Proc. of the 26th Int. Laser Radar Conf., Porto Heli, Greece, 25-29 June, 2012*, 2012, s5P-01.

[25] M. H. Hayes, *Statistical Digital Signal Processing and Modeling.* John Wiley & Sons, 391-424, 1996.

A re-configurable all-fiber polarization-diversity coherent Doppler wind lidar

Cyrus F. Abari, Xinzhao Chu, Mike Hardesty, and Jakob Mann

Paper IV

Based on: C. F. Abari, X. Chu, M. Hardesty, and J. Mann, "A re-configurable all-fiber polarization-diversity coherent Doppler wind lidar," a manuscript to be submitted to Opt. Express.

Abstract

This paper shows an efficient adaptation of a polarization diversity optical front-end, commonly used in high-speed fiber-optic communications, in a coherent Doppler lidar (CDL). The adopted architecture can be employed in a modified transceiver design for an all-fiber micro pulsed coherent Doppler wind lidar where the performance limits of such systems are pushed beyond the conventionally available wind CDLs. As a result, either a longer measurement range, crucial in clear-air environments with low concentration of aerosols, or a shorter integration time (resulting in a faster scanning) can be achieved. Alternatively, in certain aerosol loading conditions where the presence of non-spherical aerosols is considerable, the system can be re-configured on the fly to analyze the cross-polarization of the backscatter optical signal. The result is the capability to analyze the nature of aerosol particles for the detected range of interest. Due to a full utilization of the backscatter signal, i.e., detection of co-pol and cross-pol components, the signal-to-noise-ratio (SNR) as well as detection range is improved in this configuration. This system employs robust and compact all-fiber components which are cost effective and widely available as off-the-shelf components.

1 Introduction

Optical remote sensing of atmospheric parameters has been actively sought after and developed over the past few decades to provide better tools for the characterization and prediction of atmospheric and climatic phenomena. In renewable energy industry, e.g., wind energy, remote measurement of atmospheric parameters, especially wind, is crucial for the maximization of energy production. One of the primary and highly efficient remote sensing techniques is light detection and ranging (lidar), an active measurement technique. In such instruments a light source is employed to illuminate a target of interest, such as molecules or aerosol particles. The backscatter light from the target is collected and analyzed to measure and quantify the parameters of interest.

Some of the first reported examples of lidars were based on a rudimentary search light technique [1] to measure the air density profiles in the upper atmosphere. In these systems a continuous transmission of light would illuminate the targets along the beam transmission path. A scanning receiving telescope would collect the backscatter light from the range/altitude of interest. Later, modulation of the searchlight through a rotating mechanical shutter was suggested by Johnson [2] resulting in measurements at longer ranges. Ever since, application of light in active instruments to measure various atmospheric parameters has grown dramatically and the field has expanded. After the invention of laser, a highly coherent light source became available which conceived new measurements and pushed the boundaries of the existing ones. For instance, resonance lidars have been used to measure the temperature densities of Fe and Na in the upper atmosphere [3, 4]. Rotational Raman lidars [5] were developed to carry out remote measurements of temperature and high spectral resolution lidars became available to provide measurements of temperature and atmospheric aerosols [6].

One of the capabilities of lidars is to measure the wind speed. For instance, resonance fluorescence lidars can be employed for the remote sensing of wind in the mesopause [4, 7].

Among the available wind lidars coherent Doppler lidars (CDL) became widely popular for the measurement of wind in the troposphere [8]. CDLs measure the radial velocity of the wind by processing the wind-induced Doppler shift. The CO_2 laser was among the first adopted lasers for coherent detection of wind [9]. Due to advances in diode-laser pumping, solid-state CDLs (operating in 0.3-3 μm) became popular [9]. An eye-safe CDL operating at 2.1 μm using solid-state lasers was first reported by Henderson, et al. [10].

Recently all-fiber CDLs have become widely adopted for remote sensing of wind both as ground-base and airborne systems [11–13]. These systems are compact, robust, and fairly cost effective, thanks to high-speed optical communication which has been the driving force behind rapid technology improvements in fiber optic components and lasers. For instance, an airborne all-fiber continuous-wave (CW) CDL has been reported in [13] for in-flight measurement of wind and turbulence. WINDCUBE [14] from Leosphere, ZephIR [15] from ZephIR, and HALO photonics lidars [16] are commercial examples of 1.5 μm all-fiber coherent Doppler wind lidars. A modified ZephIR lidar, developed as a research instrument in collaboration with the Technical University of Denmark, is the Windscanner [17]. Compared to the commercially available ZephIR, this CW CDL has the additional capability to detect the direction of the radial velocity of wind. Recently, the systems have been retrofitted with an improved optical front-end, i.e., an image-reject homodyne optical front-end [18], to improve the measurement performance.

CDLs share many principles with coherent optical communications. The majority of the available all-fiber CDLs benefits from the extensively available fiber-optic components, originally developed for fiber-optic communications. However, there seems to be a huge potential for further improvement of all-fiber CDLs if the full extend of fiber-optic communication technology, when relevant, is exploited. For instance, it was recently shown [18] that an all-fiber image-reject homodyne optical front-end, originally developed for coherent detection in optical communication, can be successfully adopted in a CW CDL. The lab results from the prototype, as the first reported all-fiber image-reject homodyne CW CDL, show significant improvement in terms of the detection velocity range as well as noise behavior. The detection improvements were significant for small values of wind speed, near-zero velocities. The improved performance results of this system were further verified through an atmospheric campaign [19]. This front-architecture can be equally adopted in a long-range pulsed CDL.

In this paper, we show that a polarization diversity image-reject homodyne optical front-end, commonly employed in high-speed fiber-optic communications [20], can be adopted in a re-configurable pulsed CDL. The proposed lidar in this paper has the capability to improve the performance of the contemporary all-fiber CDLs multi-fold. As we will show in Sec. 4, the re-configurable transceiver can operate either in a high-power mode, suitable in atmospheric conditions with weak aerosol loading (resulting in weak backscatter signals) or a cross-polarization detection mode. When in high-power mode (known as mode II, see Sec. 4) two erbium doped fiber optic amplifiers (EDFA) can operate in concert to double the output power of the lidar. To remove the possibility of interference between the transmit/receive signals, the two EDFAs are isolated by their orthogonal state of polarization. In the alternative mode (mode I), the system has the capability to continuously monitor the depolarization of backscatter light from non-spherical particles such as ash plumes, ice crystals, clouds, etc. To our knowledge,

this is the first all-fiber CDL capable of continuous monitoring of signal depolarization from aerosol particles.

The material in this paper is presented in a few sections. In Sec. 2 a mathematical model for the expected receive signal power for elastic backscattering from a diffused atmospheric target is provided. Furthermore, we present the requirements for the realization of a coherent Doppler lidar system and present an example of a typical all-fiber CDL architecture. Sec. 3 introduces the baseband signal modeling adopted in this paper for the simulation purposes. In Sec. 4, the proposed architecture in this paper is analyzed and advantages and disadvantages are discussed. In Sec. 5, we show the results of our numerical simulation for the two main configurations (modes) of the proposed system in this paper. Eventually, the paper is finalized with the conclusion section where suggestions for future work are also presented.

2 Coherent Doppler lidar

CDLs rely on the processing of elastic backscattering from a target [1] to extract the information of interest such as Doppler shift. In atmospheric science the target has a diffuse nature, i.e., the mean free path between the constituents is much larger than optical wavelength of the transmitted laser beam [21]. For a maximum atmospheric penetration, for lidars relying on elastic backscattering, the optical wavelength should be selected such that it's absorption by the atmospheric constituents such as water vapor and CO_2 is minimal. Besides, eye-safety issues associated with laser transmission place harsh requirements on the transmit optical power (for a given wavelength). 1.5, 2.1, and 10 μm wavelengths (see [9, 10, 14, 15]) have been reported for successful implementation of eye-safe CDLs attaining maximum atmospheric transmission. Despite a stronger backscatter cross-section the sub-micron wavelengths are not suitable for adoption in a CDL; high-quality diffraction-limited optics, an essential part of a CDL, is difficult to achieve for submicron wavelength while eye-safety poses additional constraints. Wavelengths above 1.4 μm are generally considered eye-safe [9]. This definition is within well-defined standards and its analysis is beyond the scope of this paper.

In an elastic-backscatter lidar the expected backscatter power can be expressed through the modified lidar equation [22]

$$E_r = \eta E_t \beta\left(\lambda, z\right) T^2\left(\lambda, z\right) G(z) \frac{A}{z^2} \Delta z, \tag{2.1}$$

where η is the lidar efficiency, β is the backscatter coefficient, T is the one-way atmospheric transmission, z is the mean distance to the measurement range, $G(z)$ is the geometric parameter for the light collection capability of the lidar at range z, A is the receiving optical antenna area, and Δz is the depth of the illuminated region. Furthermore, E_r and E_t are the receive and transmit optical energies, respectively.

CDLs belong to a class of lidars known as diffraction-limited lidars. In diffraction-limited lidars the amount of background light collection is minimized by restricting the

[1] In elastic backcattering there is no transfer of energy between the light and matter. In other words, the optical wavelength of the backscatter light remains similar to the transmit light.

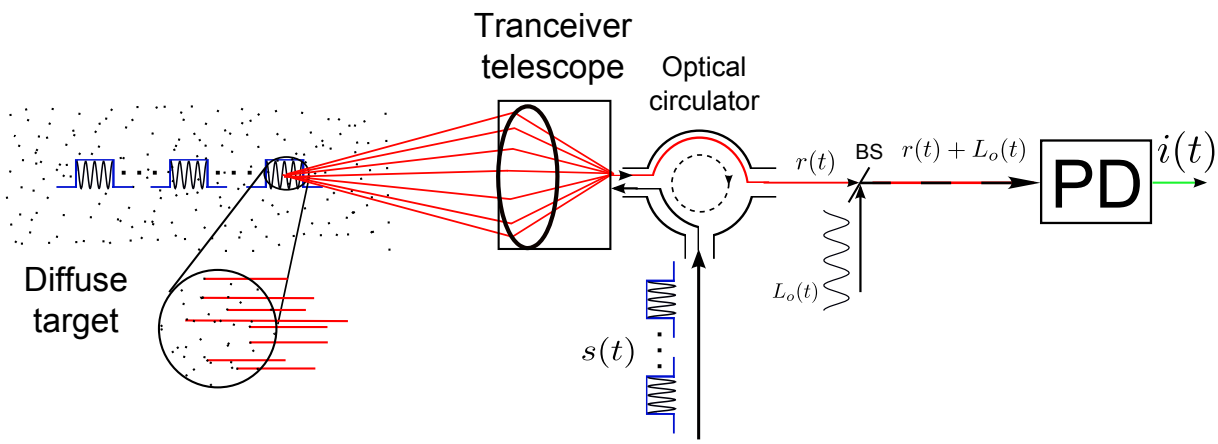

Figure 1: A simplified illustration of a pulsed CDL. The transmitted, $s(t)$, and the local oscillator, $L_o(t)$, signals are spatially and temporary coherent; they are usually (but not necessarily) derived from a single laser known as master oscillator.

field of view, i.e., the number of spatial modes seen by the lidar [23]. In CDLs defraction-limited operation is also key to the existence of spatial coherence between the local oscillator and the collected backscatter signal. It can be shown [23] that in mono-static diffraction-limited lidars the collected signal power is maximized if the transmitter and receiver are matched to the same spatial mode. In other words, the transmit and receive path should overlap in such systems, hence a coaxial system. Meanwhile, since in CDLs the phases of the return signals are compared against a reference signal the detected signal can suffer from a small-scale Rayleigh fading (also known as speckle noise) when backscatter is from a diffuse target (see [24] for the properties of speckle).

Equation (2.1) can be rewritten for a CDL to accommodate the transmit/receive geometry as well as backscatter from a diffuse target, such as atmospheric aerosols. Thus,

$$E_r = \eta E_t \beta(\lambda, z) T^2(\lambda, z) \frac{A_{eff}(z)}{z^2} \frac{c\tau}{2}, \tag{2.2}$$

where $\frac{\tau}{2}$ is the range gate in time, c is the speed of light in the atmosphere, and $A_{eff}(z)$ is the effective telescope area. Moreover, (2.2) can be expressed as,

$$p_r = \eta E_t \beta(\lambda, z) T^2(\lambda, z) \frac{c A_{eff}(z)}{2z^2}, \tag{2.3}$$

where p_r is the average backscatter signal power over τ time span. Following [21] it can be shown that the effective telescope area for a turbulence-free optical path is

$$A_{eff}(z) = \frac{\pi D^2}{4} \left[1 + \left(\frac{\pi D^2}{4\lambda z} \right)^2 \left(1 - \frac{z}{F} \right)^2 \right]^{-1}, \tag{2.4}$$

where D is the telescope diameter and, in the event of a focused light, F is the focus distance. Furthermore, for a collimated beam ($F \to \infty$)

$$A_{eff}(z) = \frac{\pi D^2}{4} \left[1 + \left(\frac{\pi D^2}{4\lambda z} \right)^2 \right]^{-1}. \tag{2.5}$$

(2.4) is the effective telescope area in the presence of target speckle only. However, another important phenomenon in the atmosphere, especially for long optical paths, affects the spatial coherence of the wave-front associated with the backscatter. In the presence of atmospheric turbulence the refractive index variations over the optical path deteriorates the speckle. The effect of the atmospheric turbulence on the optical path has been well investigated [23, 25–28]. As a result, (2.4) can be modified to reflect the effect of turbulence such that

$$A_{eff}(z) = \frac{\pi D^2}{4}\left[1 + \left(\frac{\pi D^2}{4\lambda z}\right)^2 \left(1 - \frac{z}{F}\right)^2 + \frac{D^2}{2\rho_0^2}\right]^{-1}, \tag{2.6}$$

where ρ_0 is the turbulence parameter (also known as "the efficiency saturation dimension" [29]) and given by

$$\rho_0 = \left[1.45\left(\frac{2\pi}{\lambda}\right)^2 \int_0^z C_n^2(z')\left(1 - \frac{z'}{z}\right)^{\frac{5}{3}} dz'\right]^{-\frac{3}{5}}, \tag{2.7}$$

where C_n^2 is known as the refractive index structure function. Typical diurnal conditions of strong and moderate turbulence can be represented by $C_n^2 = 10^{-12}$ and $C_n^2 = 1^{-14}$ [28], respectively.

It can be shown that for a constant refractive turbulence level, C_n^2, (2.8) reduces to

$$\rho_0 = \left[\frac{4.35}{8}\left(\frac{2\pi}{\lambda}\right)^2 C_n^2 z\right]^{-\frac{3}{5}}. \tag{2.8}$$

The speckle effect places an upper limit on the maximum antenna area, beyond which no tangible signal-to-noise ratio (SNR) improvement is observed [27]. For a relatively moderate atmospheric turbulence the turbulence induced speckle is dominant. Moreover, since the target speckle correlation time is on the order of a few μs its effect can be reduced through pulse averaging. The same is not true for the atmospheric turbulence as its correlation time is on the order of ms. As a result, a design antenna diameter can be safely selected based on the atmospheric turbulence induced speckle. It has been shown [27] that in an efficient design ρ_0 is selected as the optimum size of the receiving optics for a given range and atmospheric turbulence condition.

Fig. 1 shows a simplified example of a CDL. In this system, an optical circulator (see Fig. 2) isolates the transmit and receive signals. In this system, the collected backscatter signal, $r(t)$, is mixed with a reference signal known as the local oscillator (LO), $L_O(t)$. The mixed signal is impinged on the surface of a photo detector. Coherent detection relies on spatial and temporal matching of the LO and the receive signal. The two signals should sustain a matched polarization state for a maximum detection efficiency. As a result, for an LO signal with an optical power p_{lo} and average return signal power p_r, it can be shown that the power of the detected Doppler signal, $i(t)$, at the output of the photodetector is [2]

$$p_i = \mathbb{E}\left\{|i(t)|^2\right\} = 2p_{lo}p_r\cos^2(\theta), \tag{2.9}$$

[2] We have assumed a photodetector responsivity (detection efficiency) of unity.

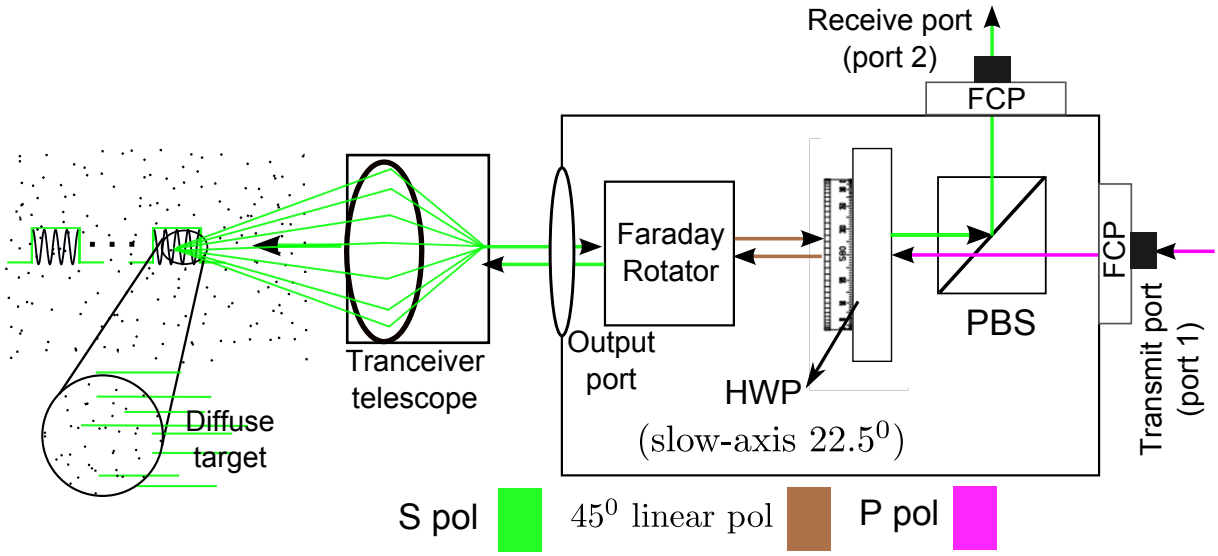

Figure 2: A simple single polarization optical circulator. Isolation between port 1 and 2 is provided by manipulating the light polarization through the PBS, half-wave plate (HWP), and Faraday rotator, as shown. The fiber coupled ports (FCP) connect the optical circulator to the transmit and receiver fibers. For more information on optical circulators please see [30, 31].

where θ is the angle between the polarization states of LO and backscatter signals and $\mathbb{E}\{\cdot\}$ denotes the ensemble average operation. Please note that we have dropped the z dependence of p_r in (2.9) for simplicity.

For an optimum performance the LO power is selected so that the detector operates in a shot-noise limited operating mode. The shot-noise power, considered the dominant noise source, can be expressed as

$$p_{\eta_{sn}} = 2\frac{hc}{\lambda}p_{lo}B, \tag{2.10}$$

where B is the bandwidth (BW) of the photodetector, h is the Planck constant, and c is the speed of light in the medium. Following (2.9) and (2.10), the average SNR ($\bar{\gamma}$), for a perfect match between the polarization states of the reference and backscatter signals, can be defined as

$$\bar{\gamma} = \mathbb{E}\{\gamma\} = \frac{p_i}{p_{\eta_{sn}}} = \frac{p_r\lambda}{hcB}. \tag{2.11}$$

Equation (2.12) shows the high sensitivity of coherent detection; this system reaches a SNR= 0 per unit BW for each single photon.

The ensemble average in (2.11) is a reminder for the random nature of the backscatter power resulting from the speckle. The instantaneous SNR, γ, associated with the return from one single pulse has an exponential distribution and can be expressed as [32],

$$p_\gamma(\gamma) = \frac{1}{\bar{\gamma}}\exp\left(-\frac{1}{\bar{\gamma}}\gamma\right), \tag{2.12}$$

where $p_\gamma(\gamma)$ is the probability distribution function (PDF) of γ.

3 All-fiber single-polarization CDL and baseband signal modeling

Before recent advances in fiber-optic technology CDLs relied on bulky open-space optics for the generation, transmission, and manipulation of the optical signals. CO_2 and diode-pumped Tm:Lu:YAG laser CDLs [9] are examples of such systems. With the revolutionary advances in fiber-optic technology a wide variety of fiber-optic components became available. Examples of such components are fiber-optic lasers, amplifiers, beam couplers, etc. These components are compact, robust, and cost-effective, when compared to their open-space counterparts. Due to their minimum transmission loss at 1.5 μm, optical-fibers have become the dominant means of optical information transmission at 1.5 μm.

1.5 μm wavelength also happens to belong to an optical spectral region with a maximum atmospheric transmission. As a result, all-fiber lidars have become the dominant players in the CDL market, e.g., see [14, 16] for instances of commercially available all-fiber long-range (pulsed) CDLs. In such systems fiber lasers (or fiber-coupled semiconductor lasers) with a linewidth better than 5 kHz are available. A narrow linewidth on this scale allows the coherent detection over significantly long measurement ranges, with minimal signal degradation arising from the loss of temporal coherence between the transmit and reference signals. Besides, the availability of EDFAs has provided a linear low-noise alternative for optical signal amplification in these systems. Since the majority of EDFAs exhibit μJ optical powers in the pulsed amplification mode, pulsed all-fiber CDLs are also known as micro-pulsed CDLs. The pulse repetition rate (PRR), however, is relatively high in EDFAs (on the order of several kHz) making the average output power comparable with some of the more high-energy pulsed open-space technologies such as the ones discussed in [9].

Fig. 3 shows an examples of an all-fiber CDL in master oscillator power amplifier (MOPA) configuration. In this figure, the master optical source is a narrow linewidth fiber coupled CW laser with an average optical output of tens of mW. The pulse shaper (modulator) can be a mechanical chopper, an acousto-optic modulator (AOM), or an electro-optic modulator (EOM). The signal train at the output of the modulator is fed into an EDFA for amplification. The result passes through the optical circulator and after proper beam expansion and focusing (or collimation), is transmitted through the atmosphere. As the pulse travels through the atmosphere it illuminates the atmospheric constituents, e.g., aerosols. The backscatter from the particles is collected by the telescope and passed through the circulator until it reaches the balanced mixer. A detailed description of a balanced mixer, employed in a continuous wave (CW) CDL, has been provided in [18]. The LO and receive signal $r(t)$ are mixed by a 50% fiber-optic coupler and impinged on a pair of balanced photo detectors. The resultant current is further amplified and conditioned for digitization. The Doppler spectrum of the return signal is processed in the digital domain to extract the parameters of interest, e.g., the wind speed.

The pulse modulator in the system shown in Fig. 3 is usually an AOM. The main benefit of AOM in such systems is a simultaneous modulation of amplitude and frequency while providing a high extinction ratio between on and off states. As a result of a frequency

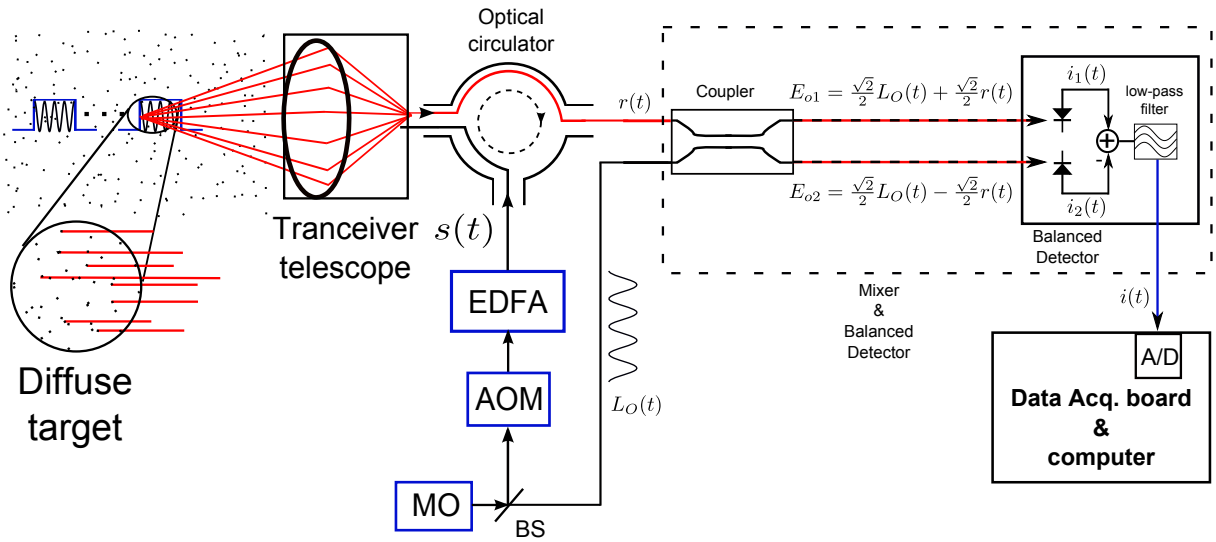

Figure 3: A single-polarization heterodyne pulsed CDL with IF sampling. The AOM is responsible for chopping the signal received from the MO and generating the required optical pulses while shifting the transmit signal frequency to an IF offset. The balanced mixer and detector utilized the full power of the collected backscatter signal while removing the DC and any common mode components from the L_O and $r(t)$ signals [18].

offset at the intermediate frequency (IF) the sign of the detected Doppler shifts can be discriminated. This is at the cost of a reduced BW efficiency associated with the photodetectors and the analogue-to-digital converters (A/D). It has been shown in [18] that by employing an all-fiber image-reject homodyne optical front-end, made originally available to the high-speed optical-communication industry, the signals can be translated into baseband where the requirement for an IF offset is eliminated. Although the optical front-end in [18] is adopted for a CW CDL, it can be easily employed in a pulsed CDL. Fig. 4 shows the schematic of a single-polarization all-fiber image-reject homodyne long-range (pulsed) CDL.

To provide a better understanding of the detected signals at the output of the photo detector associated with the system in Fig. 4, the complex baseband mathematical signal model introduced by Rye [33] can be readily adopted in this system. If the compressed transmit pulse associated with the system in Fig. 4 is $s(t)$, then the Doppler-free baseband signal can be expressed as

$$i(t) = k \int_0^{+\infty} s(t - t') \sum_{l=1}^{N} \alpha_l \delta\left(t' - t_l\right) dt', \tag{3.1}$$

where α_l is a complex valued random variable (RV) associated with the lth particle with independent real and imaginary components having a Gaussian distribution. Furthermore, N is the number of scattering particles and k is a constant scaling factor representing any optical attenuation, transceiver efficiency, photodetector responsivity, etc., not shown in (3.1).

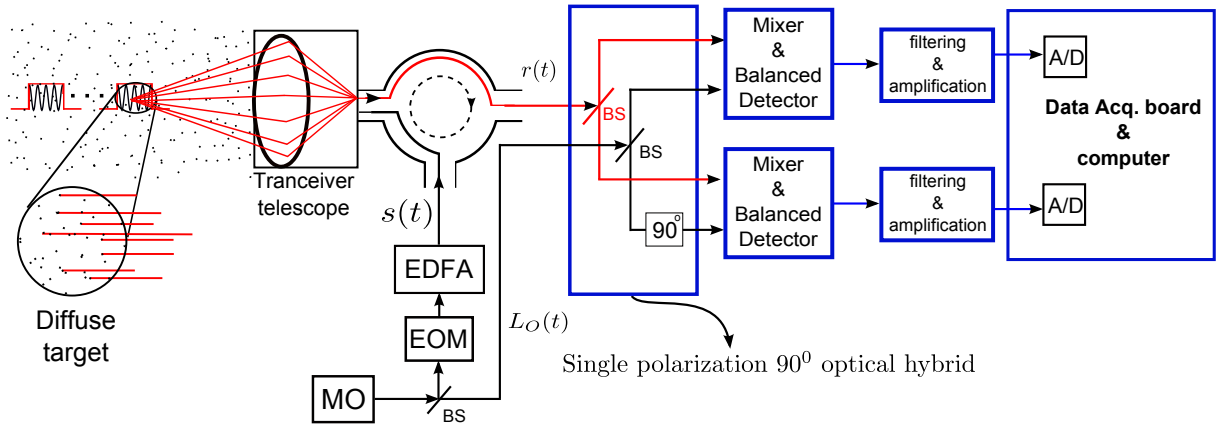

Figure 4: A single polarization image-reject homodyne pulsed CDL. In this system the pulse generator can be an EOM which does not introduce any frequency offset in the transmit signal. The image-reject homodyne receiver translates the Doppler signal into baseband for further processing. The image-reject homodyne receiver, also known as direct-conversion receiver, eliminates the need for an IF offset (enabling Doppler signal sign detection).

Equation (3.1) reflects the diffuse nature of the target. The above equation can be also expressed as a convolution such that

$$i(t) = s(t) \otimes h(t), \tag{3.2}$$

where $\otimes$ is the convolution operator and $h(t) = k \sum_{l=1}^{N} \alpha_l \delta\left(t - t_l\right)$ can be thought of the channel response function, a terminology commonly used in wireless communications.

(3.1) does not reflect the Doppler effect and, as a result, needs to be modified so that the motion of the particles is included. Thus [33],

$$i(t) = k \iint_{0}^{+\infty} s(t-t') \exp\left[j2\pi f'(t-t')\right] \sum_{l=1}^{N} \alpha_l \delta(t'-t_l)\delta(f'-f_l) dt' df', \tag{3.3}$$

where $s(t-t') \exp\left[j2\pi f'(t-t')\right]$ is the frequency-shifted pulsed waveform and f_l is the frequency shift associated with the lth particle. (3.3) is associated with the detected signal over the entire measurement range. Considering the fact that the pulse illuminates different sets of particles as it propagates through the atmosphere the return signal decorrelates. As a result, a shorter sample volume where a certain spatial correlation between the scattering particles exists needs to be used for the Doppler shift estimation. We can expect the range gate to completely decorrelate once the pulse has traveled a distance equivalent to the pulse length.

In light of the above discussion (3.3) needs to be truncated for each range gate of interest. Range gating also allows the estimation of the Doppler spectra for specific ranges over the maximum measurement range. Thus, if $w\left(t - t_0\right)$ is the window function with a width equivalent to the length of the range gate (t_0 is the center of the range gate), then

$$i_T(t) = w\left(t - t_0\right) i(t). \tag{3.4}$$

Following [33] and after some mathematical manipulations and simplifications it can be shown that

$$P_{i_T}(f) = \mathbb{E}\left\{|I_T(f)|^2\right\} = k^2 \sum_{l=1}^{N_0} \mathbb{E}\{|\alpha_l|^2\} \left[|W(f)|^2 \otimes |G(f)|^2 \otimes \mathbb{E}\{P_{T_0}(f)\}\right], \tag{3.5}$$

where $P_{i_T}(f)$ is the power spectral density (PSD) of $i_T(t)$, while $I_T(f)$, $W(f)$, and $G(f)$ are the continuous time Fourier transforms (CTFT) of the truncated signal, window, and pulse, respectively. Furthermore,

$$P_{T_0}(f) = \sum_{l=1}^{N_0} \delta\left(f - f_l\right) \tag{3.6}$$

is the Doppler spread function associated with the particles belonging to the range gate centered at t_0. It is evident from (3.5) that the Doppler spectrum of the detected signal is the convolution of the pulse and window function PSDs as well the Doppler spectrum associated with the particles in the sampling volume.

4 All-fiber polarization diversity image-reject coherent Doppler lidar

As seen from (2.9) the detection efficiency is maximized if the LO and backscatter signals retain the same polarization state. As a result, in the majority of all-fiber CDLs, polarization maintaining (PM) fibers are used for the transmission and manipulation of light. The only exception is a CW CDL where the LO is taken from the end facet of delivery fiber by Fresnel reflection [11]. As a result, the LO and backscatter signal follow the same path in the system and experience the same polarization variations. In such a system single mode (SM) fibers can be conveniently used in place of PM fibers. A detailed description of such a system architecture can be found in [11, 18]. Due to system design requirements, where the LO and backscatter signal (after collection by the telescope) experience different paths before mixing at the receiver, the long-range (pulsed) CDLs need to employ PM fibers to guarantee maximum overlap between the polarization states of the receive and LO signals.

In this paper, we suggest a new all-fiber optical front-architecture where an image-reject homodyne receiver such as the one in [18] is used for the translation of Doppler information into the baseband. Furthermore, we suggest a polarization diversity optical front-end, conventionally used in high-speed fiber-optic communications [20], to take advantage of the additional degree of freedom provided with an extra polarization state of light. In other words, we suggest the system operate on the basis of two orthogonal polarization states. The orthogonality of the polarization states helps us separate the two signals without any noticeable interference. The system is designed such that it is capable of detecting the depolarized signal component, if any. Backscatter light depolarization is a common phenomenon when probing aerosols with non-spherical shapes; for instance, (ash) clouds and ice crystals are examples of natural atmospheric phenomena where non-spherical particles may constitute a significant part of the aerosols. In the event of clear

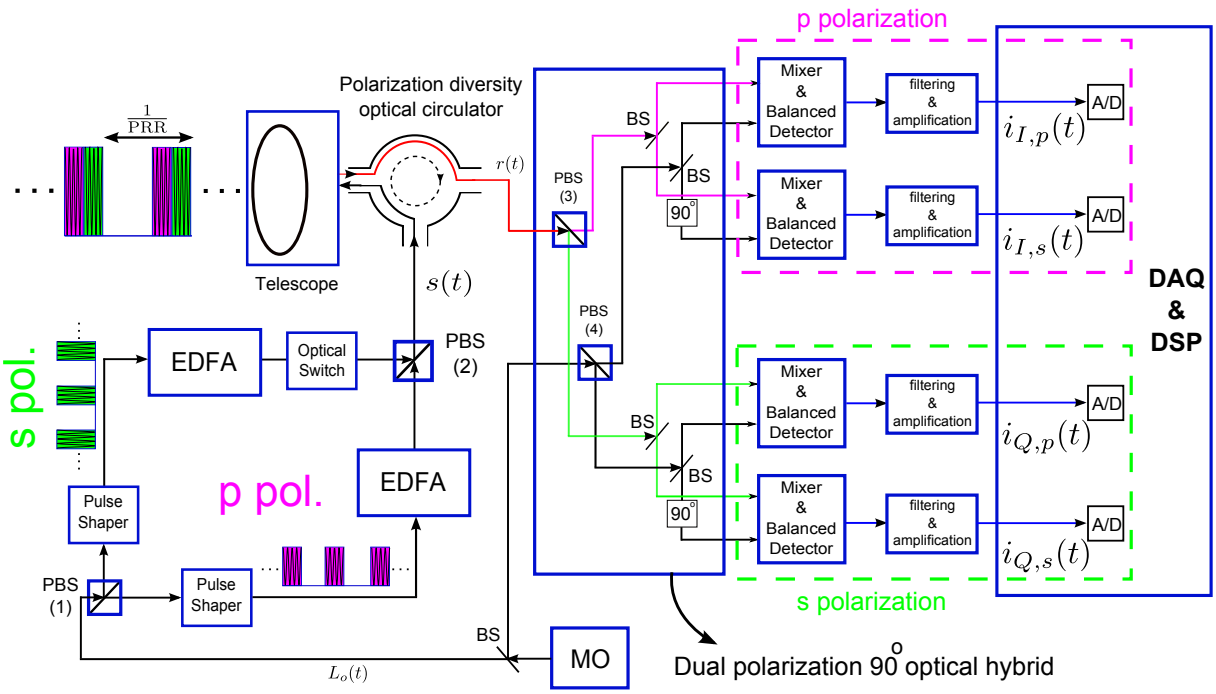

Figure 5: The re-configurable polarization-diversity image-reject homodyne pulsed CDL presented in this paper. The dual-polarization 90^0 optical hybrid [20] is responsible for splitting the receive signal into its orthogonal polarization components while providing the necessary phase shifts necessary for the translation of the Doppler signals into baseband.

air atmosphere, with relatively low amount of light depolarization, the system can double its average output power by interleaving the transmit pulsed with orthogonal polarization states while maintaining its range.

Fig. 5 shows the schematic of such a system. As we can see an MO is used to generate a narrow linewidth laser. The optical power is usually in the range of 10s of mW. For the system configuration in this system the state of polarization of the laser light at the output of the MO can be 45^0. A beam splitter (BS) allows a small amount of the power to be diverted as LO signal. The signal at the output of the BS, right after MO, is fed into the first polarizing beam splitter (PBS). The PBS receives the laser (having a polarization of 45^0) and divides it in half, where two orthogonal polarization states, i.e., p and s polarization states are separated at the output legs. The optical switch on the p polarization leg allows the system to operate in two configurations. When the switch is on, the system operates with maximum output power. In other words, it allows two separate pulse trains to be transmitted simultaneously without interfering with each other; the two pulse trains are isolated in polarization. We call this operating mode II. If the switch is off, i.e., mode I, then the system operates with only one polarization, p polarization. This operation mode is suitable in measurement in atmospheric conditions where non-spherical particles are expected. For instance, if the laser pulse propagates through clouds a certain degree of depolarization can be observed [34].

4.1 Mode I

In mode I, the system operates with only one EDFA. The EDFAs are usually average power limited. There is only so much power an EDFA (employing single mode fibers) can generate. Due to a limited single mode fiber core size, such EDFAs have a limited output power. Since the EDFA's are average-power limited, one may increase the pulse energy by decreasing the PRR; most EDFAs operate within certain PRR and pulse energy limits before non-linearities and other unwanted spurious effects kick in. Besides, increasing pulse energy at the cost of PRR reduces the effective number of pulse averaging at the receiver for a given integration time. A detailed discussion of EDFAs and their limitation is well beyond the scope of this report.

Since the optical switch is turned off (when operating in Mode I), only the pulses from the p polarization (co-pol) leg are transmitted through the polarization diversity optical circulator and eventually the telescope. The optical circulator essentially isolates the transmit and receiver signals and should ideally eliminate the cross-talk between its three ports. Due to non-ideal behavior of the components used to build the optical circulator, there is always a certain degree of cross-talk between the ports. Imperfections in beam alignment can also be confounding. The polarization diversity optical circulator is more complex than the single-polarization optical circulator. The schematic of a polarization diversity optical circulator is discussed in Appendix A.

As soon as the pulse starts propagating through the atmosphere the backscatter signal is collected and continuously recorded (the signal associated with the range of interest is isolated through range gating, a processing done later at the receiver) and passed to PBS 3. At the output of PBS 3 the signal is divided into two components with orthogonal polarization states, i.e., p (co-pol) and s (cross-pol). If atmospheric depolarization is negligible, then the backscatter signal retains its polarization state and signal is present on only one leg at the output of PBS 3. The polarization state of the received light depends on the optical circulator design and technology. If the optical circulators shown in this paper are employed in the system the return signal will exhibit the cross-pol when compared to the originally transmitted signal. In this specific case, where p-pol is transmitted, s-pol (identified with the green colored signal paths in Fig. 4) is received at the input of PBS 3. If there is any tangible backscatter depolarization, the cross-polarization (in this case p polarization) will be detected by the upper detection chain (pink optical path) while the s polarization (green optical path) is detected by the lower detection chain in Fig. 4. The ratio between the two detected signals can provide some information about the nature of the aerosol particles. As a result, one benefit from the additional information provided by this CDL to characterize the aerosols associated with different range gates.

The possibility of detecting the depolarized signals, as opposed to dumping them (a method conventionally used in single-polarization CDLs), also improves the SNR in this system. The system effectively collects all the available backscatter signal (including the depolarized signal) within its filed of view for detection at the photodetectors. In such a system, a maximum ratio combining (MRC) technique (e.g., see [35]) commonly used in wireless communications can be used to maximize the SNR for any given signal strength on the two polarization states. This system is also able to improve the SNR degradation

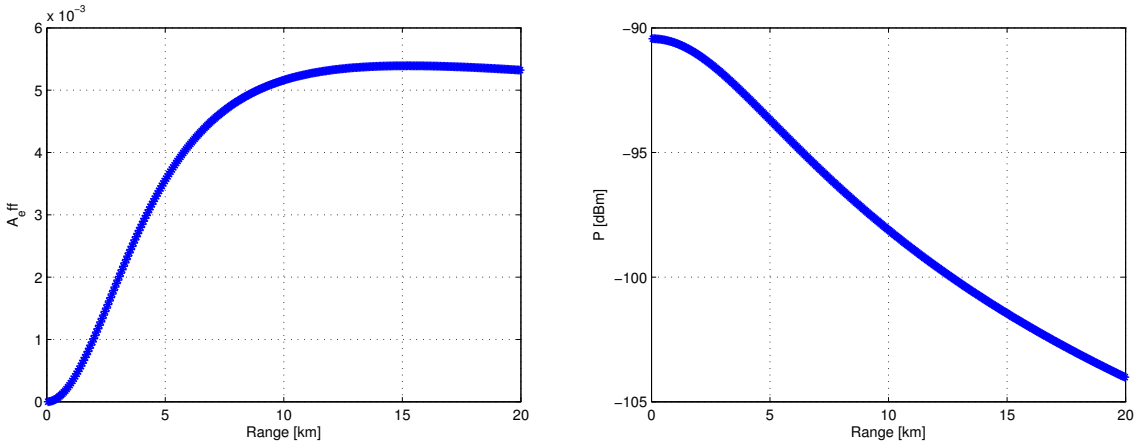

(a) The effective telescope area

(b) The Mie backscatter signal power

Figure 6: The effective telescope area and expected return signal power associated with one channel for the parameters given in table 1.

seen in single-polarization CDLs from non-ideal optical components and surfaces (such as mirrors) that contribute to a certain amount of signal depolarization. Moreover, it is expected that the two backscatter light components (with orthogonal polarization states) experience different speckle patterns. This can be expected due to the non-spherical nature of the particles. As a result, the SNR is further improved due to an additional degree of speckle diversity in this configuration. In a single-polarization pulsed lidar pulse averaging for each range gate helps to improve the SNR. This is due to the physical nature of the (target) speckle; target speckle has a correlation time of a few μs. As much as a 2-fold speckle diversity improvement (in the event of signal depolarization) can be expected in this configuration.

4.2 Mode II

This mode is particularly beneficial in measurement scenarios where the aerosol concentration is low in the measurement volume; a requirement for this mode is that the aerosols are mostly spherical so the amount of backscatter light depolarization is minimal. In the event of backscatter signal depolarization, the cross-pol component of the backscatter signal associated with one pulse train will interfere with the backscatter from the other, resulting in range ambiguity at the receiver. As a result, this mode can be safely used after an initial scan of the measurement volumes (in Mode I) has been performed. If no significant depolarization is observed the system can be switched into Mode II. To take into account the variations in atmospheric conditions and aerosol types a certain measurement and scanning scheme can be developed where the system switches between Mode I and II periodically to account for possible depolarization at certain range gates during the measurement time. Another main merit of this system is improving the measurement speed by reducing the required integration time for a given measurement accuracy. This is especially useful in scanning CDLs.

If the optical switch is on, then the two pulse trains are interleaved at the output

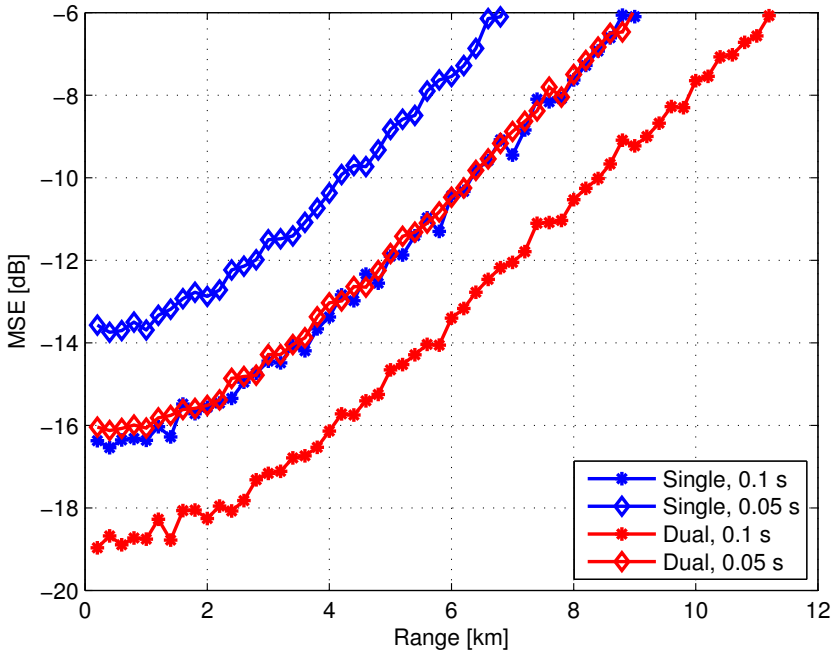

Figure 7: Mean square error (MSE) versus range. Single channel represents the MSE for one polarization state. Dual channel represents the MSE when the data from both polarization is utilized. The values are estimated for two different integration times, i.e., 0.1 and 0.05 s.

of PBS 3. One of the design parameters in this system is the interleaving pattern. By controlling the timing (delay) between the co-pol and cross-pol pulses, generated by the pulse modulator, one can decide where the pulses are placed relative to each other. For instance, the interleaved pulses can be placed in equal distances from each other. Although this seems as an obvious choice for the given pulse trains, it may cause interference with the collected backscatter signal at the optical circulator. This is mainly attributed to the possible leakage and non-ideal behavior of the optical circulator; due to a cross-talk in the optical circulator as well as back reflections from the telescope, high energy optical pulses will leak back to the photo detectors (on both polarization legs) while leaving the telescope. This is one of the main reasons why the pulsed lidars are incapable of measuring the short ranges immediately after the output of the telescope. This range is proportional to the pulse length; the longer the pulse the longer the blind detection range, i.e., the blind spot.

To address the above mentioned issue, we suggest placing the interleaved pulses immediately next to each other. As a result, we prevent detector saturation during the measurement of a specific range which coincides with the timing of the alternate polarized pulse transmission. The downside is that the blind spot size doubles. This system mode, however, is mostly used for the measurement of longer ranges and the deterioration of the short-range measurement capability (blind zone) is not expected to be significant.

The added benefit of placing the alternate polarized pulses next to each other is maximizing the correlation between the backscatter signal associated with each polarization state. Atmospheric correlation time is on the order of a few μs. Any backscatter signal for a specific range gate decorrelates between the transmission of consequent pulses [33] (in a single-polarization CDL) probing the measurement range. To our knowledge, the pulse repetition rate at its highest (available in all-fiber CDLs) is on the order of 10s of kHz. Thus the pulse separation in time is on the order of ms. As a result, no correlation between the backscatter signals associated with two consecutive pulses is expected. In our proposed interleaved pulse scheme, the two pulses with orthogonal polarization states, travel together, separated only by the polarization and a time interval equivalent to the pulse length (typical pulse length in such systems is on the order of 200-400 ns). Thus, the backscatter signals associated with a pair of traveling pulses for each measurement range are expected to be correlated.

5 Simulation results

To characterize the performance of the system presented in this paper, We have carried out a Monte-Carlo simulation of the lidar system in Matlab. The simulation of the lidar return can be carried out in a number of ways [33]. We have adopted the spectral-synthesis method, originally introduced by Zrnic [36] for radar. This method has been reliably used to simulate lidar return in literature (e.g., see [33]) and is computationally fast. Since a thorough performance analysis of the system, covering the non-ideal behavior of the components, is beyond the scope of the current paper, we have assumed ideal CDL behavior; the detectors have a resposivity of unity, the optical circulator does not exhibit any leakage or cross-talk, and the only noise source is the shot-noise of the photo detector which is assumed to be spectrally flat (white Gaussian noise).

Table 1: System simulation parameters

E_t [μJ]	110	PRR [kHz]	20
BW [MHz]	100	f_s [MHz]	100
pulse length [ns]	300	range gate [m]	90
integration time [s]	0.1, 0.05	N	512
D [cm]	10	C_n^2	10^{-14}

We have adopted (2.3) for the atmospheric simulation where the atmospheric transmission is affected by both aerosol and molecular backscatter. Since the Mie backscatter coefficient is unpredictable for different ranges and altitudes we have assumed a uniform scattering of identical particles in the air. The simulation has been performed for a lidar located at an altitude of 1 km from sea level with a horizontal beam (horizontal scan) measuring in one single direction. To estimate the contribution of Rayleigh backscatter to the optical transmission we have used the U.S Standard Atmospheric model. Fig. 6a shows the effective telescope area while Fig. 6b depicts the average Mie backscatter power for different ranges. For spectral processing we have adopted the Periodogram [37] associated with each range gate where zero-padding has been applied to smooth out the

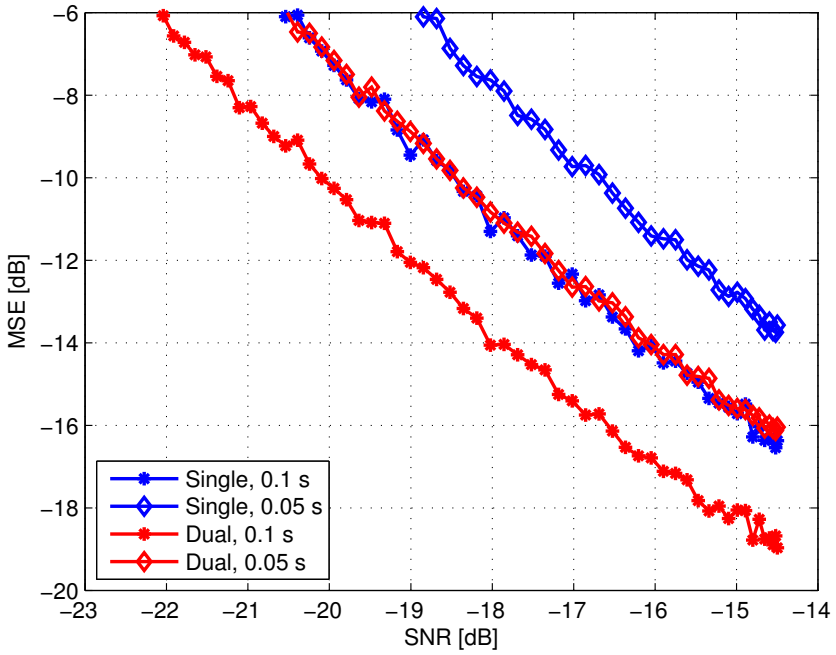

Figure 8: Mean square error (MSE) versus SNR. Single channel represents the MSE for one polarization state. Dual channel represents the MSE when the data from both polarization is utilized. The values are estimated for two different integration times, i.e., 0.1 and 0.05 s.

spectrum. Please note that zero-padding does not provide any extra information and has a curve fitting effect on the processed spectra. To estimate the mean Doppler shift, a maximum likelihood estimator (ML) was employed. The ML performance can reach the Cramer-Rao lower bound (CRLB) [38]; the CRLB is the lower achievable bound on the variance of any estimator. Furthermore, a relatively narrow-band Doppler spectrum [38], normalized variance of 0.02, was chosen for the simulations. A detailed list of simulation parameters is given in Table 1.

Fig. 7 shows the mean square error (MSE) associated with mode 2. The "Single" legend in the graph refers to the spectra acquired from only one channel, i.e., only one polarization state. The "Dual" refers to the scenario where the spectra from both channels (both polarization states) are averaged. Furthermore, the simulations have been carried out for two different integration times. It is evident from this figure that the effect of employing a dual polarization configuration where two EDFA's operate in concert (as described in Sec. 4) is an consistent improvement of 3-dB in MSE across different ranges. Please note that in this simulation we have ignored the range beyond which the MSE is above -6 dB; a mean speed estimation deviation of 0.5 m/s is equivalent to a -6 dB MSE. Another observation from Fig. 6 can be made. The MSE associated with the dual polarization configuration with an integration time of 0.05 s is consistent with the MSE for a single polarization mode with an integration time of 0.1 s. A factor of 2 reduction

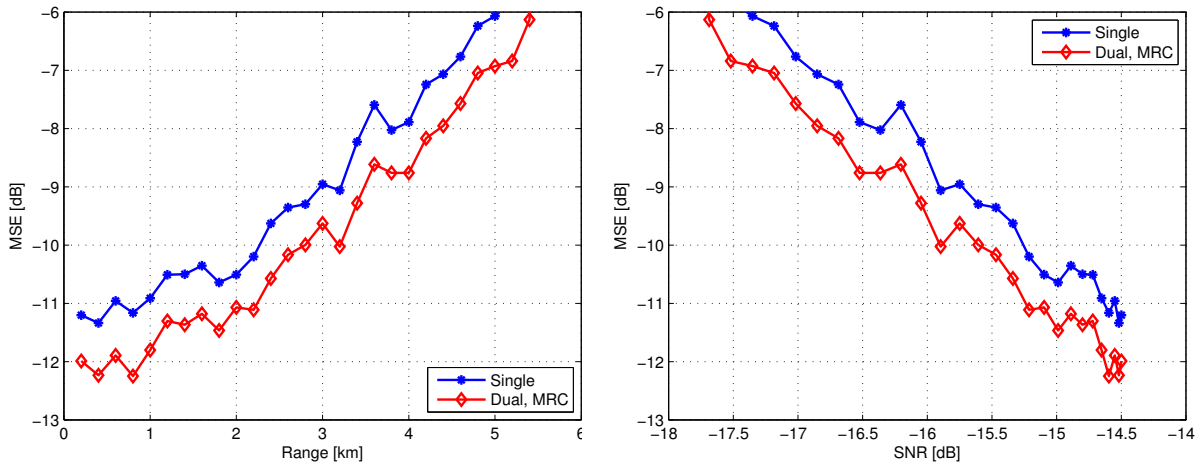

(a) MSE versus range

(b) MSE versus SNR

Figure 9: The MSE of the mean speed estimator associated with operation mode I. The simulations have been done following the relevant parameters given in table 1. A 0.05 s integration time and signal depolarization of 30% have been selected in this simulation.

in the integration time for the dual polarization mode is very attractive when operating the CDLs. We know from experience that one of the problems associated with a scanning CDL is the long time intervals associated with carrying out a full scan. By employing a dual polarization CDL the scanning time can be improved by a factor of 2 which is valuable in scanning CDLs. Please note that a range improvement of around 2.5 km is achieved by either by doubling the integration time or the transmitted optical power for the given simulation parameters. Fig. 8 shows the MSE versus SNR and is another way to illustrate the plots in Fig. 7.

To illustrate the performance of the system in mode I we have assumed a depolarization of 30%. As we have described in Sec. 4 the system operates with only one EDFA in this mode while detecting in co-pol and cross-pol components from the depolarized backscatter signal. The main benefit of this configuration is providing more information about the nature of the aerosol particles for each range gate. The added benefit is an improvement in the detected SNR which results in an improved estimated mean speed. Fig. 9a shows the MSE for the estimated mean speed calculated for a number of ranges. The simulation has been performed for an integration time of 0.05 s and a maximum MSE of -6 dB (0.5 m/s in standard deviation). As we can see from Fig. 9a an SNR improvement of 1 dB is observed when the cross-pol is combined with the co-pol signal using a MRC technique in the spectral domain.

6 Conclusions

All-fiber CDLs can benefit from the more mature and advanced optical communication technology. The adoption of relevant technologies in fiver-optic communications allows us to push the peformance of the all-fiber CDLs. In this paper, we showed that by employing

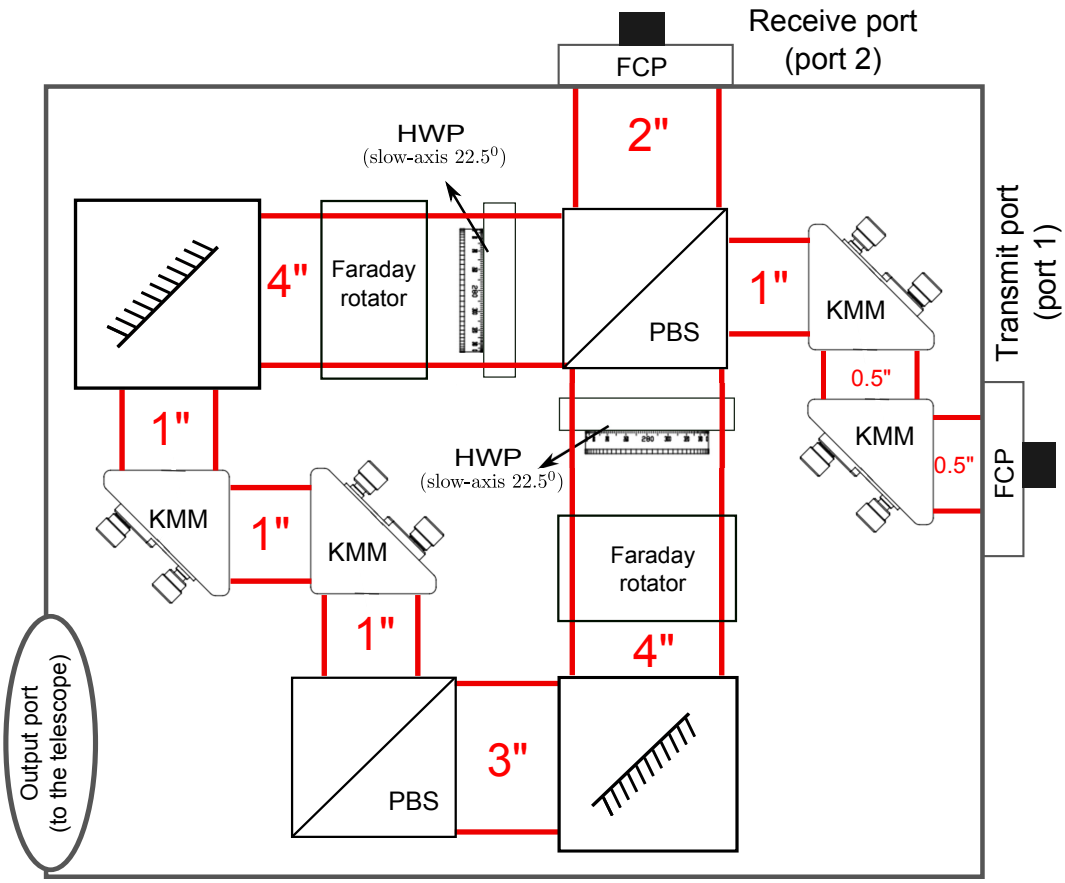

Figure 10: Polarization diversity circulator. The circulator is connected to the transmit and receiver fibers through the FCPs. The isolation between transmit and receive ports is provided through manipulation of light polarization through the PBS, HWP, and Faraday rotator. Two pairs of kinematic-mounted mirrors (KMM) provide enough degrees of freedom to align and overlap the transmit and receiver beams associated with the two polarization states.

an all-fiber polarization-diversity image-reject optical front-end not only faster and longer-range systems can be developed for the measurement of wind speed but also a simultaneous measurement of signal depolarization can be carried out. The depolarized signal can provide information about the nature of the aerosols for different ranges. Thanks to fiber-optic components, this system is compact, robust, and requires little maintenance when compared to its open-space optic counter parts. This system has the flexibility to be reconfigured on the fly to operate in two different modes. Due to its flexibility it can be adopted in any coherent detection system and its application is not limited to remote sensing of wind.

Appendix A Polarization-diversity optical circulator

The polarization-diversity optical circulator adopted in our system is based on the proposed architecture by Roth, et al. [39]. The employed optical circulator provides a large field of view and has a relatively high power handling (around 100 W/cm^2 for the system proposed in [39]). High power handling capability is crucial in pulsed lidar applications due to a high pulse peak power and energy. Fig. 10 shows the schematic for our adopted polarization diversity optical circulator; this circulator has been successfully built in the lab. Since, for the purposes of this paper, the non-ideal behavior of the components in the system is neglected, a detailed analysis of this circulator in terms of power handling, cross-talk, field of view, etc. is left out.

As seen in Fig. 10 this optical circulator can be viewed as a more complicated version of the single-polarization one shown in Fig. 2. One of the challenges in this sub-system is alignment of the two transmit and receive optical signals (a total of four signals) associated with the co-pol and cross-pol signals. As a result, three degrees of freedom for optical beam alignment in this system is required. We have adopted two pairs of mirrors in z-configurations, as shown in Fig. 10, providing tilt and beam displacement.

Acknowledgment

The authors would like to thank Alan Brewer at NOAA, Boulder for the valuable technical discussions as well as providing the lab environment for building and prototyping the polarization diversity optical circulator. Jakob Mann is grateful for a grant from the Ingeborg and Leo Dannin Foundation for Scientific Research, which was used to fund some of the lab equipment.

References

[1] E. O. Hulburt, "Observations of a searchlight beam to an altitude of 28 kilometers," *Appl. Opt.*, vol. 27, pp. 377–382, 1937.

[2] E. A. Johnson, R. C. Meyer, R. E. Hopkins, and W. H. Mock, "The measurement of light scattered by the upper atmosphere from a search-light beam," *Appl. Opt.*, vol. 29, pp. 512–517, 1939.

[3] X. Chu, W. Pan, G. C. Papen, C. S. Gardner, and J. A. Gelbwachs, "Fe Boltzmann temperature lidar: design, error analysis, and initial results at the North and South Poles," *Appl. Opt.*, vol. 41, pp. 4400–4410, 2002.

[4] X. Chu and G. Papen, "Resonance fluorescence lidar for measurements of the middle and upper atmosphere," *In Laser Remote Sensing*, T. Fujii and T. Fukuchi, eds. (CRC Press, 2005), pp. 179–432.

[5] Y. F. Arshinov, S. M. Bobrovnikov, V. E. Zuev, and V. M. Mitev, "Atmospheric temperature measurements using a pure rotational Raman lidar," *Appl. Opt.*, vol. 22, pp. 2984–2990, 1983.

[6] P. Piironen and E. W. Eloranta, "Demonstration of a high-spectral-resolution lidar based on an iodine absorption filter," *Appl. Opt.*, vol. 19, pp. 234–236, 1994.

[7] C. S. Gardner, "Sodium resonance fluorescence lidar applications in atmospheric science and astronomy," *Proc. IEEE*, vol. 77, pp. 408–418, 1989.

[8] R. T. Menzies and R. M. Hardesty, "Coherent Doppler Lidar for Measurements of Wind Fields," *Proc. IEEE*, vol. 77, pp. 449–462, 1989.

[9] R. M. Huffaker and R. M. Hardesty, "Remote sensing of atmospheric wind velocities using solid-state and CO2 coherent laser systems," *Proc. IEEE*, vol. 84, pp. 181–204, 1996.

[10] S. W. Henderson, C. P. Hale, J. R. Magee, M. J. Kavaya, and A. V. Huffaker, "Eye-safe coherent laser radar system at 2.1 μm using Tm,Ho:YAG lasers," *Appl. Opt.*, vol. 16, pp. 773–775, 1991.

[11] C. J. Karlsson, F. Olsson, D. Letalick, and M. Harris, "All-fiber multifunction continuous-wave coherent laser radar at 1.55 m for range, speed, vibration, and wind measurements," *Appl. Opt.*, vol. 39, pp. 3716–3726, 2000.

[12] G. N. Pearson, P. J. Roberts, J. R. Eacock, and M. Harris, "Analysis of the performance of a coherent pulsed fiber lidar for aerosol backscatter applications," *Appl. Opt.*, vol. **41**(30), pp. 6442–6450, 2002.

[13] S. M. Spuler, D. Richter, M. P. Spowart, and K. Rieken, "Optical fiber-based laser remote sensor for airborne measurement of wind velocity and turbulence," *Appl. Opt.*, vol. 50, pp. 842–851, 2011.

[14] WINDCUBE V2, a 200m vertical wind Doppler lidar. [Online]. Available: http://www.leosphere.com/products/vertical-profiling/windcube-v2. [Accessed Feb. 6, 2015].

[15] ZephIR 300 technical specifications. [Online]. Available: http://www.zephirlidar.com/resources/technical-specs. [Accessed Feb. 6, 2015].

[16] Halo Photonics pulsed Doppler LiDAR. [Online]. Available: http://halo-photonics.com. [Accessed Feb. 6, 2015].

[17] T. Mikkelsen, J. Mann, M. Courtney, and M. Sjöholm, "Lidar-based Research and Innovation at DTU Wind Energy–a Review," in *J. Phys.: Conf. Ser.*, vol. 524. IOP Publishing, 2014, p. 012007.

[18] C. F. Abari, A. T. Pedersen, and J. Mann, "An all-fiber image-reject homodyne coherent Doppler wind lidar," *Opt. Express*, vol. 22, pp. 25 880–25 894, 2014.

[19] C. F. Abari, A. T. Pedersen, E. Dellwik, and J. Mann, "Performance evaluation of an all-fiber image-reject homodyne coherent Doppler wind lidar," *Atmos. Meas. Tech. Discuss.*, vol. 8, pp. 3729–3752, 2015.

[20] COH28 dual-polarization 90^0 optical hybrid. [Online]. Available: http://kylia.com/?portfolio=90-hybrid-coh. [Accessed Feb. 6, 2015].

[21] C. M. Sonnenschein and F. A. Horrigan, "Signal-to-noise relationships for coaxial systems that heterodyne backscatter from the atmosphere," *Appl. Opt.*, vol. 10, pp. 1600–1604, 1971.

[22] T. Fujii and T. Fukuchi, *Laser Remote Sensing.* CRC Press, 486–488, 2005.

[23] S. F. Clifford and L. Lading, "Monostatic diffraction-limited lidars: the impact of optical refractive turbulence," *Appl. Opt.*, vol. 22, pp. 1696–1701, 1983.

[24] J. W. Goodman, "Some fundamental properties of speckle," *J. Opt. Soc. Am.*, vol. 66, pp. 1145–1150, 1976.

[25] D. L. Fried, "Optical heterodyne detection of an atmospherically distorted signal wave front," *Proc. IEEE*, vol. 55, pp. 57–67, 1967.

[26] R. G. Frehlich, "Effects of refractive turbulence on coherent laser radar," *Proc. IEEE*, vol. 32, pp. 2122–2139, 1993.

[27] I. Goldstein, P. A. Miles, and A. Chabot, "Heterodyne measurements of light propagation through atmospheric turbulence," *Proc. IEEE*, vol. 53, pp. 1172–1180, 1965.

[28] A. Belmonte and B. J. Rye, "Heterodyne lidar returns in the turbulent atmosphere: performance evaluation of simulated systems," *Appl. Opt.*, vol. 39, pp. 2401–2411, 2000.

[29] A. Dabas, P. H. Flamant, and P. Salamitou, "Characterization of pulsed coherent Doppler LIDAR with the speckle effect," *Appl. Opt.*, vol. 33, pp. 6524–6532, 1994.

[30] T. Matsumoto and K. Sato, "Polarization-independent optical circulator: an experiment," *Appl. Opt.*, vol. 19, pp. 108–112, 1980.

[31] M. Koga and T. Matsumoto, "High-isolation polarization-insensitive optical circulator for advanced optical communication systems," *J. Lightw. Technol.*, vol. 10, pp. 1210–1217, 1992.

[32] A. Belmonte, "Statistical model for fading return signals in coherent lidars," *Appl. Opt.*, vol. 49, pp. 6737–6748, 2010.

[33] B. Rye, "Spectral correlation of atmospheric lidar returns with range-dependent backscatter," *Appl. Opt.*, vol. 7, pp. 2199–2207, 1990.

[34] H. Cho, P. Yang, G. W. Kattawar, S. L. Nasiri, Y. HU, P. Minnis, C. Trepte, and D. Winker, "Depolarization ratio and attenuated backscatter for nine cloud types: analyses based on collocated CALIPSO lidar and MODIS measurements," *Opt. Express*, vol. 16, pp. 3931–3948, 2008.

[35] H. T. Hui, "The performance of the maximum ratio combining method in correlated Rician-fading channels for antenna-diversity signal combining," *IEEE Trans. Antennas Propag.*, vol. 53, pp. 958–964, 2005.

[36] D. S. Zrnic, "Simulation of Weatherlike Doppler Spectra and Signals," *J. Appl. Meteor.*, vol. 14, pp. 619–620, 1975.

[37] M. H. Hayes, *Statistical Digital Signal Processing and Modeling.* John Wiley & Sons, 391–424, 1996.

[38] B. J. Rye and R. M. Hardesty, "Discrete Spectral Peak Estimation in Incoherent Backscatter Heterodyne Lidar. I: Spectral Accumulation and the Cramer-Rao Lower Bound," *IEEE Trans. Geosci. Remote Sens.*, vol. 31, pp. 16–27, 1993.

[39] J. M. Roth, R. E. Bland, and S. I. Libby, "Large-aperture wide field of view optical circulators," *IEEE Photon. Technol. Lett.*, vol. 17, pp. 2128–2130, 2005.

A micropulse eye-safe all-fiber molecular backscatter coherent temperature lidar

Cyrus F. Abari, Xinzhao Chu, Jakob Mann, and Scott Spuler

Paper V

Based on: C. F. Abari, X. Chu, J. Mann, and S. Spuler, "A micropulse eye-safe all-fiber molecular backscatter coherent temperature lidar," in proc. of the 27th int. laser radar conf. (ILRC 2015), New York, USA, July 2015.

Abstract

In this paper, we have analyzed the performance of an all-fiber, micropulse, 1.5 μm coherent lidar for remote sensing of atmospheric temperature. The proposed system benefits from the recent advances in optics/electronics technology where a high resolution spectrum in the baseband can be acquired. Due to the presence of a structured spectra resulting from the spontaneous Rayleigh-Brillouine scattering, associated with the relevant operating regimes, an accurate estimation of the temperature can be carried out. One of the main advantages of this system is the removal of the contaminating Mie backscatter signal by electronic filters at the baseband (before signal conditioning and amplification). The paper presents the basic concepts as well as a Monte-Carlo system simulation as the proof of concept.

1 INTRODUCTION

Continuous high-resolution observation of atmospheric temperature profile in the troposphere is crucial for improved weather forecasting at the mesoscale [1]. In wind energy industry, where the latest turbines have reached heights beyond 200 m, remote sensing of temperature has become compelling. At these heights, wind shear, veer, and turbulence are highly sensitive to the stratification due to temperature [2]. Furthermore, profiling horizontal variations of temperature is important for the flow characterization on varying terrain.

Lidars can provide high spatial and temporal resolution monitoring of thermodynamic variables in the atmosphere. The majority of existing temperature measurement lidars benefit from the direct detection principle. In these systems sub-micron wavelengths are employed to take advantage of a stronger Rayleigh backscatter, where $\beta \propto \lambda^{-4}$ (β is the molecular backscatter cross-section and λ is the wavelength). There are a few disadvantages associated with such systems, e.g., they require high-power lasers which can be costly, bulky, and require high-maintenance. The transceivers in such systems can also be more costly and complicated to design and implement.

Coherent Doppler lidars (CDL), relying on Mie scattering, have been successfully used for remote sensing of wind [3–5]. Recent advances in fiber-optic technology and electronics have paved the way for a wide range of robust, compact, and cost-effective lasers and fiber-optic components. Successful realization of all-fiber CDLs operating at 1.5 μm wavelength has already been well established, e.g., see [4, 6]. Although the existing CDLs rely on Mie scattering to capture the wind-induced Doppler spectrum, modified systems should be capable of recording the thermally broadened (Doppler) spectrum from the molecular backscatter signal [7].

Historically, a few pitfalls have prevented the realization of a molecular coherent temperature lidar (CTL). The Rayleigh backscatter signal is weak and has a thermally broadened Doppler spectrum with a relatively wide bandwidth (BW), when compared to the narrowband Mie backscatter. The BW scales inversely with λ and is outside the detection BW of the available photodetector (PD) technology for sub-micron wavelengths. Only recently, PDs and fast analogue to digital converters (ADC) have become available with detection BWs that are comparable with the BW of the Rayleigh backscatter Doppler signal (for longer wavelengths in the infrared region such as 1.5 μm). Optical image-reject

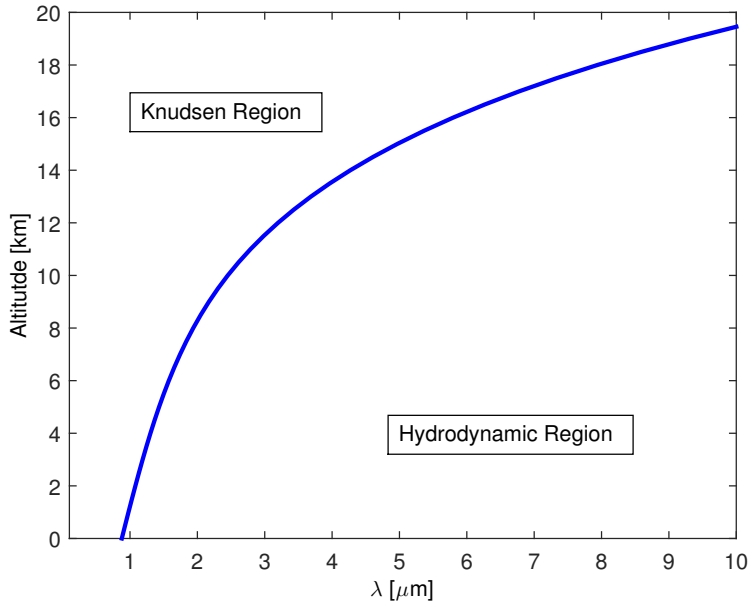

Figure 1: Transition from the Kundsen to hydrodynamic region [7]. The region below the curve represents the area where the wavelength is longer than the mean free-path in the atmosphere, hence, SRB backscattering.

down-conversion of Doppler signals to baseband, essential for resolving positive and negative frequency shifts, has not been practically demonstrated, viz., not until recently [8]. This is an essential part of the proposed CTL to circumvent the restrictions imposed by the available BW of ADCs and PDs. The alternative, and conventionally employed, down-conversion to intermediate frequency (IF) band, places unrealistic requirements on the BW of the PDs and ADCs. A successful prototyping of an all-fiber image-reject homodyne receiver demonstrated by Abari et al. [8] facilitates the realization of a molecular backscatter CTL as suggested in this paper.

2 Spontaneous Rayleigh-Brillouin (SRB) backscattering and system description

A theoretical feasibility study of a molecular backscatter CTL was carried out by Rye [7] for a few wavelengths (i.e., 350, 2100, and 10600 nm). The results indicate that the longer wavelengths, in the infrared (IR) spectrum, may operate in the hydrodynamic region, where λ is larger than the mean free path in the air [7, 9]. In this region the return signal is not purely Rayleigh; the return spectra has contributions from the Rayleigh and spontaneous Brillouin backscatter signal, known as spontaneous Rayleigh-Brillouin (SRB), resulting in a triplet of peaks in the spectra. Fig. 1 shows the transition from the Kundsen (where the backscatter signal is largely dominated by the Rayeligh backscatter) to hydrodynamic region for different wavelengths and altitudes. As a result, due to the

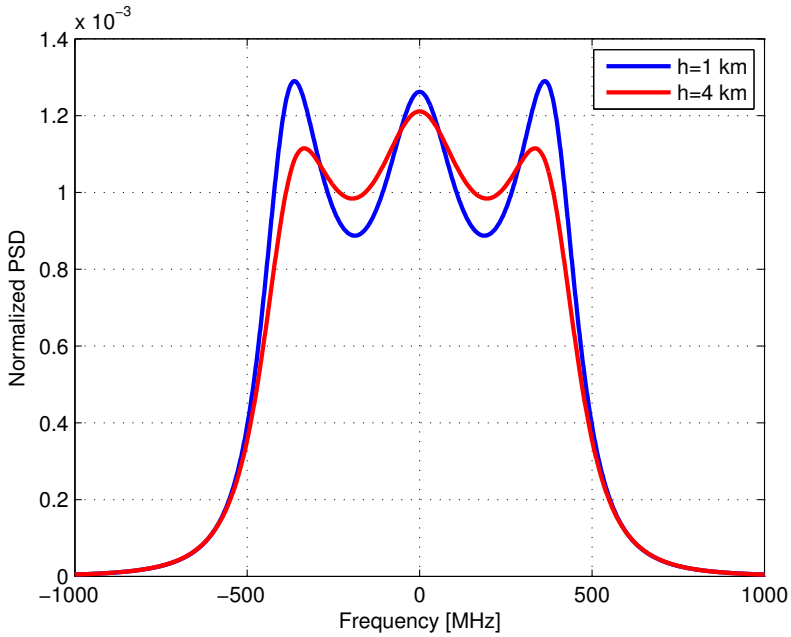

Figure 2: SRB spectrum for $\lambda = 1560$ nm at two different altitudes in reference to sea level. The data is taken from the U.S. Standard Atmosphere Model.

presence of a structured SRB backscatter Doppler spectrum in the hydrodynamic region [10] as well as the inherent CTL detection sensitivity, accurate estimation of temperature from a weak molecular backscatter is possible; the presence of narrowband Brillouin peaks provide a reliable measure of the atmospheric temperature [7]. As we will see in Sec. 3, we have resorted to a least squares (LS) curve fitting between the estimated and expected spectra to estimate the temperature. The added benefit of LS curve fitting is the potential for extracting other parameters (e.g., atmospheric pressure) from the estimated spectra [7].

Following Tenti's S6 theory [9], the spectra associated with the SRB backscatter for $\lambda = 1560$ nm (at two different heights in reference to sea level) has been calculated and shown in Fig. 2. As the atmospheric pressure decreases (i.e., the altitude increases) the contribution from the Brillouin effect is reduced (as the mean free-path between the molecules becomes comparable with the laser wavelength) and the Rayleigh backscatter becomes more dominant. This is why the Brillouin peaks associated with the estimated spectra at an altitude of $h = 4$ km shown in Fig 2 are less pronounced when compared to the spectra estimated at $h = 1$ km.

In light of Rye's [7] results, we have shown that it is possible to use a micropulse 1.5μm CTL to carry out an accurate remote sensing of temperature in the lower atmosphere. Although the micropulse system cannot rival the solid-state or gas-based IR laser, in terms of the maximum available pulse energy, it provides comparable average output powers. In other words, the integration time is competitive with the high power IR systems analyzed in [7]. High-quality all-fiber 1.5 μm pulsed erbium doped fiber amplifiers (EDFA) with a PRR of 10-20 kHz and pulse energy of 110-220 μJ (average optical power of 2.2 W) are available as off-the-shelf components [11] and have been successfully integrated in com-

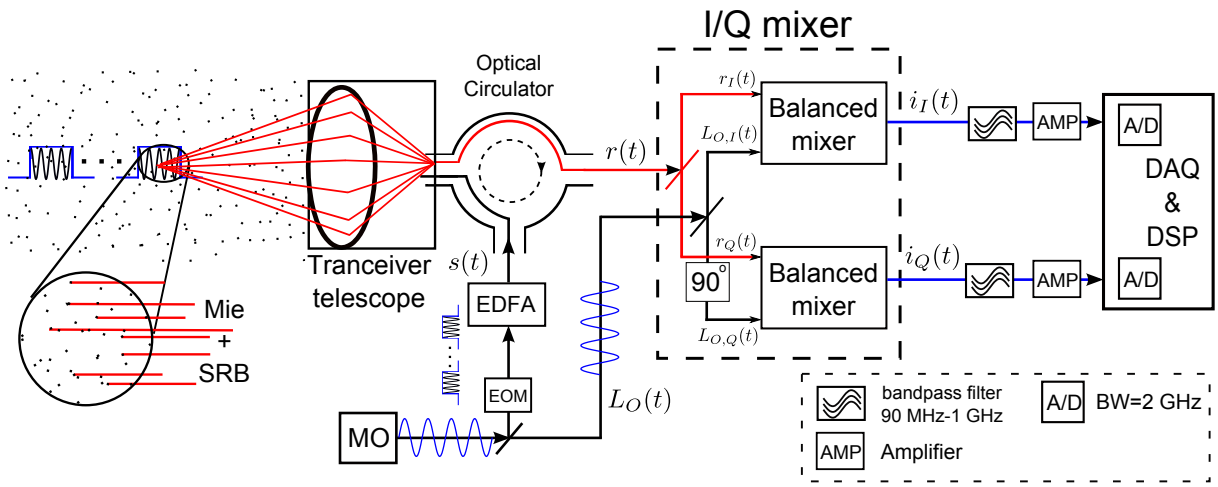

Figure 3: An all-fiber pulsed image-reject homodybe CTL. The master oscillator (MO) provides a highly stable and narrow linewidth laser which is split into (by a beam splitter) a local oscillator (LO) and input signal to the electro-optic modulator (EOM). The EOM can be programmed to generate the desired pulse train which is amplified by the EDFA. The optical circulator isolates the transmit and receive signals. The in-phase/quadrature-phase (I/Q) mixer translates the spectral information into baseband for further processing. For a detailed analysis of the image-reject receiver please refer to Abari, et al. [8]. The bandpass filters, designed for a maximum expected mean wind speed, filter out the Mie signal.

mercially available all-fiber wind CDLs [6]. More powerful multi-stage EDFAs, benefiting from large core optical fibers, can be developed and integrated into the micropulse system to improve the range and required integration time.

Fig. 3 shows the schematic of the proposed all-fiber CTL. This system benefits from an all-fiber image-reject homodyne receiver [8] which allows the translation of the frequency-shifted signals into the baseband. Due to a relatively narrow BW associated with the 1560 nm molecular backscatter signal, a PD with a BW of 1 GHz and two ADCs with a sampling rate of 2 GHz provide the opportunity to resolve the spectral components, which upon further processing and digital signal processing allow the estimation of the relevant parameters such as temperature. A common problem associated with the detection and characterization of the molecular backscatter signal in the lower atmosphere is a strong contamination resulting from the Mie backscattering which dominates the return signal. In direct detection techniques, such as high spectral resolution lidars (HSRL), optical filters, only available for a limited number of wavelengths, are employed to filter out the Mie component from the return signal. In the proposed system, we suggest the removal of the Mie backscatter directly at the output of the PD. If the dominant Mie component is not removed immediately before amplification and conditioning of the detected signal, it will either saturate or occupy the dynamic range of the following stages, i.e., the electronic components adopted for signal amplification, conditioning, and sampling. One of the main merits of this system is to remove the Mie component through reliable, cost-effective, and accurate electronic filters. In this system the electronic filter BW can be designed for the expected maximum mean wind speed. Moreover, due to the nature of coherent detection,

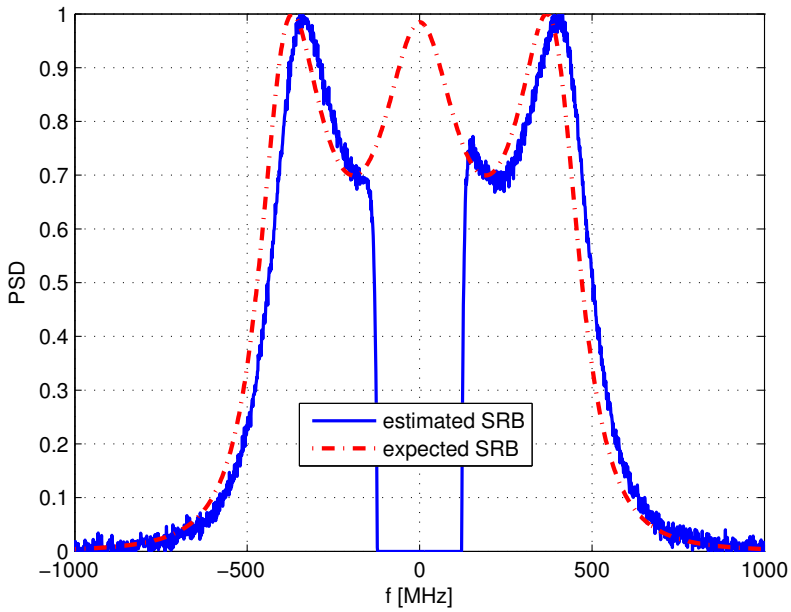

Figure 4: The simulated return spectrum (target range of 1 km, please see Table 1). The observed mean frequency shift in the blue curve is due to a presumed mean wind speed of 25 ms^{-1}.

background light removal, necessary in direct detection systems, is not required in the proposed system.

3 Simulation Results

The performance of the system suggested in this paper is evaluated through modeling and Monte-Carlo simulations performed in Matlab. In our simulation the combined effects of Mie and molecular backscattering are taken into account. Since the aerosol type and density in the atmosphere is hard to predict and model, we have assumed a moderate loading of aerosols [12] with uniform scattering throughout the measurement range. The Rayleigh backscatter parameters have been adopted from the U.S. Standard Atmospheric Model. Furthermore, the Monte-Carlo simulations have been done for a CTL located 1 km above the sea level performing a horizontal scan. The simulation parameters are listed in Table 1. Please note that β_{Mie} and D represent Mie backscattering coefficient and the telescope diameter, respectively.

For the estimation of the temperature we have resorted to an LS estimator in this paper. The estimator employs a LS fitting of the acquired spectra; an iterative procedure where the SRB curve resulting in the LS error between the acquired spectra and the curve is selected as the best estimate. For the performance characterization of our system, we have adopted the mean square error (MSE) of the temperature estimator for different ranges; the MSE can be viewed as the variance of the estimator. Fig. 5 shows the MSE

Table 1: Simulation parameters

E_t [μJ]	220	PRR [kHz]	10
PD BW [GHz]	1	f_s [GHz]	2
pulse length [ns]	400	resolution [m]	95
integration time [s]	60	N [FFT points]	1024
D [cm]	20	β_{Mie}	1.83×10^{-7}

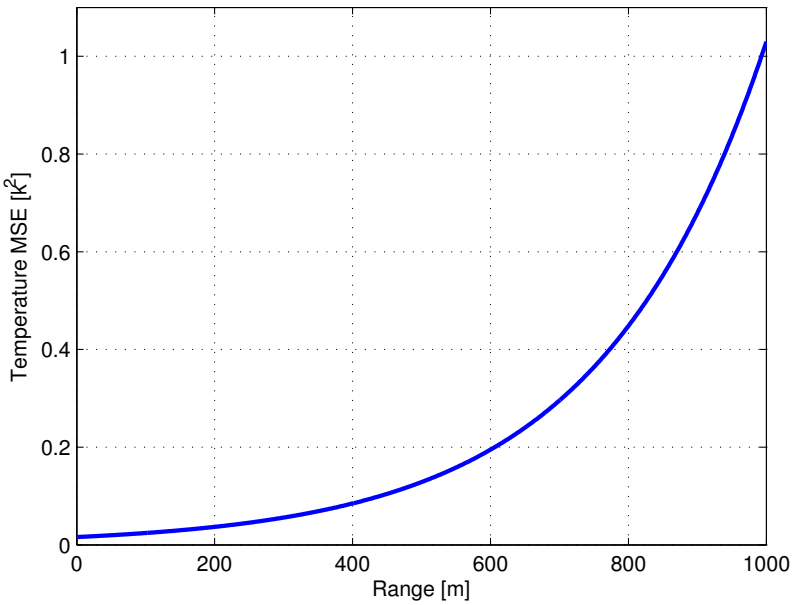

Figure 5: MSE (variance) of the temperature estimator (for a temporal resolution of 60 s) versus target range.

of the temperature estimator adopted in this paper for different ranges. As we can see the estimator provides an estimate of the temperature with a variance better than 1 K for a measurement range of up to 1 km. It can be shown that the measurement range can be improved by increasing the pulse energy or integration time. Due to the availability of high speed computers and digital signal processors, more advanced signal processing can be adopted to improved the temperature estimation accuracy which can result in a longer measurement range for a given system configuration and atmospheric condition.

4 CONCLUSIONS

In this paper, we have shown that in light of recent advances in fiber-optic and electronic technology it is feasible to build a compact and robust coherent lidar for remote sensing of atmospheric temperature. Compared to other lidars, the proposed system should be low-cost, low-maintenance, and can be deployed as an eye-safe system (in the same fashion 1.5μm wind Doppler lidars with similar optical output powers operate, e.g., a scanning

CTL). Due to it's form factor the system can be deployed as ground-base or airborne. Furthermore, the system has the potential to provide simultaneous measurements of wind and pressure (besides temperature); this will be investigated in our future work. We have adopted only one simple estimator, i.e., LS, to demonstrate the feasibility of the proposed CTL. However, we believe there is room for improved estimation algorithms where the Cramer-Rao lower bound (CRLB), computationally calculated in [7], can be achieved.

References

[1] Committee on Developing Mesoscale Meteorological Observational Capabilities to Meet Multiple Needs, National Research Council, *Observing Weather and Climate from the Ground Up: A Nationwide Network of Networks.* Washington, D.C.: The National Academies Press, 2009.

[2] A. Sathe, J. Mann, T. Barlas, W. Bierbooms, and G. van Bussel, "Influence of atmospheric stability on wind turbine loads," *Wind Energy*, vol. 16, no. 7, pp. 1013–1032, 2013.

[3] F. Hall, R. Huffaker, R. Hardesty, M. Jackson, T. Lawrence, M. Post, R. Richter, and B. Weber, "Wind measurement accuracy of the NOAA pulsed infrared Doppler lidar," *Appl. Opt.*, vol. 23, no. 15, pp. 2503–2506, 1984.

[4] S. M. Spuler, D. Richter, M. P. Spowart, and K. Rieken, "Optical fiber-based laser remote sensor for airborne measurement of wind velocity and turbulence," *Appl. Opt.*, vol. 50, pp. 842–851, 2011.

[5] R. M. Huffaker and R. M. Hardesty, "Remote sensing of atmospheric wind velocities using solid-state and CO_2 coherent laser systems," *Proc. IEEE*, vol. 84, pp. 181–204, 1996.

[6] WINDCUBE V2, a 200m vertical wind Doppler lidar. [Online]. Available: http://www.leosphere.com/products/vertical-profiling/windcube-v2. [Accessed Feb. 6, 2015].

[7] B. J. Rye, "Molecular backscatter heterodyne lidar: a computational evaluation," *Appl. Opt.*, vol. 37, no. 27, pp. 6321–6328, 1998.

[8] C. F. Abari, A. T. Pedersen, and J. Mann, "An all-fiber image-reject homodyne coherent Doppler wind lidar," *Opt. Express*, vol. 22, pp. 25 880–25 894, 2014.

[9] C. D. Boley, R. C. Desai, and G. Tenti, "Kinetic models and Brillouin scattering in a Molecular Gas," *Canadian Journal of Physics*, vol. 50, no. 18, pp. 2158–2173, 1972.

[10] Z. Gu, B. Witschas, W. van de Water, and W. Ubachs, "Rayleigh–Brillouin scattering profiles of air at different temperatures and pressures," *Appl. Opt.*, vol. 52, no. 19, pp. 4640–4651, 2013.

[11] 1.5 μm LONG PULSE FIBER AMPLIFIER, (Keopsys, 2015). [Online]. Available: http://www.keopsys.com.[Accessed Feb. 6, 2015].

[12] V. Srivastava, J. Rothermel, A. D. Clarke, J. D. Spinhirne, R. T. Menzies, D. R. Cutten, M. A. Jarzembski, D. A. Bowdle, and E. W. McCaul, "Wavelength dependence of backscatter by use of aerosol microphysics and lidar data sets: application to 2.1-μm wavelength for space-based and airborne lidars," *Appl. Opt.*, vol. 40, pp. 4759–4769, 2001.